THESIS FOR THE DEGREE OF DOCTOR OF PHILOSOPHY

The Hydrodynamics of Waterjet/Hull Interaction

ARASH ESLAMDOOST

Department of Shipping and Marine Technology
CHALMERS UNIVERSITY OF TECHNOLOGY
Gothenburg, Sweden
2014

The Hydrodynamics of Waterjet/Hull Interaction

ISBN: 978-91-7597-133-9

Doctoral Thesis at Chalmers University of Technology
Report No: 3814
ISSN 0346-718X.

Division of Marine Technology
Department of Shipping and Marine Technology
Chalmers University of Technology
SE-412 96 Gothenburg
Sweden
Telephone + 46 (0)31-772 1000

Printed by Chalmers Reproservice
Gothenburg, Sweden 2014

The Hydrodynamics of Waterjet/Hull Interaction

Arash Eslamdoost
Division of Marine Technology
Department of Shipping and Marine Technology
Chalmers University of Technology

Abstract

The objective of the present investigation is to explore the physics behind the waterjet/hull interaction, and in particular the negative thrust deduction often reported in the semi-planing speed range. Another objective is to propose a validated numerical technique for computing the hydrodynamics of waterjet-driven hulls.

The parameters that play a role in the waterjet/hull interaction are split into global effects (i.e. sinkage and trim variations) and local effects (other effects caused by the intake suction) and each are addressed individually in this thesis. Investigation of these parameters is carried out in two different ways. First, assuming the flow to be potential flow, an algorithm is developed for modelling the water/hull interaction. Then, in the second part of the thesis, a technique employing a Reynolds-Averaged Navier-Stokes (RANS) solver is employed for modelling the flow and understanding the interaction effects.

The algorithm used in the first part is called the Pressure Jump Method in this thesis. This method is based on the equilibrium condition that the resistance forces are balanced by the thrust force created by the head increase through the waterjet pump. The Pressure Jump Method is coupled with a potential flow solver capable of non-linear free-surface modelling. Validation and verification of the method are accomplished by comparing the computational results with experimental data available from a test case. The resistance increment of the hull is also estimated using the Pressure Jump Method and the dominant parameters, which contribute to the thrust deduction, are determined. General sinkage and trim changes between the bare hull and the self-propelled hull are also estimated by approximating the waterjet-propelled hull as a flat plate with a rectangular hole representing the intake opening.

In the second part of the thesis, a technique using a RANS solver with a Volume of Fluid (VOF) free-surface representation combined with a body force representation of the pump is developed and validated against measurements. Using the results of this technique, the thrust deduction fraction is studied in detail from very low to high speeds. It is revealed that, in the lower speed range, the transom clearance plays an important role in the behaviour of the thrust deduction fraction. Therefore, the transom clearance phenomenon is studied in detail. The reasons for the waterjet-driven hull resistance increment are identified through studying the hydrostatic and the hydrodynamic pressure resistance as well as the frictional resistance variations over the entire speed range. The difference between the net thrust and the gross thrust of the waterjet system, which has been a controversial issue, is also studied in this thesis and it is seen that this difference may well be the reason for the negative thrust deduction. Other issues investigated in the thesis are the shape of the capture area and the streamtube within which all water going into the intake is contained, the importance of the velocity profile at the intake and exit, the pressure distribution at the exit and the diameter and position of the vena-contracta.

Keywords: waterjet propulsion, waterjet/hull interaction, net thrust, gross thrust, thrust deduction, sinkage, trim angle, potential flow, non-linear free-surface, RANS, VOF, intake drag, exit drag, capture area, vena-contracta, streamtube, transom clearance

Preface

This thesis presents a project carried out at the Hydrodynamics Research Group of the Department of Shipping and Marine Technology, Chalmers University of Technology during 2009 to 2014. It is in the framework of the PhD project “The Hydrodynamics of Waterjet/Hull Interaction,” supported by Rolls-Royce Marine through the University Technology Centre in Computational Hydrodynamics hosted by the Department of Shipping and Marine Technology at Chalmers.

Acknowledgements

First and foremost I would like to express my gratitude to my supervisors Professor Lars Larsson, for all the valuable discussions, enthusiasm and willingness to help and Professor Rickard Bensow for his support and guidance. I would not have been able to do this work without the help of my supervisors.

Many thanks go to Marko Hyensjö, Reima Aartojärvi, Johan Lundberg, Göran Grunditz and Urban Svennberg of Rolls-Royce AB, for sharing their experiences and encouraging me throughout the project. I would like to acknowledge the important contributions by Matz Brown and his colleagues Hans Liljenberg and Da-Qing Li in connection with the waterjet tests at SSPA. The results of these measurements paved the way to understand many aspects of the waterjet/hull interaction. Further, I would like to extend my appreciation to Professor Tom van Terwisga for his comprehensive doctoral thesis, which in fact is the basis of the current thesis, as well as for leading my licentiate thesis seminar and making it an inspiring event. I am also grateful to John G. Hoyt III for providing me with the test data from the ITTC Specialist Committee on Validation of Waterjet Test Procedures as well as his fruitful hints and comments. Special thanks also to the colleagues and staff at the Department of Shipping and Marine technology for providing a pleasant working environment.

Rolls-Royce Marine is acknowledged for funding the project through the Rolls-Royce University Technology Centre at Chalmers. The Chalmers Centre for Computational Science and Engineering (C^3SE) is also acknowledged for providing computational resources throughout the project.

I truly appreciate my friends, who with their kindness have made my life sweeter and more charming. Finally, I would like to express my warmest and deepest gratitude to my family and thank them for all their sincere support and encouragement.

Gothenburg, December 2014
Arash Eslamdoost

TABLE OF CONTENTS

1 Introduction

Waterjet propulsion may be considered as one of the common contemporary propulsion systems. This propulsion method is not as popular as conventional propellers but is competitive to them in certain operating conditions. The tendency to use waterjet propulsion is increasing thanks to the enhanced efficiency of these systems. In order to investigate the reasons behind this increased interest in applying waterjet propulsion, we need to know the specific characteristics of the propulsion method and its advantages and disadvantages under various operating conditions. In this chapter, a brief review of the history of waterjet propulsion developments is presented and then the components of current waterjet units and their features are introduced. The historical steps mentioned in this chapter are not covering the entire known progress in the history of waterjet propulsion but only some selected pieces to show the pace of the development.

1.1 History of Waterjet Propulsion Development

The very first idea of a mechanised marine propulsion system was introduced in England ’s patent no. 5 by David Rumsey (1631). The first sign of employing steam power for industrial purposes emerges through this patent and Ramsey specifically mentions that steam power might be used "*to make boates, shippes and barges to goe against the wind and tyde*"(Raithby 1829).

In ancient times, an Archimedean screw (Figure 1.1) was being used to irrigate and pump out flooded ships. The concept used in this screw to pump water was more or less similar to the sketch drawn by Leonardo da Vinci showing a rotating spiral for raising water and the rotor of his famous helicopter (Figure 1.2). Adopting the Archimedian screw as a ship propeller, Toogood and Hays (1661) introduced an initial waterjet propulsion concept, which is registered as patent no. 132 in England with the following description:

“*A newe inventc̃on of forceing water by bellowes, not done with wind, alsoe the draweing it vpp with leatheme baggs linked togeather in manner of bucketts where the bellowes cannot be placed which may be for the publique benefitt of shipping, drayning of mines, bringing*

water to houses, emptying of rivers or ponds, drayneing & watering of grounds, or any way of pumping water, together with a particular way of forceing water through the bottome or sides of shipps belowe the surface or toppe of the water which may be of singular vse and ease in navigac͡on, & was never before publiquely done or vsed within any of our kingdomes, Dominions, or Territories"(Bennet 1858).

Years later, in 1730, Dr. John Allen, MD, introduced a different concept of waterjet propulsion, which generated steam aboard a vessel and discharged the steam jet through the stern into the water forcing the craft along (Roy 1994).

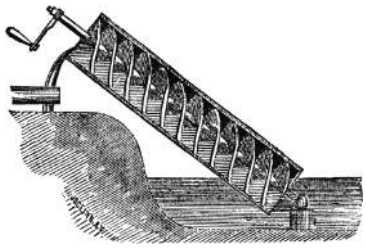

Figure 1.1. Archemidian screw

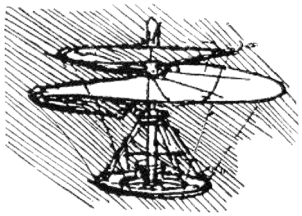

Figure 1.2. Helicopter drawing by Leonardo da Vinci

James Thomas Flexner (1944) discusses the history of the steamboats, developers and patents in this area. He mentions that in 1753, Benjamin Franklin (1706-1790) was inspired by the Frenchman Daniel Bernoulli (1700-1782) to develop waterjet propulsion systems. Flexner says Bernoulli believed that "*if a stream of water was driven out of the stern of a boat below the water line, its reaction on the body of water in which the boat floated would drive the vessel forward. Bernoulli's experiment had merely involved an L-shaped pipe stretching to the rear into which water could be poured; Franklin added a pump that drew water in at the bow and drove it out at the stern. 'A fire engine might in some case be applied to this operation with advantage' he concluded*".

In the mid-1780's and early 1790's, James Rumsey and John Fitch each separately developed waterjet propulsion systems. Rumsey developed a tube boiler and utilized it in his waterjet system, which consisted of a cylinder of steam on top and a pump cylinder, both sharing a single piston rod. Water was sucked through some valves placed in the keel and rushed out of the stern. Rumsey's waterjet system propelled the boat with the speed of two miles per hour, about 1.73 knots. In 1790, Fitch applied the same concept as introduced by Allen sixty years earlier, forcing a column of air through trunks filled with water out of the stern while the bow valves were closed (Roy 1994). Figure 1.3 illustrates a sketch of Fitch's design (Schult 1974).

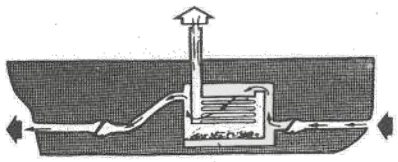

Figure 1.3. Sketch (by Schult) of Fitch's 1790 Waterjet Patent (Schult 1974)

After some trials with different concepts of waterjet systems, engineers noticed that “certain characteristics of early waterjet proposals, such as the friction of the water in the long pipes with the relatively inefficient combination of a positive displacement pump, coupled with a reciprocating steam engine, would not be able to match the efficiency of paddle wheels or screw propellers” (Roy 1994). The problems mentioned were solved to some extent by the invention of hydraulic pumps. Roy (1994), discusses the history of developing and utilizing hydraulic pumps. A rather developed design of waterjet systems including an hydraulic pump based on Barnaby’s suggestion is depicted in Figure 1.4. Barnaby suggested to “reduce the efficiency losses by obviating the need to raise or turn the ducts of water and by aligning the axis of the centrifugal pump horizontally instead of vertically”; he also mentioned that “if the pump could be put outside the boat, there would be no problem with getting water into the boat and up to the pump, and, little or no water would be carried” (Roy 1994).

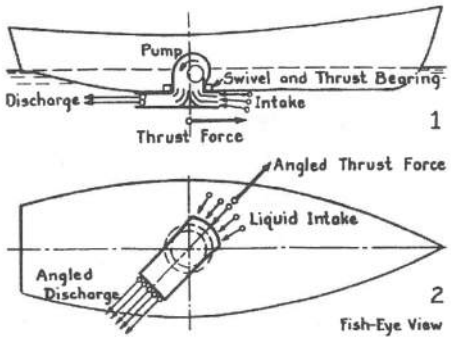

Figure 1.4 “Hydraulic-Jet” propulsion based on Barnaby’s idea in 1884 (Saunders 1957)

Roy (1994), indicates the Energy Burst Systems as the next important step towards modern waterjet systems. He believes that although Fitch’s patent of 1790 was a waterjet system, it may be described as an intermittent energy burst waterjet propulsor. Another example of the early designs of energy burst systems is known as the McHugh (1916) pulsejet (Roy 1994). Although this pulsejet system was unsuccessful in full scale design but extremely effective in model scale and countless numbers were sold as toys from the 1920s and onwards (Roy 1994). Figure 1.5 shows a schematic presentation of a similar pulsejet system. There exists an engine consisting of a boiler connected to one or two tubes. By heating up the boiler, the steam inside expands and pushes the water column inside the tubes backwards, resulting in a thrust force. Next, due to the condensation of the steam bubble and lower pressure inside the boiler, water is sucked back into the tubes. This procedure continues repeatedly and causes a cyclical thrust force.

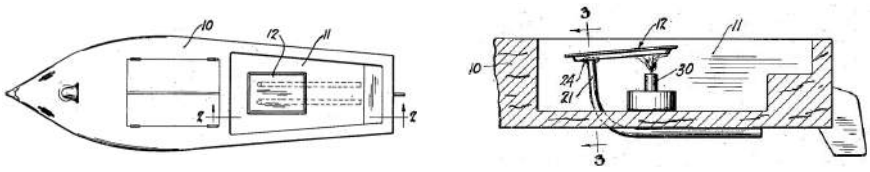

Figure 1.5 Diaphragm type of pulsejet engine (Jones, Jr. , Paul, Harman 1935). The left figure shows the general arrangement of the system and the right figure depicts the side view of midsection of the pulsejet engine of diaphragm type. No. 12 and 30 show the boiler and heater respectively. Connected tubes are marked by no. 21.

Another example of more sophisticated energy burst waterjet systems is shown in Figure 1.6. In this design, “the ingenious power head utilized a reed valve at the air inlet to control the energy burst in the combustion gas exited through a novel ring-shaped device which acted as both a rudimentary pressure valve and a discharge nozzle” (Roy 1994).

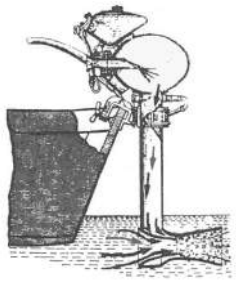

Figure 1.6 Sketch by Schult of H. J. MacCollum’s (1946) Pulse Jet Outboard (Schult 1974)

In 1950, Kenneth produced a small jet outboard with an horizontal impeller. In the same year, William Hamilton developed the very first high-speed jet propulsion system, which in general showed similarities with modern designs employed nowadays. After this time, some upgrades have been made on waterjet designs to increase the efficiency of these propulsion systems, which in some cases resulted in outstanding outcomes. An example of such an outcome is the 68 *m* Destriero which, propelled by three KaMeWa units (Roy 1994), scored an Atlantic record at almost 53 knots. The history reviewed in this section only represented some selected designs and developments achieved in the history of waterjet propulsion systems. Some additional historical events related to marine waterjet development are provided in Appendix A. More detailed information may be found in (Allison et al. 2001) and (Roy 1994).

1.2 Connection to other Turbomachines

The principle behind all types of conventional turbomachins is quite similar. These systems are either used to absorb energy from a fluid stream and deliver mechanical power through a shaft (e.g. windmills, water turbines) or employ the delivered power through a shaft to create a stream of higher energy levels (e.g. pumps, fans, axial compressors). Figure 1.7 shows the connection between different types of turbomachins in the form of a box model (Bulten 2006). The characteristic properties of each face of the box model are mentioned in Table 1.1. By reviewing the development history of the thrusters, it is observed that when there is need for higher velocities, thrusters move from external flow to internal flow thrusters inside a special casing; this is similar to the development of aeronautical thrusters which started with propellers and were later upgraded to jet engines. A same trend is observed in marine thrusters, which were started with paddles and propellers and were then improved to become ducted propellers and waterjet propulsion systems.

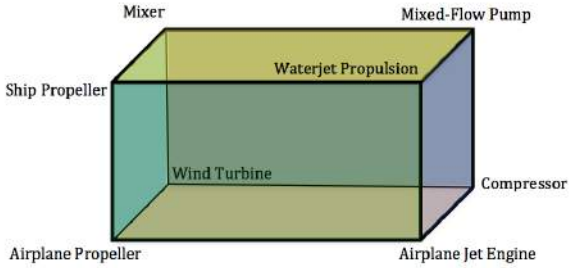

Figure 1.7 Relation between the waterjet propulsion systems and the other types of turbomachinery (Bulten 2006).

Table 1.1 Characteristics of the turbomachins on each face of the box model introduced in Figure 1.7

Front Face	Designed to produce thrust
Back Face	Any thrust production is an undesirable effect
Top Face	Operate in water; Cavitation might be important
Bottom Face	Operate in air; Compressibility might be important
Left Face	External flow machines; Thrust transmision only through shaft only
Right Face	Internal flow machines; Thrust transmision through both shaft and casing

1.2.1 Comparison with Marine Propellers

Perusing the history of marine propulsors, there has been a tendency to employ marine screw propellers rather than waterjet systems, the reason is that the design and production procedure of propellers were easier. But the introduction of more efficient pumps utilizable in waterjet systems in recent decades has changed the strong tendency of using screw propellers. Nowadays, there are specific characteristics of waterjet propulsion systems that make them a better choice in comparison with conventional marine propellers, including higher achievable velocity, better manoeuvrability (e.g. zero speed docking, sideways movement with multiple jet installation and the possibility to stop quickly) and lower noise levels.

Due to the fact that there are no appendages, such as struts, rudders etc., the shallow draft of the system makes it possible to run the craft in shallow waters. However, by operating in this condition, mud and other debris might be sucked into the system and cause damage to the pump system. At high speeds, the appendage drag can achieve 20% of the bare hull drag (van Terwisga 1996). There is indeed no such drag component for waterjets.

The extent of cavitation is rather different for propellers and waterjet systems. Due to increased pressure inside the waterjet system, cavitation occurs at higher velocities. Therefore, when conventional transcavitating and supercavitating propeller performance fall off, waterjets are better choices; surface piercing propellers and waterjet systems are more or less competitive. According to the heavier weight of waterjet units compared to conventional propellers, these systems become more efficient on larger crafts such as wave-piercing ferries (Carlton 2007).

Combining waterjets and propellers in the form of hybrid propulsion is also a possible option. In this case smaller propellers with lower noise and vibration levels are used for normal cruising, while a central waterjet system would be employed to boost the system to achieve higher speeds.

1.3 Common Waterjet Systems

Generally, four different basic types of waterjet propulsion systems exist (Figure 1.8). The major difference between these designs is the ducting channel geometry and the pump installation in these systems. The most conventional intake is a flush type intake in which the duct opening is almost parallel to the intake flow. For ram type intakes, the intake opening is normal to the intake flow.

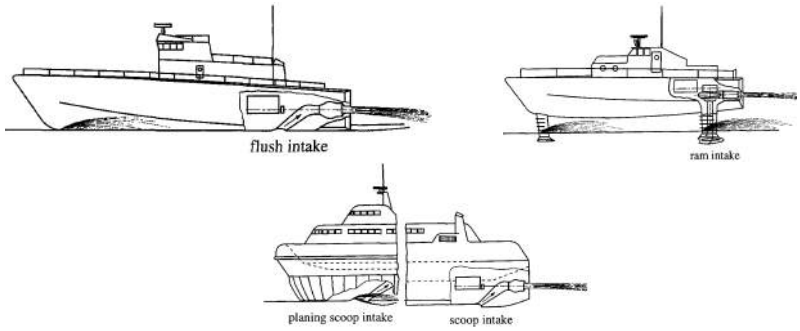

Figure 1.8 Basic intake concepts (Kruppa, C., Brandt, H., Östergaard 1968)

Figure 1.9 depicts the main components of flush intake waterjet system, which includes an inlet duct, pump, nozzle and steering unit. Water is sucked into the intake opening and guided through the ducting channel into the pump. As shown in Figure 1.10, pumps are categorized into axial, mixed and centrifugal flow pumps based on the angle of inflow and outflow. Axial and mixed flow pumps are the major types being used in the design of waterjet propulsion systems. Generally, mixed flow pumps are wider compared to axial flow pumps; this should be taken into consideration during the design process, especially when multiple waterjet units are supposed to propel a vessel.

Passing through impeller and stator, the flow approaches the nozzle. The duty of a nozzle is to increase the momentum flux by ejecting the flow, which is accomplished by the contraction of the nozzle. “Nozzle is usually shaped such as to have the vena-contracta of the discharged jet coinciding with the nozzle exit” (van Terwisga 1996). The vena-contracta of a jet is the section of the jet in which the average static pressure is identical to the ambient pressure in that section. Depending on the nozzle design, vena-contracta may occur at the nozzle discharge section or further downstream. Additional discussions about the position of vena-contracta take place in Section ‘Vena-Contracta’ of Chapter 3.

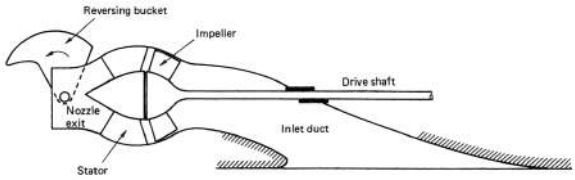

Figure 1.9 Typical waterjet general arrangement (Carlton 2007)

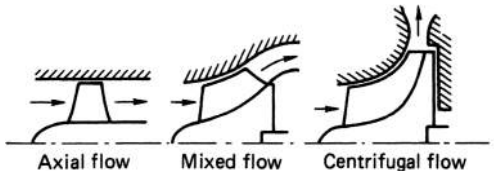

Figure 1.10 Pump impeller types (Carlton 2007)

Steering crafts propelled by waterjet systems is done either by means of a steerable nozzle (Figure 1.11) or by deflecting the direction of the discharged jet through some other installation. The angle through which the jet is directed would generally be of the order of ±30◦ (Carlton 2007). Similarly, for stopping the vessel, flaps or a ‘reversing bucket’, is employed which completely changes the direction of the jet momentum flux, as seen in Figure 1.11.

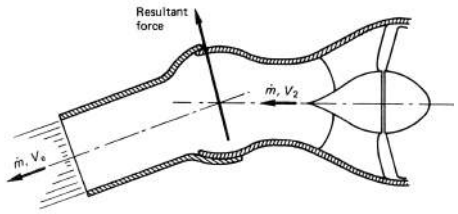

Figure 1.11 Principel of waterjet steering capability (Carlton 2007)

2 Literature Review, Motivation and Objectives

2.1 Literature Review

In reviewing the research dedicated to understanding the behaviour of waterjet propulsion systems, many interesting papers and reports have been found that each in turn reveals facts about this propulsion method. In this chapter, a thorough review of the published literature in this area is presented. The summaries reviewed are presented in a chronological order below.

Purnell (1976), raising the lower overall efficiency of the waterjet system comparing to that of propellers, discusses methods to increase the performance gains by using low momentum boundary layer flow for a wide flush intake on a waterjet propelled craft for producing the propulsion jet. The general concepts of boundary layer flow, such as boundary layer thickness, momentum velocity and energy velocity, are discussed in this report. Based on these parameters, a method of predicting pump size and overall waterjet system performance is highlighted. It is shown that applying a wider or large width/height intake area improves the overall propulsive coefficient.

Etter et al. (1981) discuss the differences between the model tests of the waterjet driven craft with propeller driven one. They have tried to define propulsion terms and experimental procedures for evaluation of the waterjet and hull performance together from tests of separate components. Also, analogies between their proposed method for waterjets are noted in comparison to the conventional propellers.

Alexander et al. (1994) performed full-scale towing and self-propulsion tests in order to determine the mechanisms of waterjet-hull interaction. They indicate that after-body pressure change due to the presence of the waterjet and jet system force component is the main reason responsible for the interaction. They point out that there exists an optimum trim angle for each hull and the forces and moments created by the jet system determine whether the trim angle of the self-propelled hull is smaller or bigger than the optimum trim angle.

Dyne and Lindell (1994) question the method of obtaining the required net thrust from a thrust deduction fraction and instead introduced a direct method giving the shaft power

without using any propulsive factor. Two different control volumes for obtaining the bare-hull and self-propelled viscous resistance directly from the momentum theorem are introduced. These viscous resistances are then applied to calculate the required net thrust to drive the vessel forward. Boundaries of the control volumes introduced are assumed to be far upstream and downstream of the hull where the flow is just in the axial direction. Moreover, for the sake of simplicity, the loss of the wake behind the model is assumed to be zero. For the bare-hull case, the wake is divided into two separate parts: First, a streamtube, which in the case of self-propulsion, passes through the ducting and the other part of the wake is a streamtube passing outside the ducting channel. The control volume applied to the self-propulsion case is slightly different and a part of the wake is passing through the ducting channel.

Roberts and Walker (1995) studied the problem of boundary layer ingestion for waterjets and developed a two- dimensional theory for waterjet propulsion systems with and without boundary layer ingestion. Due to the development of a new boundary layer right after the intake, they show that boundary layer ingestion is not always beneficial. Besides, the effect of nozzle drag on the propulsive efficiency was investigated.

Through an analytical procedure, van Terwisga and Alexander (1995) show that there is no intake drag for a flush type intake operating in a potential flow. Moreover, it is mentioned that the intake viscous drag in a viscous flow is negligibly small. It is stated that in case no longitudinal pressure gradient exists over the imaginary surface covering the intake opening, no interaction effect of the potential flow distortion by the hull on the jet performance may be detected. Finally, it is indicated that for a sufficiently large area around the flush intake, no net contribution of the intake-induced flow on the total lift force on jet-hull systems exists.

Johansson (1995) studied the vertical force acting upon a marine waterjet propulsion unit and the way such forces change the trim angle and resistance of a planing craft. A numerical two-dimensional potential flow simulation was developed to investigate the pressure distribution around the waterjet. Two separate experimental tests were planned: One was confined to the intake geometry and the other was a self-propulsion test. Results from the intake test were incorporated into Savitsky's method of predicting the performance of a planing hull. Finally, it was noticed that no vertical force is created by the action of the waterjet unit but there is a bow-down trim variation due to the waterjet moment.

Coop (1995) in his doctoral thesis, investigated the interaction between waterjet and hull using model scale and full scale measurements as well as empirical and analytical methods, which were base on the Savitsky planing performance equations and Hadler's work on propeller-hull interaction (Hadler 1966). The model developed using these methods needs a small speed dependant correction function to account for deviations between the predictions and full-scale data. He discusses the possible mechanisms contributing to the overall interaction effect and states the waterjet momentum forces causing lift and moment about the centre of gravity, the wake momentum losses and the loss of the planing surface at the intake opening as the most significant ones. A review to the methods for obtaining the nozzle momentum flux is presented in this thesis. Among these methods, a Prandtl rake is used for measuring the nozzle momentum flux in this study. Coop carried out model scale and full

scale measurements on a planing hull and obtained the thrust deduction data for these hulls. Coop reports the largest measured negative thrust deduction fractions (up to -8%) around the hump speed. During these tests the effect of the towing point variation on the thrust deduction was also studied. He states that the ITTC suggested method for towing the hull along the shaft line is the most conservative approach, which yields the highest bare hull resistance.

Kruppa et al. (ITTC 1996b) in the 21st ITTC Waterjet Specialist Committee discussed possible power prediction methods for waterjet propulsion systems. Eventually, two different methods were proposed: First, the calculation of thrust force from momentum flux and the second is the direct measurement of thrust. The capture area width is here considered to be 30% larger than the intake width and its height is twice the boundary layer thickness at this section. A 20% error in the selected width of the rectangular cross section only result in 1% error of the power predicted. The method of calculating energy velocity at the capture area, as well as the outlet section of the jet is presented. Then, based on the obtained energy velocities, the momentum flux change at these sections is defined. Moreover, internal intake losses and scaling effects are also discussed. Due to different flow patterns around the bare hull and self-propelled case, it is stated that no general relationship between them could be found.

In his thesis work, van Terwisga (1996) found that a difference between gross thrust and net thrust* may occur especially around ship speeds where the transom is not fully cleared. This difference is practically zero for higher speeds and therefore, the difference between gross thrust and bare hull resistance is a good measure of the resistance increment of the hull due to the waterjet-induced flow. Through an uncertainty analysis of propulsion tests, it was shown that that the error made in the flow rate measurement in power estimation increases with decreasing JVR. He divides the effects, which result in the resistance change of a self-propelled hull, into global and local effects. Global effects include the sinkage and trim of the hull, while a local effect is the change in the flow around the intake due to the ingested flow. Based on this classification, if the assumption of independence between the changes due to the local and the global flow is true, the change in resistance may be estimated from a linear development in a Taylor series. Based on the measurements of a powerboat propelled by a single waterjet unit, he concludes that the trim angle is the most important parameter for analysing the resistance increment of the hull.

Roberts (1998) studied the effect of boundary layer ingestion in flush type waterjet intakes both experimentally and numerically. An experimental study was performed inside a wind tunnel using two different boundary layer thicknesses. The inflow capture streamtube was found to be essentially elliptical in cross-section. The measurement section was located 20% of the intake length in front of the intake tangency point. The width varied from 1.7 times the physical width of the intake for thin boundary layers up to twice the intake width for thick boundary layers. According to this finding, the recommended 21st ITTC (ITTC 1996a) intake width, 1.3 times of the physical width of the intake, was questioned and he concluded that applying ITTC's recommended width might result in an over prediction of inflow momentum

* Definition of gross thrust and net thrust are given in Chapter 3.

flux by 8.0% for a typical high speed ferry design which consequently results in gross thrust under prediction by 9.3%.

Allison et al. (2001) studied the interaction of jet, free-surface, hull flow, and hull to investigate the resulting forces and moments through both CFD simulations and model tests. Based on a control volume for a hull with submerged nozzles and a reference frame moving with the hull, an analytical method to define inlet/hull flows for a large semi-displacement mono-hull was presented. The unmixed jet was treated as an equivalent flap with width equal to the width of the jet. The resulting lift force of the flaps was incorporated into force and moment equilibrium of the ship.

Hu and Zangeneh (2001) compared single blade-to-blade channel model and whole impeller model to investigate the flow field in the impeller and nozzle of a waterjet pump. Besides studying the effect of non-uniform inlet velocity on the impeller shaft torque, waterjet thrust calculation accuracy was analysed. Calculating the velocity distribution at the nozzle outlet and comparing its bulk average to the actual momentum velocity, an error of 0.4% in the jet momentum was reported.

Van Terwisga et al. (ITTC 2002) in the 23rd ITTC Waterjet Specialist Committee try to define a standard test procedure for waterjet systems. General comments are provided on the design procedure of waterjet elements, such as intake and pump, and the procedure to investigate the waterjet hull interaction. In order to calculate the momentum and energy flux, a different formulation is introduced compared to the formulation adopted by the 21st ITTC. In the former formulation, pressure terms are included in the definition of momentum and energy flux, which in fact is not consistent with generally accepted definitions. Referring to the 21st ITTC Waterjet Specialist Committee Report (ITTC 1996a) and van Terwisga (1996), the problem of power estimation due to error in flow rate prediction was highlighted. Intake velocity profile, as well as shape and size of the capture area were also discussed in this report. It was concluded that an imaginary rectangular capture area with a width 1.3 times larger than the waterjet intake width may be a fair estimation. However, because of the conclusion made by Roberts (1998), who claimed that the choice of rectangular capture area may lead to an under prediction of gross thrust by some 10%, it was suggested the exact shape of capture area should be obtained through CFD simulations. Considering the boundary layer thickness and scale effects, it is shown that the non-dimensional capture area in model scale is larger compared to the full scale. Moreover, considering the scale effects, the procedure to determine the tow force of the model test was discussed as well as general characteristics of the hull and corresponding waterjet geometry selected for model tests

Wilson et al. (2004) present LDV measurements of velocities for the flow around a high speed hull form. Moreover, by means of static pressure taps, the static pressure coefficient was measured at different locations on the aft portion of the model hull. To accurately determine waterjet inlet momentum flux values, a correlation of CFD-determined pressure and velocities and LDV measurements coupled with a few hull static pressure taps is proposed. Rectangular, elliptical and scalloped (bottom part rectangular, top part elliptical) shapes were tried to specify the capture area. According to the measured wake factor,

although the scalloped capture area seemed to conform best to the typical shape of the observed configuration, a simple rectangular assumption seems probably to be good enough.

Bulten and van Esch (2005), by applying a RANS solver, obtained streamtubes of ducted propellers and waterjets. Neglecting the pressure, which acts on the streamtube surface, the thrust of these propulsion units based on the momentum balance for the defined streamtube was investigated. By introducing an artificial diffuser concept, they tried to explain the contribution of the pressure force on the streamtube to the total thrust of the waterjet system.

Wilson et al. (2005) performed a waterjet propulsion test on a slender high-speed hull form model propelled by four side-by-side waterjet units. Based on the 21st ITTC Waterjet Specialist Committee recommendations (ITTC 1996a), the jet system thrust was calculated from the momentum flux change through the waterjet system control volume. Besides, some numerical investigations for both bare hull and self-propelled hull were made by means of a potential flow code capable of capturing the free surface. Waterjet intakes were represented by a flat rectangular segment of hull surface having a uniform normal velocity and sucking the flow inside the hull. A downward force was created on the aft-body of the hull due to the suction of the waterjets. This force grew larger by increasing the suction. A more detailed analysis of the balance of pressure and viscous forces on the ship aft body was suggested in order to explain the mechanism of negative thrust deduction. According to the larger Reynolds number of the ship compared to the model scale, the average velocity at the capture area in full scale will be higher than the model value. In full scale, both the non-dimensional flow rate and the jet velocity are therefore expected to increase. In order to take this increase into account, Wilson et al. employed a systematic scaling procedure proposed by Scherer et al. (2001).

Van Terwisga et al. (ITTC 2005d) on the 24th ITTC Specialist Committee on Waterjets present a comprehensive review of earlier studies on waterjet systems and ITTC standard method for waterjet system analysis. This report covers the earlier Committee suggestions including some modifications. Because of some practical difficulties inherent in direct thrust measurement, this method was off-the-list of the Committee and instead they focused on the momentum flux method. Powering characteristics and the efficiency of the whole waterjet system and its elements are also discussed. Separate interaction terms are then introduced for momentum, energy, thrust and drag. Formulations for obtaining the delivered thrust and corresponding power required through conservation laws of momentum and energy are articulated. Two different thrust deduction fractions are introduced, one relating bare hull resistance to net thrust, the other expressing the relationship between gross thrust and net thrust. The sum of these thrust deduction fractions is set to be equal to the total thrust deduction fraction. By introducing a correction factor for momentum velocity at the capture area, a formulation for obtaining a change in momentum flux is presented. In the absence of any detailed information about the capture area, an elliptical capture area 1.5 times wider than the geometrical intake width is recommended. More over, it is mentioned that just the intake centreline boundary layer profile will be sufficient while employing an elliptical capture area. The procedure for scaling the data obtained from the model scale to the full scale is also presented. Finally, results of self-propulsion tests both on bare hull and self-propelled hull are presented and discussed.

Hyo et al. (2006) measured the three dimensional velocity field at the intake opening and at the nozzle exit using a stereoscopic PIV system. The velocity at the intake opening is smaller in the vicinity of the intake ramp in comparison to the velocity close to the lip due to thicker boundary layer close to the intake ramp and the geometry of the lip. The causes of different sizes of counter-rotating vortex pairs, which are observed at the nozzle exit, are discussed in this paper.

Bulten (2006) studied the flow inside waterjet propulsion systems employing CFD tools. Indicating the non-uniform velocity field at the pump section, different reasons were introduced as the causes of this non-uniformity. Non-uniform velocity distribution just before the intake due to the developing boundary layer, passing through the bend inside the ducting channel and the rotating shaft, were cited as the main cause of the flow non-uniformity at the pump inlet section. Three separate steps were taken to model the waterjet flow. First, the flow inside the ducting channel was modelled to obtain the non-uniform flow field just before the pump section. In order to investigate the effect of uniform and non-uniform flows at the pump inlet section, the flow inside the pump was modelled by employing both a quasi-state multiple frame of reference (MFR) method and a fully transient moving mesh method. Both these methods predicted almost the same head and power. Studying the unsteady forces on the impeller due to rotor-stator interaction it was shown that the magnitude of the radial interaction force depended on the flow rate though the pump. Eventually, both validated numerical models of the inlet and the pump were combined to simulate the complete waterjet installation. The integration of axial force component on the solid wall with a simplified version of the integral momentum balance equation was applied to calculate the thrust. A clear deviation between the results of these methods was reported for higher ship speeds. Also, a large vertical force was reported at the same range of speed. According to these findings, Bulten concluded that the method based on the momentum balance for the streamtube control volume was incorrect possibly because of the influence of the hull in the vicinity of the waterjet inlet and partly because of neglecting the contributions of the pressure distribution acting on the streamtube.

A comprehensive measurement campaign was completed by the Commercial Deployment of Transportation Technologies (CCDoTT) (Cusanelli et al. 2007) on a demi-hull with a pair of waterjet units. The data presented in this report can be used to validate numerical simulations. The difference of boundary layer thickness due to scale change was taken into account in the data scaling procedure. Consequently, although the thrust deduction fraction was positive in the model scale, taking this correction into account resulted in a negative thrust deduction fraction. This conclusion raises the question of whether the thrust deduction is dependent on scaling or not.

Jessup et al. (2008) accomplished a comprehensive set of experiments applying LDV and pitot-static tubes to investigate the velocity field and static pressure for three hull variants to study the effect of different propulsors. The first hull design was adapted to four propellers with open shaft and strut appendages. The second and third hull designs were intended for axial and mixed flow waterjets. Hulls designed for axial flow waterjets normally have a narrower and shallower transom compared to hull designs for mixed flow waterjets. Although the overall thrust of the axial flow waterjet unit was smaller compared to the mixed

flow waterjet unit, a negative thrust deduction fraction was reported for the hull with mixed flow waterjet units.

Hino and Ohashi (2009) applied CFD analysis to free surface flow around a waterjet propelled ship. An actuator disk with a constant body force distribution was employed to model the propulsor. The sinkage and trim angle of the hull were fixed during the computation due to the measured data obtained from experiment. Doing a backward trace of streamlines from the actuator disk plane, they found out that the capture area was twice as wide as that of the intake duct; almost 30% larger than the ITTC recommended value.

Delany et al. (2009) using a RANS method studied the performance of two different high-speed hull forms at model scale and full scale. The aft part of the hulls were shaped to accommodate axial flow or mixed flow waterjet units. The evaluation of the waterjet performance is based on the ITTC 1996 suggested method. The jet momentum flux obtained from the measurements in combination with the computed ingested momentum flux are used for calculation of the gross thrust in the computation. It is shown that the capture area of the mixed flow waterjet is shallower and wider comparing to that of the axial waterjet. Therefore, the efficiency of the mixed flow waterjet is improved because of ingesting more low momentum fluid inside the boundary layer. The computed and the measured gross thrust at model scale differs by 4% which is stated to be due to the different capture area geometry used in the computation and in the measurement. Analyzing the flow ahead of the pump inlet section for ducting channel without shaft, with non-rotating shaft and with rotating shaft reveals the flow energy for all these conditions are the same. However, the velocity distribution for each of these cases is somewhat different. Rhee et al. (2009) used the same RANS code for computing the flow around the same bare hull and waterjet-propelled hull using overset grids but different mesh generation technique. In both of the studies carried out by Delany et al. (2009) and Rhee et al. (2009) the capture area of the waterjet is estimated by back streamlines entering the pump.

Skipping the detailed flow modelling inside the ducting channels, Kandasamy et al. (2010) derived an integral force/moment waterjet model and applied it to a CFD code to predict ship local flow and powering. In order to circumvent the difficulties of obtaining the intake capture area of the waterjet system, a control volume other than the control volume proposed by ITTC was applied for balancing force and moment. The maximum error of the simulated cases compared to experimental data was for the trim angle of the bare hull and self-propelled hull, which was almost 14% on the average. Although the predicted resistance error for the bare hull and self-propelled hull was less than 5%, the calculated thrust deduction fraction showed a larger deviation from the data measured.

Through the URANS approach and applying body force to model the pump effect, Takai (2010) solved and analysed flow fields for bare hull and self-propelled high-speed sea lift hull over a speed range. Moreover, duct shape optimisation was accomplished in two separate stages. The upper curvature and lip shape modification reduced mainly minor pressure loss. Next, some effort was made to reduce the major loss principally due to friction drag in duct. Therefore, duct intakes were merged into each other in order to reduce the

surface area of the intakes. Computational results based on the latter optimised intake showed improvement in inlet efficiency. Part of this work is also published in (Takai et al. 2011).

Ding and Wang (2010) state that by applying conventional methods, intake loss is overestimated which results in overestimation of overall power. To overcome this problem, they introduce a method to determine the waterjet system flow loss by means of CFD. In this method, by dividing the surface between the internal flow ingested into the inlet duct and the external flow beneath the hull, an attempt to capture a virtual stream-tube is made. Based on the obtained stream-tube, the flow loss is calculated according to the difference of total head between the duct outlet and the capture area ahead of the intake. They showed that the flow loss coefficient is approximately in the range of 0.05 to 0.12 for typical flush-type inlet duct, which is less than the empirical value of 0.2 to 0.3. Moreover, they mention that the shaft had a big influence on the flow loss.

Aiming at performance analysis of existing waterjet designs as well as design optimization of new designs of high-speed craft, Kandasamy el al. (2011) employed a RANS method and an actuator disk body-force model for modeling the pump. The results of the computation are compared with the measured data obtained from model testing using the ITTC'05 procedure. The importance of the measurement facility bias error is highlighted in this paper and some further quantification of the measurement technique bias error are planned to carry out. The computed bare hull resistance is under-predicted by almost 2.5% in comparison to the measured value. The flow rate is under-predicted by almost 3% which is half the error computed by Takai et al. (2011) employing the same code with multiple overset grids in the duct region. The improvement of the flow rate accuracy is attributed to applying a single grid inside the ducting channel instead of the overset grid in the previous work which introduced interpolation error. The computed and the measured thrust deduction fraction in the speed range $0.4 < Fn < 0.7$ varies almost between 0.16 and 0.08. It is stated that the waterjet induced sinkage and trim increases the resistance by 4%, which does not account for all the waterjet hull interaction effect.

Peri et al. (2012) presented a simulation based design toolbox based on RANS method for optimizing a high-speed waterjet propelled catamaran (Delft Catamaran). Using different evolutionary type optimization algorithms they have solved both single and multi-objective optimization problems. In order to reduce the intake losses, the ducting channel geometry is optimized. The hull geometry is optimized for the resistance. Employing the optimization tool the total resistance is reduced by 6%. By combining the high fidelity solver with a low fidelity one the costs of the computation is reduced by 50%.

2.2 Motivation and Objectives

As seen in the literature review the physics behind the waterjet/hull interaction is not fully understood. A particularly interesting effect, which has intrigued the hydrodynamicists for a long time, is the negative thrust deduction reported for several hulls. Since this is of great importance for the waterjet design, one of the leading manufacturers of waterjet systems, Rolls-Royce AB in Sweden, proposed a project on waterjet/hull interaction to be carried out within the University Technology Centre at Chalmers, sponsored by Rolls-Royce AB.

The objective of this project was twofold:

- To gain further insight into the physics behind the waterjet/hull interaction. In particular the negative thrust deduction should be investigated. Why does it occur, and under which circumstances?
- To develop a rapid, yet reasonably accurate method for estimating the gross thrust of a waterjet driven hull.

2.3 Structure of the Thesis

After an introduction to the subject in Chapters 1 and 2 the theory of waterjet/hull interaction is presented in Chapter 3, which also includes a classification of all effects contributing to the difference between the bare hull resistance and the gross thrust. Next a numerical technique for studying the waterjet/hull interaction is proposed. It is called the Pressure Jump Method and is based on non-linear free-surface potential flow theory. The presentation and validation of this method is given in Chapter 4. Then in Chapter 5, the Pressure Jump Method is applied for estimating the hull resistance increment due to the waterjet effects. Moreover, in this chapter, simplifying the hull geometry to a flat plate, general relations for the sinkage and trim changes due to the waterjet-induced flow for different hull and intake geometries are obtained. A technique for viscous flow computations for the bare hull is presented in Chapter 6. Then in Chapter 7, this method is applied for studying the transom clearance phenomenon. A method used for the self-propelled hull viscous flow computation is presented and in Chapter 8 and in Chapter 9, this method is employed for understanding the waterjet/hull interaction effects more in detail. Finally, in the last Chapter, the conclusions from all other chapters are collected.

3 Theory

The thrust and powering of a waterjet unit is always related to the momentum flux change through the waterjet system. Like for conventional propellers, it would have been more straight forward if the powering and thrust of the waterjet unit were expressed explicitly as the net thrust of the unit. But why is it not so common to provide the net thrust of a waterjet unit? The answer is tied closely to the limitations of the current measurement methods. The net thrust of a waterjet unit transmits to the hull through different contact surfaces with the hull and not just through the shaft line, which is the case for a propeller. In the early days of waterjet testing at MARIN (Coop 1995; van Terwisga 1996) and more recently at Rolls-Royce AB, it has been tried to measure the net thrust of a waterjet unit by mounting the waterjet unit on a force measuring frame and using flexible connections between the waterjet unit and the hull so the entire thrust of the jet system could be exerted on the force measuring frame. The sketch of the setup used at MARIN is shown in Figure 3.2. In this method the entire waterjet unit needs to be suspended. The weight of the unit can affect the thrust force measured from such a suspended frame to a large extent. Furthermore, since the forces and moments from the waterjet unit are transmitted onto the hull, the direct interaction between the hull and the waterjet unit cannot be measured. These reasons, besides the expensive costs of such a setup, makes the direct measurement of the net thrust of a waterjet unit unattractive at the moment. Thus, the momentum flux change through the waterjet system is used for defining the characteristics of such units.

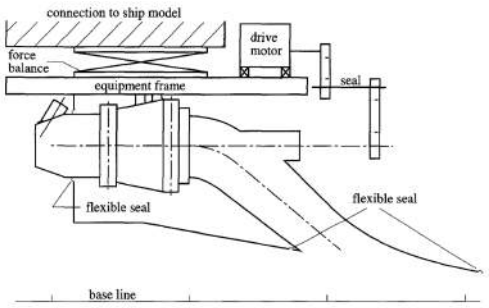

Figure 3.1 Test set-up for compete model of waterjet system (van Terwisga 1996).

In this chapter general definitions such as the net thrust, the momentum flux change through the control volume of the waterjet system and the thrust deduction fraction, which are frequently used in waterjet system analysis, are introduced. Most of the definitions and formulations in this chapter are taken from reports of the ITTC Specialist Committee on Waterjets (ITTC 1996a; ITTC 2002; ITTC 2005d; ITTC 2005a) and (van Terwisga 1996).

3.1 Momentum Flux

The waterjet propulsion concept is based on the thrust force gained from the momentum flux change through the system. Low speed velocity enters the system through the capture area. Inside the ducting channel the pump adds momentum to the entrained water and, thereafter, a high-speed jet is spewed out through the nozzle. Writing the momentum flux balance for a control volume gives the resultant force acting on this control volume. In general, momentum flux vector, *M*, in *i* direction over a control volume is defined as follows,

$$\bar{M}_i = \iint_A \rho u_i (u_k n_k) dA, \qquad (3\text{-}1)$$

where ρ is the density of the fluid, u is the velocity vector and n is the unit vector normal to the control volume surface.

3.2 Surfaces and Control Volume

Figure 3.2 shows the cross section of a waterjet propulsion unit and the control volume, which is normally applied for the system analysis. The numbering of the surfaces shown in Figure 3.2 is the same as those introduced by van Terwisga (1996).

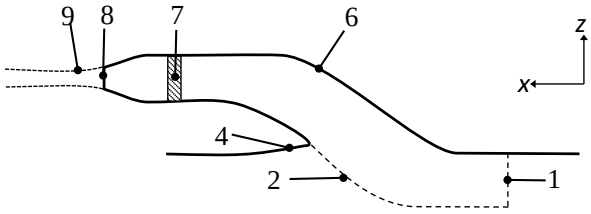

Figure 3.2 Section cut through the waterjet ducting system

Surface 1 is named the capture area. According to the ITTC Waterjet Specialist Committee (ITTC 2005d) it should be located “far enough in front of the intake ramp tangency point, before inlet losses occur”. As a practical solution, the Committee recommends one inlet length forward of the ramp tangency point (ITTC 2005d). Surface 2 in Figure 3.2 shows the dividing streamtube. This streamtube is an imaginary surface, which separates the flow drawn into the ducting system from the rest of the flow field. According to the definition of streamtube, no flow crosses this surface. Surface 4 is part of the ducting channel which lies outside the streamtube (i.e. the surface between the stagnation line on the intake lip and the line where the ducting channel merges with the hull) and surface 6 is the waterjet system internal material boundaries. Surface 7 is the boundary area of the pump control volume and surface 8 represents the nozzle discharge area. If the nozzle discharge is designed such that all the outgoing streamlines are parallel with the nozzle exit direction, the pressure at the nozzle exit would be atmospheric otherwise the atmospheric pressure will occur at another

section downstream of the nozzle exit. This section, which the jet reaches its minimum diameter, is called vena-contracta and is marked as surface 9 in Figure 3.2. Surface 3 and 5 are added to this figure in Appendix B.

3.3 Thrust and Thrust Deduction

Having defined the control volume, and considering the coordinate system, *x*, *y*, *z*, to be Cartesian and earth fixed (as shown in Figure 3.2), the thrust force exerted on the control volume may be obtained by applying the momentum conservation law over that control volume. The change in momentum flux over a certain control volume is equal to the sum of the forces acting on that control volume.

$$\iint_{A_1+A_8} \rho u_i (u_k n_k) dA = \iint_{A_1+A_2+A_6+A_8} \sigma_{ij} n_j dA + \iiint_{V_7} \rho F_{pi} dV + \iiint_{V} \rho F_i dV \qquad (3\text{-}2)$$

where,

$\iint_{A_1+A_8} \rho u_i (u_k n_k) dA$: net momentum flux through control volume

$\iint_{A_1+A_2+A_6+A_8} \sigma_{ij} n_j dA$: external force acting on surface of control volume

$\iiint_{V_7} \rho F_i dV$: body force on control volume

$\iiint_{V} \rho F_{pi} dV$: pump force acting on fluid

The normal vector *n* points out of the control volume; hence when the velocity vector, *u*, exits the control volume the product of $u \cdot n$ is positive and when the velocity vector is entering the control volume this product becomes negative.

σ_{ij} is the tensor showing the external forces acting on the control volume. This tensor can be split into two parts as shown in Equation (3-3).

$$\sigma_{ij} = -p\delta_{ij} + \tau_{ij}, \qquad (3\text{-}3)$$

where p is the time averaged pressure and τ_{ij} is the shear stress tensor. δ_{ij} is the Kronecker delta defined as follows:

$$\delta_{ij} = \begin{cases} 1 & if \quad i = j \\ 0 & if \quad i \neq j \end{cases} \qquad (3\text{-}4)$$

The gross thrust, $\vec{T}_g$, is defined as "the force vector pertinent to the change in momentum flux over the selected control volume, acting on its environment" (van Terwisga 1996). This is basically the definition of the first term on the left hand side of Equation (3-2). The gross thrust is a force vector but since the horizontal component of this vector is more important, shortly, this component of the gross thrust, $T_{g,x}$, is called the gross thrust, T_g (Equation (3-5)).

$$T_g = -\iint_{A_1+A_8} \rho u_x (u_k n_k) dA \qquad (3\text{-}5)$$

Since the gross thrust is the reaction force exerted by the control volume on its environment, the minus sign in the term to the right makes the gross thrust point in the same direction as the net thrust.

Considering the material boundaries of the waterjet system, another thrust force may be defined. "The net thrust, $\vec{T}_{net}$, is defined as the force vector acting upon the material boundaries of the waterjet system, directly passing the force through to the hull" (van Terwisga 1996). From now on, the horizontal component of the net thrust vector is going to be called the net thrust, T_{net}, which is defined as Equation (3-6).

$$T_{net} = -\iint_{A_4+A_6} \sigma_x dA - \iiint_{V_7} \rho F_{px} dV \qquad (3\text{-}6)$$

Since the surface normal vectors of the control volume point out of the flow control volume, there is a need to use minus signs for the terms on the right hand side.

It should be noted that the thrust deduction fraction, t, is not the same as the conventional thrust deduction fraction, t, employed in the propeller/hull interaction theory. For a conventional propeller, t relates the resistance of the bare hull, R_{bh}, to the net thrust required for driving the hull at a certain Froude number; but for a waterjet driven hull the thrust deduction fraction relates the resistance of the bare hull to the gross thrust, which is defined as follows,

$$t = 1 - \frac{R_{bh}}{T_g}. \qquad (3\text{-}7)$$

Using the ratio of the bare hull resistance to the net thrust of the waterjet system, it is possible to define a fraction which is similar to the definition of the thrust deduction fraction employed in conventional propeller/hull theory which reads as follows,

$$t_r = 1 - \frac{R_{bh}}{T_{net}}. \qquad (3\text{-}8)$$

Basically the net thrust of a waterjet unit is equal to the resistance of the self-propelled hull and therefore the resistance increment fraction, as it is obvious from its name, reflects the change in the resistance of the waterjet-propelled hull compared to the bare hull resistance.

Employing the definitions for the net thrust and gross thrust, the *x*-component of Equation (3-2) may be rewritten as follows,

$$-T_g = -T_{net} + \iint_{A_1+A_2+A_8} \sigma_x dA - \iint_{A_4} \sigma_x dA. \qquad (3\text{-}9)$$

In order to relate the net thrust to the gross thrust, a jet thrust deduction fraction is defined as follows,

$$t_j = 1 - \frac{T_{net}}{T_g}. \qquad (3\text{-}10)$$

By applying the definitions of the net thrust and gross thrust in Equation (3-10), t_j reads as follows,

$$t_j = -\frac{1}{T_g}\left[\iint_{A_1+A_2+A_8} \sigma_x dA - \iint_{A_4} \sigma_x dA\right]. \qquad (3\text{-}11)$$

Positive jet thrust deduction fraction means that the net thrust is smaller than the gross thrust and vice versa. This will be discussed in detail in Chapter 9.

The combination of Equations (3-10) and (3-8) gives the following equation:

$$T_g(1 - t_j)(1 - t_r) = R_{bh}. \qquad (3\text{-}12)$$

Combining Equation (3-12) and Equation (3-7) yields,

$$t = t_r + t_j - t_r \cdot t_j. \qquad (3\text{-}13)$$

In the literature which has been published so far, it has been stated that t_j value is negligibly small except at the transom clearance Froude number and therefore the second order terms on the right hand side of Equation (3-13) can be neglected ((van Terwisga 1996), (ITTC 2005d) and (Eslamdoost et al. 2014b)). In Section 9.2.3 it will be shown that t_j has considerably large values when the nozzle exit is not ventilated and therefore the second order term in Equation (3-13) cannot be neglected.

3.4 Intake and Exit Drag

So far the definition of the gross thrust and the net thrust as well as the thrust deduction fraction, the resistance increment fraction and the jet thrust deduction fraction are defined. In this section the terms which appear in the equation showing the difference between the net thrust and the gross thrust (Equation (3-9)) are split into two major components which are caused by the intake and the exit flow of the waterjet system. The integrals over the surfaces A_1, A_2 and A_4 together define the intake drag, D_i,

$$D_i = -\iint_{A_1+A_2} \sigma_x dA + \iint_{A_4} \sigma_x dA, \qquad (3\text{-}14)$$

while the integral over the surface A_8 defines the exit drag, D_e,

$$D_e = -\iint_{A_8} \sigma_x dA. \qquad (3\text{-}15)$$

Thus the gross thrust is equal to the net thrust plus the intake and the exit drag,

$$T_g = T_{net} + D_i + D_e. \qquad (3\text{-}16)$$

Van Terwisga (1996) shows that the intake drag is zero for free-stream conditions However, for operational conditions it will not be zero for several reasons:

- The intake velocity is not undisturbed.
- There is a pressure gradient along the surface A_2 caused by the finite dimensions of the hull.
- There is a pressure gradient along the surface A_2 caused by the free surface waves.

The first effect was quantified by van Terwisga in potential flow, but his relation cannot be applied in viscous operational conditions. A more thorough investigation of the three effects under operational conditions should be most valuable.

The exit drag is zero if the pressure at the jet exit is atmospheric. This will happen in case that all the streamlines at the jet discharge section are parallel with the nozzle exit and the jet is expelled into the air. At very low speed the water does not clear the transom and the nozzle exit is partly below the surface in the dead-water zone. There is thus a hydrostatic pressure over part of the exit. When the speed increases, the water will clear the transom, but if the speed is not high enough the stern wave may be so steep that the nozzle protrudes the wave, resulting in a disturbed exit pressure. For a sufficiently high speed the wave slope becomes large enough for the exit to be entirely in the air and provided that the streamlines at the nozzle exit are parallel[1], the exit drag is zero.

Obtaining the stress tensor on the capture area, A_1, the dividing streamtube, A_2 and the lip A_4 is not straight forward, especially by means of experimental methods. Numerically, it is possible to detect the surface of the streamtube and capture area to extract the forces exerted on them, something that has been accomplished by Bulten (2006) and Jiang-Ming et al. (2010). Bulten (2006) concluded that the momentum balance for the streamtube control volume does not represents the net thrust of the waterjet system but van Terwisga (1996) mentioned that for higher ship speeds, the momentum flux change through the waterjet system might be a good measure for the resistance increment of the hull since t_j is normally much smaller than t_r. In Chapter 9 the intake and the exit drags are computed numerically over a range of Froude number. This makes it possible to analyse the discrepancy between the gross thrust and the net thrust more in detail.

3.5 Capture Area

Water enters the ducting system through area 1, which is called the capture area. Sometimes, it becomes cumbersome to obtain the exact shape of the capture area and, therefore, there are some assumptions for simplifying the shape. Two of the most conventional assumptions for the shape of the capture area are a rectangular or half-elliptical shape which, according to the ITTC Waterjet Specialist Committee should be placed one impeller diameter ahead of the intake tangency point (ITTC 2002), (ITTC 2004b). Kruppa et al. (ITTC 1996a), van Terwisga [1996a] and Scherer et al. [2001] observed that in the range of intermediate to high Froude numbers, the width of the capture area is almost constant; hence, in order to reduce

[1] The possibility of having parallel streamlines at the nozzle exit seems to be unlikely for most nozzles.

the number of variants, the width of the capture area, w_{capt}, is considered to be a constant value which is a function of intake geometry width, w. Empirical widths of the rectangular and half-elliptical capture areas are shown in Figure 3.3. Height of the capture area, h, is varying based on the flow rate through the system and it is a bit higher in half-elliptical intake geometry compared to the rectangular one.

Figure 3.3 Two different assumptions for the capture area geometry (ITTC 2002)

The geometry of the rectangular or elliptical capture area may be defined by the following function (van Terwisga 1996).

$$\left(\frac{z}{h}\right)^r + \left(\frac{y}{\frac{1}{2}w_{capt}}\right)^r = 1, \qquad (3\text{-}17)$$

where r defines the shape of the capture area. For r=2 it becomes a function which defines a semi-ellipsoid and for r>100, it practically defines a rectangle. Different curves obtained from the variation of r are plotted in Figure 3.4.

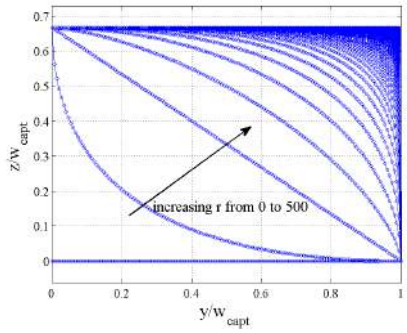

Figure 3.4 Effect of r on the curve representing the capture area

In contrast to the findings showing the validity of choosing simple intake geometry, Roberts and Walker (1995), using a rectangular capture area, measured the gross thrust as being 10% lower than the thrust obtained using the shape of the actual capture area. Finding out the exact shape of the capture area might be tricky in experiments; however, by employing CFD there are methods to calculate the exact shape. Backward tracing of the streamlines from the impeller surface is one alternative way (Figure 3.5). Another method based on concentration scalar divides the computational field into two different parts. One part is the flow, which passes through the impeller section, while the other represents the rest of the flow; the surface separating these zones defines the boundaries of the intake streamtube and is captured through a post-processing procedure when the flow field solution is converged ((Bulten 2006), (Ding & Wang 2010)).

Figure 3.5 Backward tracing of the streamlines for obtaining the capture area; left: side view and right: stern view. The dashed line shows the rectangular capture area.

3.6 Jet Flow

In this section, the jet profile and the axial velocity distribution across the nozzle discharge are going to be discussed. Although, after the impeller, there exists a stator inside the nozzle chamber to remove the swirl of the jet, some tangential component of the velocity is still detected in the discharged jet. Moreover, the effect of employing the bulk average velocity for obtaining the jet momentum flux instead of momentum velocity is addressed in this section. Besides, there will be some discussion on the position of vena-contracta of the jet.

3.6.1 Swirling Jet Flow

Measurements of the axial velocity of swirling jets show that there are retarded flow regions both in the centreline and close to the outer surface of the jet. The axial flow is well described in the following equation (ITTC 1996a),

$$\frac{u_{8,x}}{u_{8,x\,max}} = \left\{1 - \left(\frac{r}{R}\right)^{n} - k\left[1 - \left(\frac{r}{R}\right)^{\frac{3}{2}}\right]^{12}\right\}, \qquad (3\text{-}18)$$

where r is the jet radius; R shows the maximum jet radius. n and k are constants which determine the quantity of retarded flow close to the swirling jet outer surface and centreline of it, respectively. The effect of different n and k can be seen in Figure 3.6. When n goes to infinity, the axial velocity profile becomes more flat at regions close to the outer surface. k values close to zero have the same effect on the jet velocity close to the centreline.

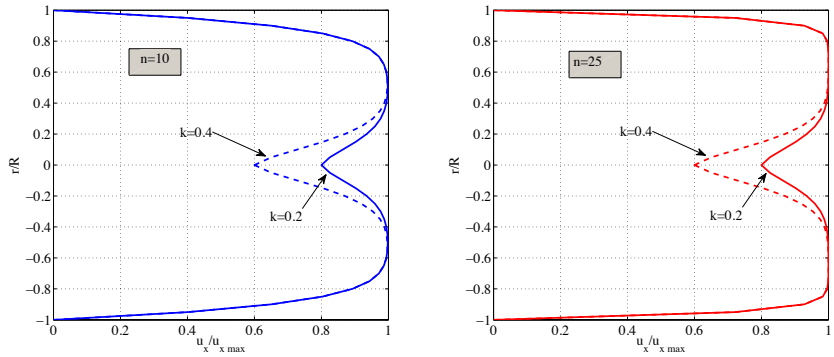

Figure 3.6 Typical axial velocity profile of a swirling jet for different values of n and k.

A sensitivity analysis (ITTC 1996a) shows that a moderate rotation has minor effects on the power prediction of the jet system. The slight change in the momentum flux is because of the

change in the static pressure of the jet due to the swirl. The pressure reduction due to swirl, Δp_{swirl}, may be obtained from,

$$\Delta p_{swirl} = -\rho \cdot \int_0^R \frac{u_{8\phi}^2}{r} dr, \qquad (3\text{-}19)$$

where $u_{8\phi}$ is the tangential velocity of the jet. r is the radial distance from the jet centre and R is the jet diameter (ITTC 1996a).

3.6.2 Vena-Contracta

The vena-contracta of an incompressible jet flow represents the section of the jet in which the average static pressure is identical to the ambient pressure. Depending on nozzle design, vena-contracta may occur at the nozzle discharge section or further downstream. Normally the parallel part of the nozzle exit geometry is not so long and therefore the streamlines at the exit will not be parallel with each other and there will be a pressure gradient in the radial direction of the jet. Thus, the possibility of vena-contracta occurring further downstream rather than the nozzle exit section is higher. According to the proposed method by 25th ITTC (ITTC 2005a), for nozzle designs with the vena-contracta, momentum flux may be measured at the nozzle discharge where its diameter may be accurately measured. Then, bollard pull calibration procedure can be applied to cancel the possible errors due to this assumption. This calibration yields a relationship between the flow rate and jet thrust.

3.7 Momentum Flux Correction

According to the previous section, the axial velocity of the jet flow at the nozzle discharge is non-uniform. Due to the existing boundary layer profile at the capture area, the axial velocity at this section is not uniform neither. Hence, using the average axial velocity for obtaining the jet axial momentum flux causes some error, which should be corrected by introducing a dimensionless momentum flux correction factor, c_m. The axial momentum flux correction coefficient is a measure of the velocity squared non-uniformity on a certain surface and is defined as follows,

$$c_m = \frac{1}{A_x} \iint_{A_x} \left(\frac{u_x}{\bar{u}_x}\right)^2 dA_x, \qquad (3\text{-}20)$$

where $\bar{u}_x$ is the mean axial velocity and u_x is the local axial velocity through surface with the projected area of A_x to the yz-plane. The axial momentum flux correction coefficient will be equal to 1 in case that the velocity distribution is uniform, otherwise it will be larger than 1(White 2008).

Employing the axial momentum flux correction coefficient, the equation showing the gross thrust of a waterjet unit (Equation (3-5)) yields,

$$T_g = \rho Q c_{m8} \bar{u}_{8_x} - \rho Q c_{m1} \bar{u}_{1x}, \qquad (3\text{-}21)$$

where ρ is the water density, Q is the volumetric flow rate through the nozzle. $\bar{u}_{1x}$ and $\bar{u}_{8x}$ are the mean axial velocity through the capture area and the nozzle discharge section, respectively.

Modelling the entire impeller geometry, Hu and Zangeneh (2001) calculated the velocity distribution at the nozzle outlet and compared its area weighted average to the actual momentum velocity to obtain c_m. They reported a momentum flux correction factor of c_m=1.000386 which means that there will be an error of approximately 0.4% in case the area weighted average velocity ($\bar{u}_x{}^2$) is employed for the momentum flux calculation instead of the momentum velocity ($u_x{}^2$).

Assuming that the momentum flux correction coefficient at the nozzle exit and at the capture area are equal to 1, Equation (3-21) simplifies as follows,

$$T_g = \rho Q u_0 (NVR - IVR), \qquad (3\text{-}22)$$

where NVR (Nozzle Velocity Ratio) and IVR (Intake Velocity Ratio) are the ratio of the mean axial velocity at the nozzle exit section and the mean axial velocity at the capture area to the undisturbed velocity, u_0, respectively. In Section 8.5.3, the momentum flux correction coefficients at the capture area, at the nozzle exit and at the vena-contracta are computed for different operating conditions of the waterjet system. Employing the computed c_m values, it would be possible to estimate the imposed error on the gross thrust when the momentum flux correction coefficients are assumed to be equal to 1.

3.8 ITTC Recommended Procedure

In the recommended procedures and guidelines of the 24th ITTC Specialist Committee on Waterjet (ITTC 2005b) the procedure for the propulsive performance prediction of a flush intake waterjet unit is outlined. The self-propulsion test, mentioned as the “momentum flux” method and data scaling method are encompassed in this technique. A short description of the procedure is presented in the following.

In order to obtain the same displacement and initial trim angle for the bare hull and waterjet driven hull, the ITTC Specialist Committee on Waterjet suggests using the same hull with the waterjet unit mounted, the intake opening covered and the ducting channel filled with water during the resistance test. The intake and nozzle geometries should be scaled to ensure the similar flow condition at the capture area and the nozzle exit in full scale. As long as the kinematic similarity of the waterjet unit incoming and outgoing flow is ensured, any pump of convenience can be used.

The trickiest quantity to measure in the “momentum flux” method is the flow rate and the entire procedure is very sensitive to errors in it. There are several methods to measure the flow rate, and two of them are discussed in the ITTC procedure. The first one is obtaining the average static pressure at two sections of the nozzle by means of Differential Pressure Transducers (DPTs) and the other is the measurement of velocities in a cross sectional plane by means of Laser Doppler Velocimetry (LDV). The measured differential pressure from the DPTs needs to be calibrated with the flow rate and this can be carried out in a bollard pull test. However, an externally exposed pressure difference (e.g. due to the submergence of the nozzle exit) can affect the flow rate calibration.

Having the flow rate at hand, one needs to know the position and the area of vena-contracta to obtain the total outgoing momentum flux. According to the ITTC recommended procedure, if the nozzle outflow is parallel, it can be assumed that the vena-contracta has the same diameter as the nozzle discharge. For a real nozzle geometry this condition is seldom satisfied and therefore this assumption can affect the measured outgoing momentum flux to a considerable extent.

In order to obtain the ingested momentum flux at the capture area the boundary layer profile at the capture is required. The velocity profile can be either measured, computed from CFD or estimated from a semi-empirical formula. The capture area should be located in front of the intake tangency point before inlet losses occur. Based upon a data survey it is stated that the normalized boundary layer profile at the capture area is almost uniform in the transverse direction; hence it would be sufficient just to measure the boundary layer profile at the centreline. The shape of the capture area is required for obtaining the ingested momentum flux by the integration of the velocity profile over this area. The exact shape of the capture area and the velocity distribution over this surface can be computed through a CFD simulation; but if measurements are used for obtaining the momentum flux it is suggested to measure the velocity profile at the centre line and then assuming a rectangular or a half-elliptical shape of the capture area. Empirical widths of the rectangular and half-elliptical capture areas are 1.3 and 1.5 times the intake width, respectively. The consequences of selecting each of these area shapes are discussed in the proceedings of the 23rd ITTC (ITTC 2002). After obtaining the average velocity and the momentum correction coefficient at the capture area and at the vena-contracta, Equation (3-21) can be used for the calculation of the waterjet system gross thrust.

3.8.1 Modification to the ITTC Recommended Procedure

According to the procedure suggested by the ITTC Specialist Committee on Waterjets, the momentum flux is obtained at the vena-contracta and therefore there will be no exit drag. In the lower speed range where the nozzle is not fully ventilated, there will be no jet cross section with atmospheric static pressure, and therefore, instead of obtaining the momentum flux at the vena-contracta the momentum flux at the nozzle exit is used for the gross thrust calculation. In such a case, the contribution of the non-atmospheric pressure at the nozzle exit is introduced as the exit drag. Thus, in this method, the calculation of the exit momentum flux is not consistent between submerged and ventilated cases. In order to be consistent over the different speed ranges, in this thesis, the exit momentum flux is obtained at the nozzle exit section, and the non-atmospheric pressure at the nozzle exit, which can be due the nozzle submergence and/or non-parallel jet flow streamlines at the nozzle exit, is treated as exit drag[1].

[1] In Chapter 4 it is assumed that the pressure at the nozzle exit is atmospheric. Consequently, the exit drag would be zero.

3.9 Contribution of Different Parameters to Thrust Deduction

Conventionally, the total thrust deduction factor for a waterjet-propelled hull is defined as the ratio between the gross thrust of the waterjet system and the bare hull resistance. The gross thrust, in fact, is the horizontal component of the momentum flux change through the waterjet system. For a normal propeller, the thrust deduction factor is defined as the ratio between the net thrust and the bare hull resistance. The reason for introducing a different thrust deduction definition than that of conventional propellers is that there are some practical impediments in measuring the net thrust of a self-propelled hull, but it is much easier to measure the gross thrust of a waterjet unit. Measuring the force transmitted through the propeller shaft gives the net thrust of the propeller; but for the waterjet system, it is not only the impeller shaft, which transmits the thrust force to the hull; a proportion of the thrust is also transferred to the hull through the ducting channel. It is no easy task to measure this transmitted force. Instead, measuring the momentum flux change, which provides the gross thrust of the unit, seems more practical and achievable. In this Chapter, based on the definitions of the net and gross thrust (Section 3.3), the possible parameters linking the bare hull resistance to the gross thrust of the self-propelled hull are identified. Then, the contribution of each of these parameters to the resistance of the hull is discussed. Knowing the magnitude of each single parameter separately helps to understand the physics behind the thrust deduction and may aid in the optimization of the hull/propulsor configuration. Also it may shed some light on the reason for the negative thrust deduction fractions sometimes found on waterjet driven hulls.

3.9.1 Flowchart Showing the Relation between Bare Hull Resistance and Gross Thrust

A summary of the items engaged in the thrust deduction analysis of a waterjet-propelled hull is presented in the flowchart given in Figure 3.7. It is the bare hull resistance and the gross thrust that finally needs to be compared. These two items appear on the top and bottom of the flowchart, respectively. All other items appearing in-between the bare hull resistance and the gross thrust are contributing to the total thrust deduction fraction.

The flowchart can be split into two major parts; the part connecting the bare hull resistance to the net thrust and the part relating the net thrust to the gross thrust. These parts define the thrust deduction fractions t_r and t_j (see Section 3.3), respectively.

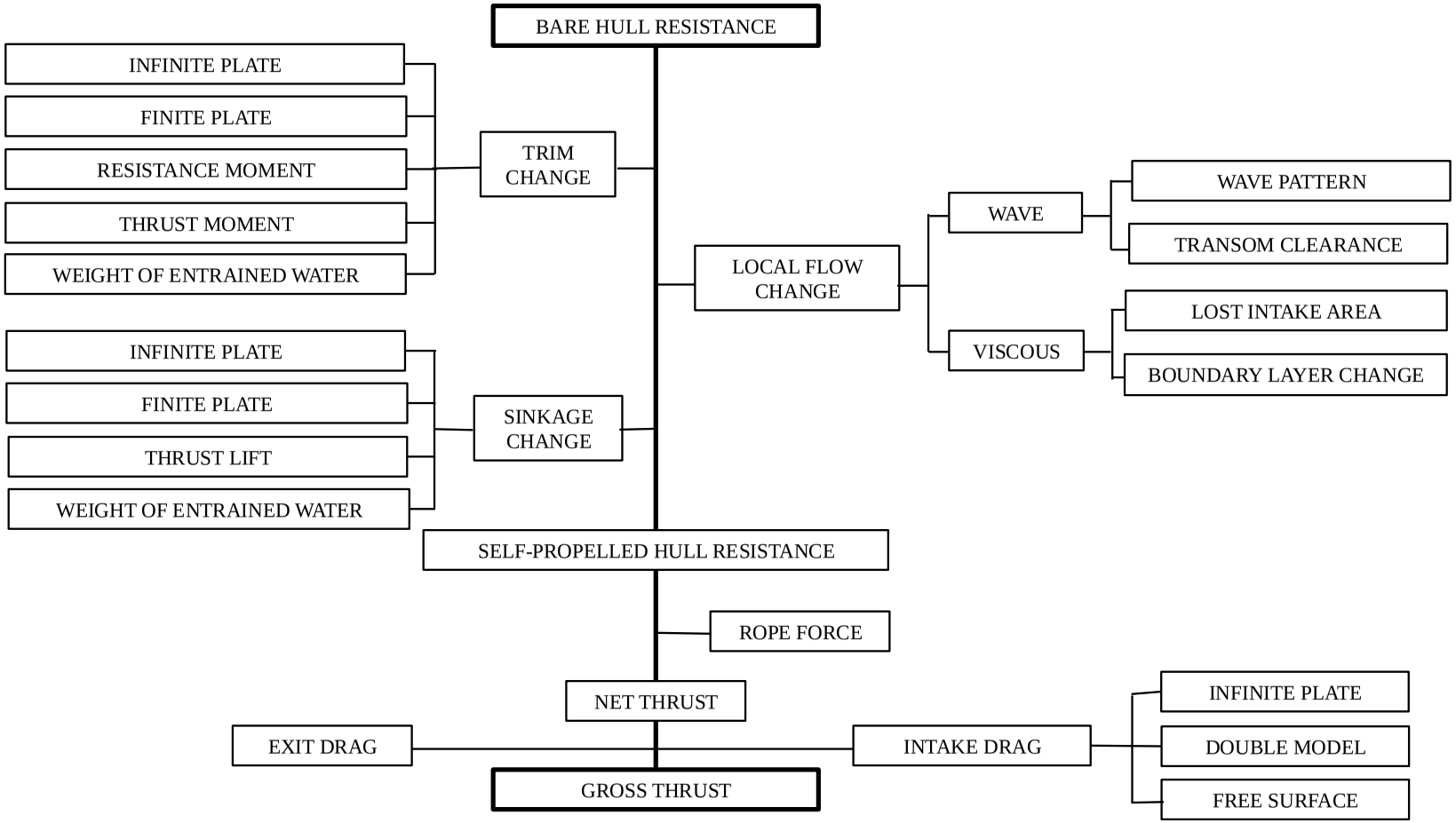

Figure 3.7 Contribution of different parameters on thrust deduction of a waterjet propelled craft

As seen in Figure 3.7 the difference between the bare hull resistance and the self-propelled hull resistance is caused by three independent parameters, the changes of sinkage, trim and flow around the intake. The combined effect of sinkage and trim can be called global flow pattern change and the contribution of the flow change around the intake can be referred to as local flow change. Assuming that sinkage, trim and the local flow changes independently influence the resistance change, the resistance increment of the hull may be estimated from a linear expansion in a Taylor series and expressed as follows (van Terwisga 1996),

$$\Delta R(Q,\sigma,\tau) = \frac{\partial R}{\partial \sigma}(Q_0,\sigma_0,\tau_0)d\sigma + \frac{\partial R}{\partial \tau}(Q_0,\sigma_0,\tau_0)d\tau + \frac{\partial R}{\partial Q}(Q_0,\sigma_0,\tau_0)dQ, \qquad (3\text{-}23)$$

where R is the hull resistance and Q, σ and τ are the flow rate through the ducting channel, the hull sinkage and the hull trim angle, respectively. Index 0 denotes the bare hull.

The bare hull equilibrium position is the reference point, about which the Taylor expansion is made. Obtaining the partial derivatives of resistance with respect to sinkage, trim and flow rate individually, the contribution of each of them to the resistance increment may be estimated.

As mentioned in Chapter 4, at full scale the self-propelled hull resistance is equal to the net thrust, but at model scale a towing force, called rope force, is applied to the self-propelled hull to account for the too large frictional resistance. The net thrust is thus reduced by this force, as appears from Figure 3.7.

To further explore the influence of various parameters the sinkage, trim and local flow effects have been subdivided into different components in Figure 5.1. The occurrence and magnitude of these effects depends on the definition of the bare hull condition. *In this investigation the bare hull case is defined as a case where the propulsor has no influence on the sinkage, trim and local flow*. Thus the hull is pushed (or towed) horizontally at the height of the centre of effort of the resistance. In this way, the true effects of the propulsor on the resistance may be investigated. It should be stressed that this condition is somewhat theoretical, since neither propeller driven nor waterjet driven hulls normally satisfy these conditions. The effects of deviations from this ideal case in the bare hull testing will be discussed below.

Perhaps the most basic influence on the global effects, sinkage and trim, comes from the change in pressure distribution on the hull due to the waterjet intake, and the most fundamental case that can reveal such an influence is that of an infinitely large horizontal flat plate with an intake. The effect is denoted “Infinite Plate” in Figure 5.1, and the case is referred to as “free-stream condition” in the following. (In this condition there is also a duct attached to the intake ejecting the jet horizontally).

A more realistic case is obtained if only part of the infinite plate is considered. The part of the plate, with an area and beam similar to the hull in question, may be considered separately from the rest of the infinite plate, which thus represents the water surface. From the same solution as above the forces and moments on the “hull plate” can then be obtained. In the flowchart this case is referred to as “Finite Plate”.

If the thrust is not horizontal, and applied at the same height as the resistance, a lift force and a trimming moment are created. The lift is denoted “Thrust Lift” in the flowchart. The moment is related to the centre of floatation and split into two components the “Resistance Moment” and the “Thrust moment”, as will be further explained below.

The ducting system of the waterjet obviously contains water, not present in the bare hull case. This water will generate a vertical force and a moment on the hull thus altering the sinkage and trim. In the figure this effect is termed “Weight of Entrained Water”.

It should be noted that if the bare hull is tested according to the ITTC recommendations, it is towed along the pump shaft axis, and the effect of the entrained water is taken into account by an additional weight at the stern of the hull. This is to approximately account for the inclined shaft and the entrained water already in the bare hull testing. Obviously the Thrust Lift, Thrust Moment and Resistance Moment for the self-propelled hull will then be much smaller, but they will not disappear entirely. Since the resistance of the self-propelled hull differs from that of the bare hull, there will be some contribution to all three. This contribution may be called a second order quantity and its magnitude is t_r times the first order quantity, i.e. it is one order of magnitude smaller than the first order quantity.

Due to the installation of the ducting channel, as well as the ingestion of the flow into the waterjet unit, some differences in the flow field in the aft part of the hull may occur in comparison to the flow field around the bare hull. This is called the “Local Flow” change and may have some impact on the increment of the resistance of the self-propelled hull. One may split the effect of the local flow change into the change taking place in wave making resistance and that taking place in viscous resistance.

The suction of the waterjet system results in a different wave pattern next to the aft part of the hull. The free surface is sucked down, and this may have different implications if the surface has a wave crest or a wave trough at this location. This effect is indicated as “Wave Pattern” in the flow chart.

As will be seen in Section 9.1.1 the suction of the water jet has several effects on the critical Froude number, where the transom clears the water. These effects may be quite important for the thrust deduction, particularly in the Froude number range where the transom is dry for the bare hull, but not for the self-propelled one. Effects of this kind are denoted “Transom Clearance” in the flow chart.

There are also some changes in the viscous flow around the hull. One may relate these viscous flow changes partly to the missing area of the bare hull surface, at the intake opening and partly to the boundary layer change in the vicinity of the intake due to the suction.

In the lower part of Figure 3.7 the effects relating net thrust and gross thrust are displayed. One component is the “Exit Drag” which occurs whenever the jet exit is submerged, or partly submerged, into the flow behind the transom. This situation occurs at low speeds, either when the water does not clear the transom or when the protruding part of the nozzle hits the (steep) stern wave.

Intake Drag is related to the forces on the protruding part of the control volume used in the momentum balance for obtaining gross thrust (See Figure 3.2). As will be seen below, this effect is zero under free-stream conditions, but not for a real case. The deviations from the free-stream conditions are denoted “Double Model” and “Free Surface”, respectively.

Discussion of the Flowchart

In this section a more thorough discussion of the effects introduced in Section 3.9.1 will be presented. Wherever possible, formulas for estimating the effects will also be included. First the effects related to the global changes, sinkage and trim, will be discussed. Thereafter effects of the local flow changes will be dealt with.

Global Effects

Since similar effects influence sinkage and trim, they will be treated simultaneously in this section.

Infinite Plate (Free-Stream Conditions)

Figure 3.8 defines the control volumes used for this analysis. One of the control volumes, CV_3, includes the ducting channel and the other, CV_4, includes the rest of the flow. These control volumes share a common surface, which is the imaginary surface covering the intake opening. Accordingly, when writing the force balance for each of the control volumes, it should be kept in mind to set different directions for the force on this surface. Note that CV_4 is considered to be a hemisphere.

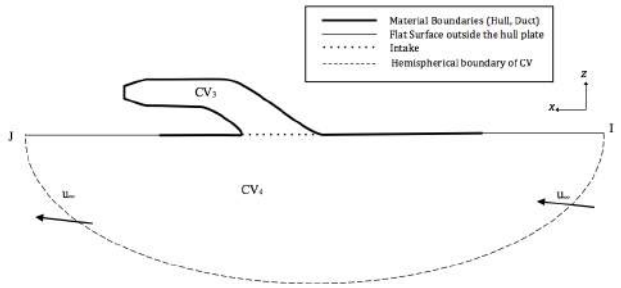

Figure 3.8 Control volumes used for derivation of intake induced lift on an infinitely large flat plate.

The control volumes, CV_3 and CV_4 are separately shown in Figure 3.9 and Figure 3.10, where, the forces exerted on the material boundaries of these control volumes are also indicated. The positioning of the forces in these figures is merely for demonstration and does not necessarily show the location where the forces are exerted in reality. These forces are defined as follows:

- F_D : vertical force (upwards) on the ducting channel.
- F_I : vertical force exerted on the imaginary surface covering the intake opening.
- F_S : vertical force (downward) on the infinite plate.
- F_H : vertical force (downward) on the finite part of the infinite plate (to be used later).

Writing the momentum flux balance for the control volume CV_4 in the vertical direction results in:

$$\phi_{I\,z} - \phi_{HS\,z} = +F_I + F_S, \qquad (3\text{-}24)$$

where $\phi_{I\,z}$ and , $\phi_{HS\,z}$ are the momentum fluxes in the z-direction through the intake and hemisphere surface of CV_4.

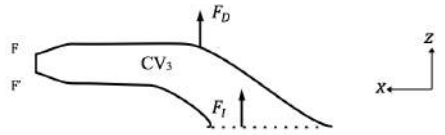

Figure 3.9 Control volumes, CV_3, and the vertical forces exerted on the boundary.

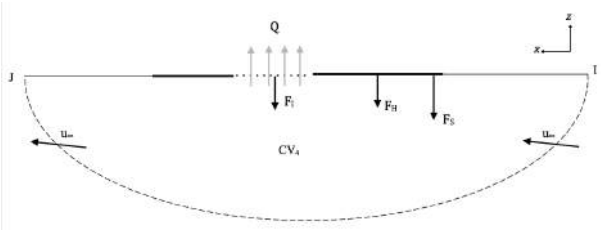

Figure 3.10 Control volumes, CV_4, and the vertical forces exerted thereon.

A more exact picture of CV_4 is shown in Figure 3.11. In this figure CV_4 is considered to be a hemisphere of a sufficiently large radius for the intake to be represented by a sink at its centre.

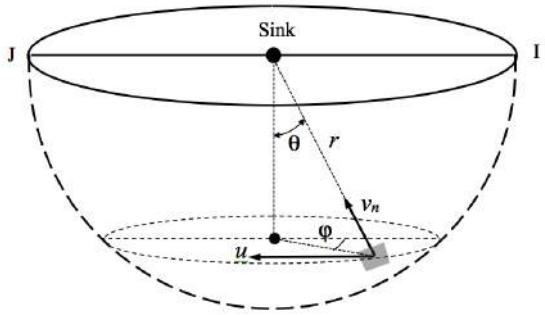

Figure 3.11 CV_4 and the intake represented by a sink at the center.

The normal velocity on the surface of the sphere induced by the sink is:

$$v_n = \frac{Q}{2\pi r^2}, \qquad (3\text{-}25)$$

where Q is the sink volume flux.

The vertical momentum flux through the surface of the hemisphere can be expressed as follows:

$$\begin{aligned}\phi_{HS\,z} &= \int_{-\frac{\pi}{2}}^{0}\int_{0}^{2\pi} \rho u_n u_z r^2 \sin\theta \, d\theta d\varphi \\ &= \int_{-\frac{\pi}{2}}^{0}\int_{0}^{2\pi} \rho[(v_n + u\sin\theta\cos\varphi)v_n\cos\theta]r^2\sin\theta\, d\theta d\varphi,\end{aligned} \qquad (3\text{-}26)$$

where angles θ and φ are shown in Figure 3.11. θ and φ vary from $-\frac{\pi}{2}$ to 0 and 0 to 2π, respectively. u_n and u_z are the normal and vertical component of the velocity through the large hemispherical surface and u is the undisturbed velocity.

Inserting v_n from Equation (3-25) into Equation (3-26) yields:

$$\begin{aligned}\phi_{HS\,z} &= \int_{-\frac{\pi}{2}}^{0}\int_{0}^{2\pi} \rho\left[\left(\frac{Q}{2\pi r^2} + u\sin\theta\cos\varphi\right)\frac{Q}{2\pi r^2}\cos\theta\right] r^2\sin\theta\, d\theta d\varphi \\ &= \int_{-\frac{\pi}{2}}^{0}\int_{0}^{2\pi} \rho\left(\left(\frac{Q}{2\pi r}\right)^2 \sin\theta\cos\theta + \frac{Q}{2\pi}u\sin^2\theta\cos\theta\cos\varphi\right) d\theta d\varphi.\end{aligned} \qquad (3\text{-}27)$$

When *r* tends to infinity the first term obviously tends to zero. This is the case also for the second term due to the factor including φ, which is integrated from 0 to 2π. Thus,

$$\lim_{r\to\infty} \phi_{HS\,z} = 0. \qquad (3\text{-}28)$$

Equation (3-24) thus simplifies to:

$$\phi_{I\,z} = +F_I + F_S. \qquad (3\text{-}29)$$

This equation implies that the vertical momentum flux through the intake is equal to the sum of all forces on the water from the entire horizontal plane, including the imaginary surface covering the intake opening.

Writing the same momentum balance for CV_3 gives the following equation:

$$\phi_{FF'\,z} - \phi_{I\,z} = -F_D - F_I. \qquad (3\text{-}30)$$

Since it is assumed that the jet is discharged horizontally, there is no component of the jet momentum flux in the vertical direction, $\phi_{FF'\,z} = 0$; so, Equation (3-30) may be simplified:

$$-\phi_{I\,z} = -F_D - F_I. \qquad (3\text{-}31)$$

Adding Equations (3-29) and (3-31), the combined result is:

$$F_S = F_D. \qquad (3\text{-}32)$$

The force downwards on the infinite plate is equal to the force upwards on the duct, i.e. there is no net force in the vertical direction in this case (Waterjet in free-stream conditions).

The next step is an investigation of the infinitely large flat plate trim angle caused by the intake-induced pressure. Generally, the trim angle of a hull, τ, can be obtained from the equation (Larsson & Eliasson 2007):

$$\tau = sin^{-1}\left(\frac{M_y}{\rho \nabla g \overline{GM}_L}\right) \times \frac{180}{\pi}, \quad (3\text{-}33)$$

where M_y is the trimming moment exerted on the hull, ρ is the water density, and ∇ is the displacement volume of the hull. $\overline{GM}_L$ is the longitudinal metacentric height of the hull.

For a sufficiently long hull, $\overline{GM}_L$is so large compared to the distance between the centers of buoyancy and gravity that it may be considered equal to the longitudinal metacentric radius, $BM_{L,}$, which may be obtained from:

$$BM_L = \frac{I_L}{\nabla}, \quad (3\text{-}34)$$

where I_L is the water plane area longitudinal moment of inertia.

Inserting Equation (3-34) into Equation (3-33) yields:

$$\tau = sin^{-1}\left(\frac{M_y}{\rho g I_L}\right) \times \frac{180}{\pi}, \quad (3\text{-}35)$$

Consider a flat plate of dimensions $L \times L$ (representing a hull) under which a constant positive pressure, $+p$, acts on one half (stern half) and a negative pressure, $-p$, on the other half (bow half). The moment, M_y, can be split into two components. A component due to the pressure on the large plate, M_{Py}, and a component due to the ducting channel moment, M_{Py}, which is bounded. The moment generated by the pressure around a line separating the two pressure distributions (around mid-ship) is:

$$M_{Py} = 2 \times p \times \frac{1}{2} L^2 \times \frac{L}{4} = \frac{pL^3}{4}. \quad (3\text{-}36)$$

The moment of inertia for the plate around the line in the middle (mid-ship) is:

$$I_L = L \times \frac{L^3}{12} = \frac{L^4}{12}. \quad (3\text{-}37)$$

Using Equation (3-33) the trim angle of the plate hull will be:

$$\tau = sin^{-1}\left(\frac{3\,p}{\rho g L} + \frac{12\,M_{Dy}}{\rho g L^4}\right) \times \frac{180}{\pi}. \quad (3\text{-}38)$$

M_{Dy} is bounded and in the limit of infinite L:

$$\lim_{L \to \infty} \tau = \lim_{L \to \infty} sin^{-1}\left(\frac{3\,p}{\rho g L} + \frac{12\,M_{Dy}}{\rho g L^4}\right) \times \frac{180}{\pi} = 0. \quad (3\text{-}39)$$

Since the trim angle for this generic case is zero for infinite L, this is certainly so for the more realistic pressure distribution, where the pressure is not constant, but decays with distance from mid-ship. Note that the limit is zero for any value of p, as long as it is finite.

Flat Plate of Limited Size

We will now proceed to investigate the lift force and moment induced by the action of an intake positioned on a flat plate of a limited size. This case is thus closer to reality than the previous one.

The intake-induced sinkage, σ_0, due to the forces exerted on the duct/hull system may now be obtained as:

$$\sigma_0 = \frac{F_D + F_H}{\rho g A_H}, \qquad (3\text{-}40)$$

where A_H is the water plane area of the hull.

The trim angle of the hull due to intake induced pressure and the duct force is (Larsson & Eliasson 2007):

$$\tau_0 = sin^{-1}\left(\frac{M_{D\,y} + M_{H\,y}}{mg\overline{GM}_L}\right) \times \frac{180}{\pi}, \qquad (3\text{-}41)$$

where $M_{D\,y}$ and $M_{H\,y}$ are the moments created by the ducting channel and hull, respectively, about a transverse axis. m is the hull mass. In order to estimate $M_{D\,y}$, it is assumed that the vertical force component of the ducting channel, F_D, is exerted at the same longitudinal position as the trailing edge of the intake opening, as shown in Figure 3.9.

In the examples of Section 5.1.1 we will assume that the flat plate representing the hull is rectangular, so the exact pivot point would be in the middle of the plate. However, to better represent reality, the pivot point is moved to the center of floatation of the real hull.

Thrust and Resistance Effects on Sinkage and Trim

Figure 3.12 shows a waterjet propulsion system with an inclined nozzle. The total angle of nozzle inclination relative to the horizontal direction, θ_T, is obtained by adding the hull trim angle, τ, to the nozzle design inclination angle, θ_n. The entire thrust of the waterjet unit is assumed to act in the same direction as the shaft, which has a same inclination as the nozzle. Thus, the change in sinkage of the hull due to the shaft inclination can be obtained as follows:

$$\sigma_T = \frac{T_Z}{\rho g A_H}, \qquad (3\text{-}42)$$

where T_Z is the vertical component of the total thrust force and A_H is the water plane area of the hull.

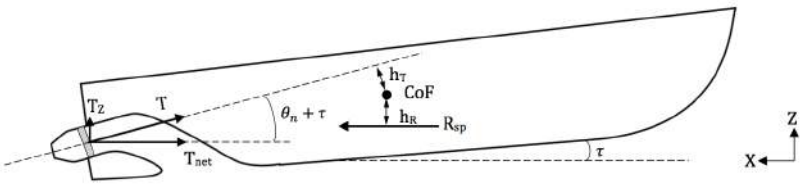

Figure 3.12 Illustration of Waterjet propelled hull with an inclined nozzle

There will be two trimming moments about the center of floatation due to the resistance and thrust forces. These moments can be calculated from the following equations:

$$M_{T\,y} = T \times h_T, \tag{3-43}$$

and,

$$M_{R\,y} = R_{sp} \times h_R, \tag{3-44}$$

where $M_{T\,y}$ and $M_{R\,y}$ are thrust, T, and resistance, R_{sp}, trimming moments, respectively. The distances h_T and h_R are the lever arms, which are depicted in Figure 3.12.

Trim angle of the self-propelled hull due to latter trimming moments can be calculated as follows:

$$\tau_T = sin^{-1}\left(\frac{M_{T\,y}}{mg\overline{GM}_L}\right) \times \frac{180}{\pi}, \tag{3-45}$$

and,

$$\tau_R = sin^{-1}\left(\frac{M_{R\,y}}{mg\overline{GM}_L}\right) \times \frac{180}{\pi}, \tag{3-46}$$

where τ_T and τ_R are trim angles due to thrust and resistance forces, respectively. m is the hull mass, g is the gravitational acceleration and $\overline{GM}_L$ is the longitudinal metacentric height of the hull.

According to these definitions, larger nozzle inclination causes the hull to rise and trim less (more bow-down). Thus, the effect of nozzle inclination on sinkage and trim of small boats, which may achieve large trim angles, may be beneficial. Large hulls, with smaller trim angles, often have no nozzle inclination in the original design of the waterjet unit.

Weight of the Entrained Water

According to the model test procedure proposed by the 24th ITTC Waterjet Specialist Committee (ITTC 2004a), the entrained water is represented by a load during the resistance test, to create a better correlation between the bare hull and self-propelled hull initial sinkage and trim. The load, which is used to compensate the weight of the entrained water in a static equilibrium condition, is equal to the weight of the water inside the ducting channel. The ducting channel volume which needs to be filled with water for the bare hull tests is shown in grey in Figure 3.13

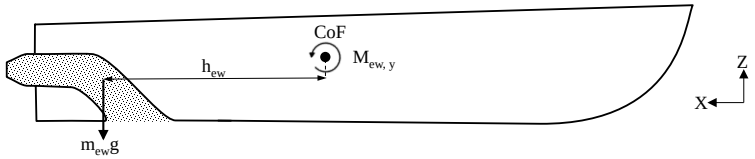

Figure 3.13 Illustration of the entrained water and its moment applied to the hull

The effect of the entrained water on the hull sinkage can be obtained through the following equation in which the subscript EW stands for entrained water:

$$\sigma_{EW} = \frac{m_{EW} g}{\rho g A_H} \qquad (3\text{-}47)$$

where m_{EW} is the weight of the total entrained water.

The trim angle can be calculated as:

$$\tau_{EW} = sin^{-1}\left(\frac{M_{EW\,y}}{mg\overline{GM}_L}\right) \times \frac{180}{\pi} \qquad (3\text{-}48)$$

where $M_{EW\,y}$ is the moment created by the weight of the water inside the ducting channel.

$$M_{EW\,y} = m_{EW} g h_{EW} \qquad (3\text{-}49)$$

h_{EW} is the horizontal distance between the centre of gravity of the total entrained water and the centre of floatation of the hull depicted in Figure 3.13.

Local Effects

In this section the intake induced effects on the local flow will be discussed.

Waves

Depending on whether a wave crest or a wave trough occurs next to the intake, the wave making resistance may decrease or increase, because the waterjet unit sucks down the nearby flow. If a wave crest occurs in the vicinity of the intake, it becomes flatter and, therefore, wave making resistance decreases. In contrast, if a wave trough occurs in this region, the intake sucks it down and the wave becomes steeper, which naturally increases the wave making resistance of the hull. For high-speed craft, it is more probable to have the wave trough than wave crest in the aft part, which leads to the conclusion that the waterjet system normally increases the wave making resistance of the hull. An example is presented in Figure 3.14 showing a wave cut just beside the hull for the Athena hull at a Froude number of 0.6, bare-hull and self-propelled. The hull is located between $x/Lpp = 0$ and $x/Lpp = 1$ in the plot, and it is clearly seen that the wave trough in the aft part is sucked down by the waterjet, which increases resistance.

The other waterjet influence on the waves is the effect on the transom clearance. In Section 9.1.1 it is shown that the transom clearance of the waterjet-propelled hull occurs earlier than the transom clearance of the towed hull. The reasons for the earlier transom clearance during the self-propulsion are also discussed in this section. The earlier transom clearance will influence the hull resistance from different aspects and the resultant of all these effect will cause the hull resistance to increase.

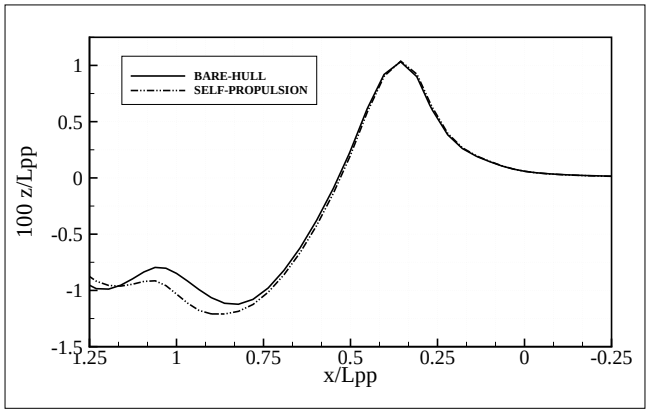

Figure 3.14 Wave cut profile comparison at $y/Lpp = 0.085$ for R/V ATHENA at *Fn*=0.6. The forward perpendicular is located at $x/Lpp = 0$ and the aft perpendicular is located at $x/Lpp = 1$ (The wave cuts are obtained from the simulations which are carried out employing the method explained in Chapter 4).

Viscous Resistance

Removing the intake-covering surface on the self-propelled hull obviously decreases the wetted surface, but it should be kept in mind that a new boundary layer starts to grow after the trailing edge of the intake, which may in fact increase the frictional resistance. The friction generally drops with distance along the surface in a boundary layer. See for instance the formula for a flat plate boundary layer, where the friction coefficient is inversely proportional to the fifth root of the local Reynolds number based on development length. If a "new" boundary layer is started aft of the intake, it will have a larger friction, than that which has developed all the way from the bow. Moreover, the negative pressure gradient and increased velocity will change the boundary layer development and increase the frictional resistance of the hull in front of the intake. The net effect of the boundary layer change is thus likely to be an increase in resistance.

4 Pressure Jump Method

Generally, the duty of a centrifugal pump is to increase the head of the flow. The rise of the flow head, which occurs by passing through the impeller, might be interpreted as an abrupt pressure rise at the section of impeller, which is generally called pressure jump. The occurred pressure jump is the fundamental theory behind the developed method for modelling the waterjet propulsion system and, therefore, this approach is called the Pressure Jump Method. The following sections describe the theory behind this method, its mathematical formulation and combination with a potential flow solver. The Pressure Jump method and the results obtained using this method are published in (Eslamdoost et al. 2013).

4.1 Formulation

To start with, the force balance for the waterjet-hull system must be formulated. The contribution of different parts of the system on the total resistance is depicted in Figure 4.1. In this figure, R_H is the hull resistance, R_D is the ducting channel drag and R_N is the drag force of the nozzle chamber. F_p is the force exerted by the impeller.

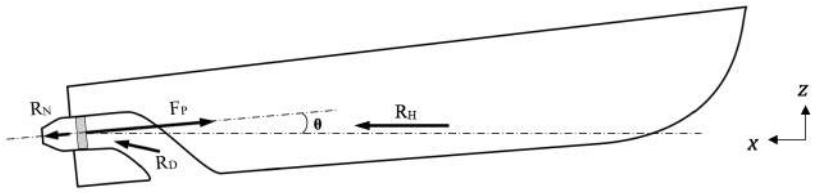

Figure 4.1 Force balance of the waterjet-hull system

Writing the force balance in the x-direction for the shown system, Figure 4.1, results in Equation (4-1).

$$F_{P,x} = R_H + R_{D,x} + R_{N,x} \qquad (4\text{-}1)$$

Because of the action of the pump, there is a difference in pressure between the sides of the impeller. In fact, this pressure jump at the impeller section is the main source of the created thrust force of the waterjet system. A simplified sketch of the nozzle geometry is shown in Figure 4.2. Assuming a constant pressure on each side of the impeller disk and considering

the fact that the impeller thrust force, F_p, is transmitted through its shaft which has an angle of θ with the horizontal plane, the equation for balancing the force in the *x*-direction reads:

$$F_{P,x} = (P_{after} - P_{front})A_{impeller} \cdot cos\,\theta \\ = \Delta p \cdot A_{impeller} \cdot cos\,\theta\,, \qquad (4\text{-}2)$$

where P_{front} and P_{after} are the pressures just before and after the impeller disk, respectively, and Δp shows the difference between these two. $A_{impeller}$ is the area of the impeller disk.

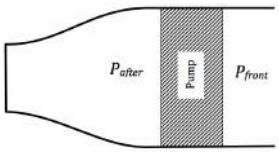

Figure 4.2 Schematic presentation of the nozzle section

Moreover, it is possible to denote the nozzle resistance, $R_{N,x}$, in the following integral form:

$$R_{N,x} = \iint_{S_{nozzle}} \sigma . n_x ds, \qquad (4\text{-}3)$$

where σ is the mean stress, S_{nozzle} is the internal surface of the nozzle chamber and n_x is the normal unit vector in *x*-direction.

One can split the stress tensor shown in Equation (4-3) into normal and shear stress:

$$\iint_{S_{nozzle}} \sigma . n_x ds = \iint_{S_{nozzle}} p . n_x ds + \iint_{S_{nozzle}} \tau . n_x ds, \qquad (4\text{-}4)$$

where *p* is the pressure and τ shows the shear stress tensor.

The actual flow inside the nozzle chamber may be considered as the superposition of two different cases. The first case is the flow through the nozzle chamber without any pressure jump but with the same flow rate as in reality. Adding a constant pressure rise to the first case results in the actual flow. According to the Navier-Stokes equations, in an incompressible flow, it is the pressure gradient which is important in defining the flow field and not the absolute pressure; hence, by subtracting the pressure jump, which is a constant amount inside the nozzle chamber, the velocity field inside the nozzle still remains the same as in reality.

Following this assumption, the pressure, *p*, The pressure after the impeller disk may be split into the static pressure inside the nozzle in the absence of the pump system, p_{WOP}, plus a constant pressure jump, Δp, occurring due to the action of the pump; thereby, one may rewrite the second term in Equation (4-4) as Equation (4-5).

$$\iint_{S_{nozzle}} p \cdot n_x ds = \iint_{S_{nozzle}} p_{WOP} \cdot n_x ds + \iint_{S_{nozzle}} \Delta p \cdot n_x ds. \qquad (4\text{-}5)$$

Since the velocity field inside the nozzle chamber does not change with the constant pressure jump, the shear stress tensor, τ, will remain the same in both cases.

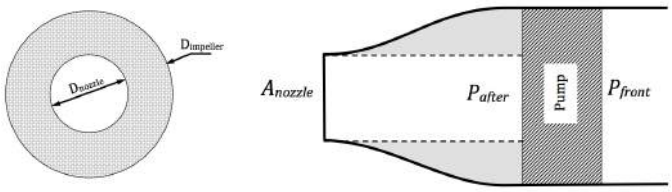

Figure 4.3 Schematic presentation of the nozzle section

The second term of Equation (4-5) can be simplified into Equation (4-6). As mentioned earlier, this term shows a constant pressure increase inside the nozzle chamber. Since Δp is constant, it can be moved out of the surface integral in Equation (4-5). The remaining term inside the integral is simply the projected area of the nozzle in the *x*-direction. This area is shown in grey in Figure 4.3.

$$\iint_{S_{nozzle}} \Delta p \cdot n_x ds = \Delta p\left(A_{Impeller} - A_{nozzle}\right) \cdot \cos\theta, \qquad (4\text{-}6)$$

where $A_{impeller}$ and A_{nozzle} consequently make up the impeller disk and nozzle discharge areas.

By introducing Equation (4-6) into Equation (4-5) and then inserting the resultant equation into Equation (4-3), a new expression for the resistance of the nozzle, $R_{N,x}$, is derived. By inserting this equation and Equation (4-2) into the original force balance equation (Equation (4-1)), the following equation emerges:

$$\Delta p \cdot A_{impeller} \cdot \cos\theta = R_H + R_{D,x} + \left[\Delta p\left(A_{impeller} - A_{nozzle}\right) \cdot \cos\theta + \iint_{S_{nozzle}} p_{WOP} \cdot n_x ds + \iint_{S_{nozzle}} \tau . n_x ds\right]. \qquad (4\text{-}7)$$

Simplifying this equation gives the following:

$$\Delta p \cdot A_{nozzle} \cdot \cos\theta = R_H + R_{D,x} + \left[\iint_{S_{nozzle}} p_{WOP} \cdot n_x ds + \iint_{S_{nozzle}} \tau . n_x ds\right]. \qquad (4\text{-}8)$$

The right hand side of Equation (4-8) is equal to the total resistance of the entire system without pressure jump and is named R_{TWOP}.

$$R_{TWOP} = R_H + R_{D,x} + \left[\iint_{A_{nozzle}} p_{WOP} \cdot n_x ds + \iint_{A_{nozzle}} \tau . n_x ds\right]. \qquad (4\text{-}9)$$

By introducing Equation (4-9) into Equation (4-8) the equation for obtaining the required pressure jump to balance the resistance forces reads,

$$\Delta p = \frac{R_{TWOP}}{A_{nozzle} \cdot \cos\theta}. \qquad (4\text{-}10)$$

4.2 Potential Flow Assumption

The following assumes that the flow from the capture area to the nozzle exit is inviscid and, therefore, there is no head loss inside the ducting channel. In other words, the total head at section 8 becomes equal to the total head at section 1 plus the constant pressure jump, Δp. This is expressed through Bernoulli's equation in Equation (4-11). The pressure at the nozzle outlet section is assumed to be atmospheric. Subscripts applied in Equation (4-11) are based on the notation presented in Figure 3.2;

$$\left[\bar{p}_1 + \rho g \bar{h}_1 + \frac{1}{2}\rho \overline{u_1^2}\right] + \Delta p = \bar{p}_{atm} + \rho g \bar{h}_8 + \frac{1}{2}\rho \overline{u_8^2}, \qquad (4\text{-}11)$$

where ρ is the water density and g is the gravitational acceleration. $\bar{p}_1$ and $\bar{p}_{atm}$ represent the average pressures at the capture area and atmospheric pressure, respectively. The average height of the capture area and nozzle outlet section are denoted by $\bar{h}_1$ and $\bar{h}_8$, respectively. $\bar{u}$ and $\bar{u}_8$ represent the average velocities at sections 1 and 8.

All terms in Equation (4-11) are known except the term containing the jet velocity, $\bar{u}_8$. By rearranging the equation for obtaining $\bar{u}_8$ and then dividing both sides by the undisturbed velocity, u_∞, the following equation emerges:

$$\frac{\bar{u}_8}{u_\infty} = \pm\sqrt{\frac{(\bar{p}_1 - \bar{p}_{atm})}{\frac{1}{2}\rho u_\infty^2} + \frac{\Delta p}{\frac{1}{2}\rho u_\infty^2} + \frac{2g(\bar{h}_1 - \bar{h}_8)}{u_\infty^2} + \frac{\overline{u_1^2}}{u_\infty^2}}, \qquad (4\text{-}12)$$

or alternatively,

$$\frac{\bar{u}_8}{u_\infty} = \pm\sqrt{\bar{C}_{p_1} + \Delta C_p + \frac{2}{Fn^2}\cdot\frac{(\bar{h}_1 - \bar{h}_8)}{L_{pp}} + \frac{\overline{u_1^2}}{u_\infty^2}}, \qquad (4\text{-}13)$$

where L_{pp} is the length between perpendiculars and Fn is the Froude number of the craft.

$$Fn = \frac{u_\infty}{\sqrt{g \cdot L_{pp}}} \qquad (4\text{-}14)$$

In the literature $\frac{\bar{u}_8}{u_\infty}$ is called the Nozzle Velocity Ratio, NVR, but since in the pressure jump method it is assumed that the pressure at the nozzle discharge section is atmospheric this velocity ratio can be called Jet velocity ratio, JVR, as well. According to the discussion in Section (3.6), if the nozzle discharge geometry is parallel NVR and JVR have the same value; but if the nozzle contracts at the jet discharge section, there will be an error in calculation of NVR, which can be solved by calculating the vena-contracta of the jet.

4.3 Numerical Simulation

The potential flow is computed using SHIPFLOW, a suite of computer codes based on in-house research. The XPAN module is a potential flow panel method, using Rankine sources on the hull and part of the free surface. A Neumann boundary condition for the potential is applied on the hull (corresponding to zero normal velocity) and a combined kinematic and dynamic condition is applied on the free surface at its exact location. The latter is obtained iteratively.

In the present study, the panels are extended into the duct all the way to the nozzle exit, where a velocity u_8 in the direction of the nozzle axis is specified. This is achieved by covering the exit plane with panels with the normal velocity u_8 at their control points. Figure 4.4 shows the upper part of the computational domain, the water below the free surface and outside the hull, as well as the duct back to the exit. The outer domain boundary is assumed to lie at an infinite distance. A potential flow solution can, thus, be obtained not only around the hull, but also inside the duct, with the given exit velocity, u_8. Note that the free jet is outside of the computational domain. In principle, this has no effect on the solution, but in practice, it makes it difficult for the free surface panels in the wake to satisfy the boundary condition; consequently, if the exit is close, instabilities may occur. So far, this has been resolved by moving the jet exit slightly forward.

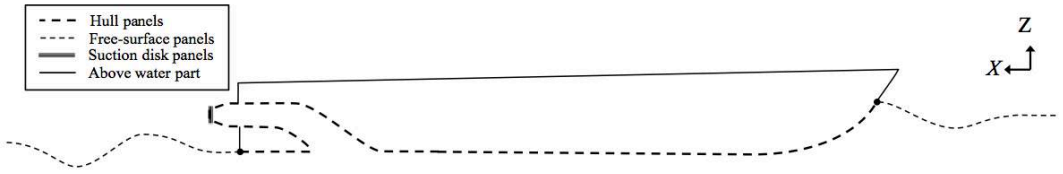

Figure 4.4 The computational domain is located below the dashed line, representing panelized surfaces.

The potential flow solution contains the pressure distribution around the hull and in the duct for the given u_8. This yields the wave resistance of the hull and an approximate pressure resistance of the duct. The latter is approximate, since SHIPFLOW assumes a constant total head in the entire computational domain, while in the duct the total head is in reality somewhat reduced, as discussed above. Since both the velocity (specified by u_8) and the height of the nozzle are correct, the pressure inside the duct will be over predicted which may result in some computational error.

The frictional resistance of the hull is computed by the boundary layer module XBOUND in SHIPFLOW based on the computed pressure. There is no need to include the RANS module for hulls like the ITTC proposed hull (ITTC 2002), with a wide submerged transom, in which the boundary layer stays relatively thin over the entire hull. Inside the duct, the friction coefficient is approximately computed by extrapolating it from the hull. As long as the wetted surface is correct, this is a minor approximation.

Note that no pump force is used in the SHIPFLOW solution. The key is to adjust the exit velocity u_8 such that Equations (4-10) and (4-13) are satisfied simultaneously. This has to be done iteratively. After each iteration, all terms on the right hand side of Equation (4-9)

are known, which means that R_{TWOP} can be computed and inserted into Equation (4-10) to obtain Δp. This is then inserted (non-dimensionalized) into Equation (4-13), where C_{p1} is obtained as the potential flow pressure on the hull at point A and u_1^2 is taken as the average of the squared velocity at the capture area, considering the boundary layer velocity profile computed by XBOUND. A new u_8 can then be obtained and the process repeated. It is convenient to start the process by neglecting the resistance of the duct.

To account for the trimming moment due to the water jet, the position (height) of the thrust force $\Delta p \cdot A_{nozzle}$ is specified at the centre of the impeller disk along the shaft line. SHIPFLOW then automatically trims the hull to balance the moment created by the total resistance force and the thrust.

4.3.1 Test Case

The hull investigated in this study is R/V ATHENA, the hull selected by the ITTC Specialist Committee on Waterjets (ITTC 2002). This Committee was composed of several Institutes that conducted some resistance and self-propulsion tests on ATHENA. Being a high-speed generic hull with a wide transom stern, having a substantial database of resistance, powering and flow information this hull satisfied several criteria taken into account by the Committee in choosing the proper hull. Some fundamental data are provided in Table 4.1. Moreover, Figure 4.5 depicts the body plan of the hull.

Table 4.1 Fundamental data for ATHENA (ITTC 2002)

Length	50.29 m
Maximum beam	6.68 m
LOW	46.9 m
Displacement	260 tons
Volume	257.5 m^3
b/B (Transom width ratio)	0.828

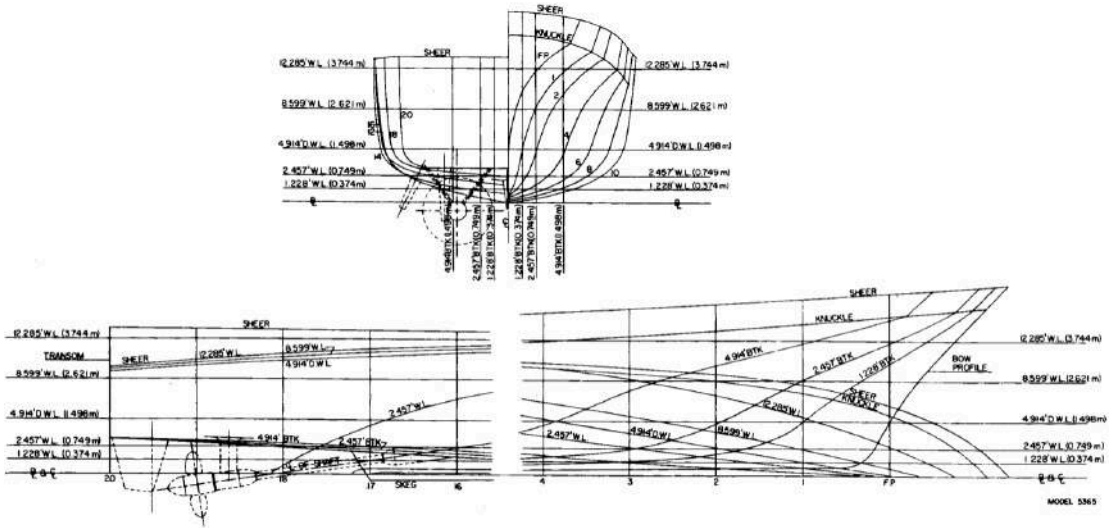

Figure 4.5 Profile lines and body plan for the R/V ATHENA (ITTC 2002)

A pair of axial flow waterjets was fitted into the model with a scale ratio of 8.556. The self-propulsion test set-up and a general view of the jet flow are shown in Figure 4.6 and Figure 4.7, respectively.

Figure 4.6 Model scale self-propulsion test setup (ITTC 2005c)

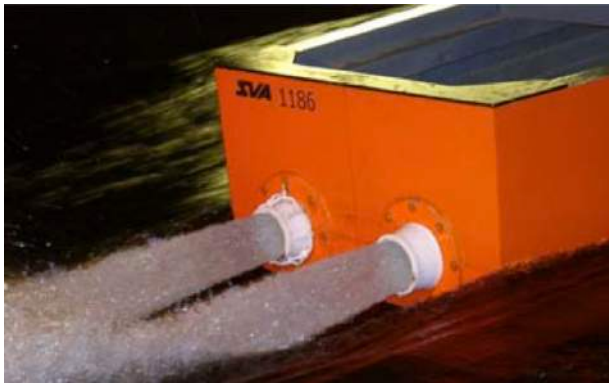

Figure 4.7 Model scale ATHENA with working waterjets (ITTC 2008)

There was a lack of agreement among different Institutes involved in the model testing on some issues like the hull displacement and the bare hull resistance test. Due to this controversy, the test displacement varied by 30 kg (Figure 4.8). The intention was to perform the bare hull resistance test with the covered intake openings; however, certain Institutes conducted the experiments with open intakes that made the ducting channel fill up with water (ITTC 2008).

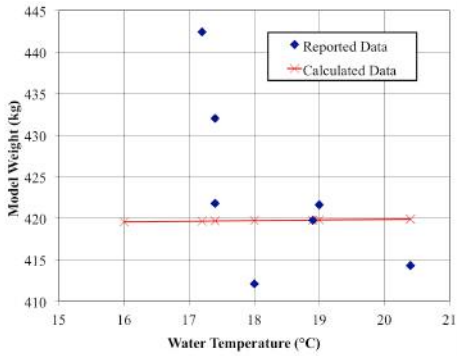

Figure 4.8 Model test displacement (ITTC 2008)

The bare hull resistance, bare hull and working inlet survey, jet velocity profile, momentum flux calculation and the full scale data prediction were investigated through a series of experiments (ITTC 2008), each of which is going to be discussed in the Validation section.

4.3.2 Panelization

In order to be able to create panels on the hull and the ducting channel, the whole system has been divided into multiple body groups and then assembled next to each other. Figure 4.9 depicts the general appearance of the panelization of the whole system. A closer look at the ducting channel panelization and the suction disk positioning is shown in Figure 4.10.

In the original geometry, the nozzle discharge is located outside the hull but as seen in Figure 4.9, the geometry has been modified and the jet discharge section is positioned somewhere before the transom inside the hull. As mentioned, this geometrical modification has been made to avoid the interaction of the suction disk with transom free surface panels. In the original geometry, when the suction disk is closer to the transom free surface, the pronounced source strength distribution on the suction disk and its interaction with the transom free

surface panels makes it hard to satisfy the dry transom condition which simply is the tangency of the transom free surface to the transom. Shortening the cylindrical part of the ducting channel is a solution for making the effect of this numerical interaction weaker. It should be noted that the angle of the nozzle discharge relative to the horizontal plane must not change in this geometrical modification.

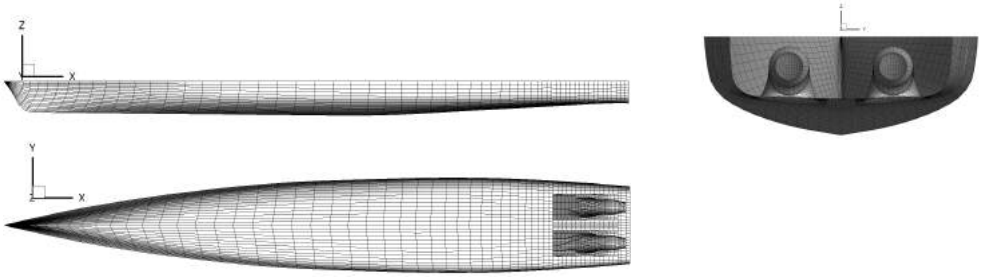

Figure 4.9 Panelization of the hull with intakes

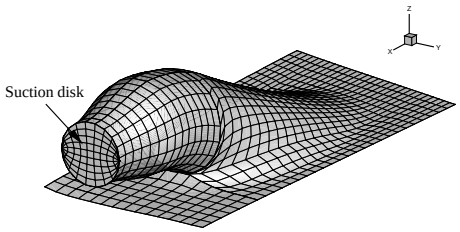

Figure 4.10 Panelization of the intake geometry and the suction disk

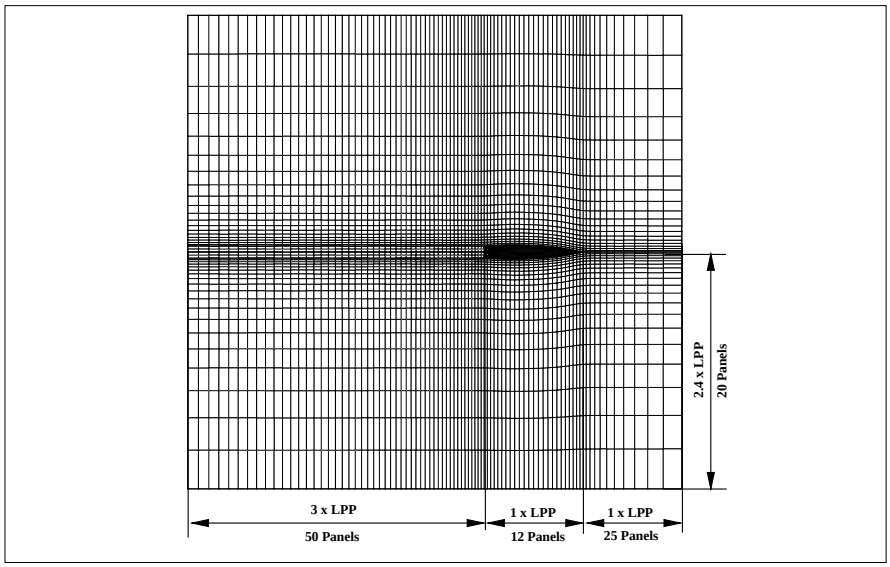

Figure 4.11 Panelization of the free-surface at $Fn = 0.6$

The computational domain size and free surface panelization for $Fn = 0.6$ are shown in Figure 4.11. The sufficient number of free surface panels along the hull is 20-30 panels per characteristic wavelength, n_λ (Janson 1997) This number is obtained by the following equation:

$$n_\lambda = \frac{1}{2\pi Fn^2}. \qquad (4\text{-}15)$$

As mentioned earlier, there is a strong interaction between the suction disk and the free surface panels at the transom, causing a problem to satisfy the dry transom criteria. As indicated before, this problem was partially solved by shortening the duct channel exit part. Moreover, coarser panels for the free surface at the transom must be used. Since the suction velocity applied on the disk varies with Froude number, the size of the first free-surface panel at the transom also varies.

4.3.3 Rope Force

Since the Reynolds number for model scale and full scale differs, the frictional resistance coefficient will also vary. In order to compensate for the deficit of the friction coefficient at full scale, an extra tow force is applied to the model in the self-propulsion test to unload the propulsor so that this propulsor only needs to overcome the full-scale frictional resistance. This extra force is called 'Rope Force' or 'Correction Allowance'.

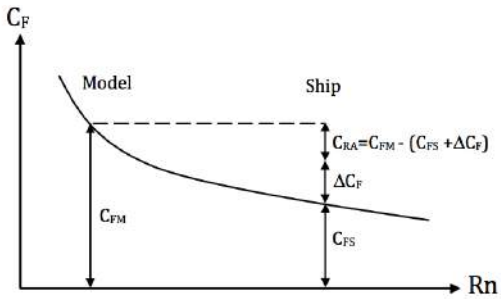

Figure 4.12 Illustration of the model-ship frictional resistance and the roughness allowance correlation

Figure 4.12 illustrates the friction coefficient variation from the model scale, C_{FM}, to the full scale, C_{FS}. The size of these coefficients can be obtained from the ITTC-57 proposed formula (Equation (4-16)) or other methods:

$$C_F = \frac{0.075}{(log_{10} Rn - 2)^2}. \qquad (4\text{-}16)$$

The total friction resistance coefficient of the full scale hull is equal to the friction coefficient at the full scale obtained from Equation (4-16) plus the roughness allowance, ΔC_F. Roughness allowance is an empirical surface roughness correction applied because of the larger surface roughness of the ship compared to the smooth surface of the model and is set to $\Delta C_F = 0.4\times10^{-3}$.

The non-dimensional rope force coefficient is expressed as follows,

$$C_{RA} = C_{FM} - (C_{FS} + \Delta C_F). \qquad (4\text{-}17)$$

Finally, the dimensional form of the rope force, which should be applied to the model, is obtained as follows,

$$R_A = \frac{1}{2}\rho_M U_M^2 S_M C_{RA}, \qquad (4\text{-}18)$$

where ρ_M is the water density of the model test, U_M is the model speed and S_M is the wetted surface area of the model.

4.3.4 Wave Making Resistance Correction

As mentioned earlier, in this study, the potential flow solver is employed to model the flow around the hull. This assumption results is an over prediction or under prediction of the hull resistance in different Froude number ranges. In the potential flow solver employed, XPAN, a dry transom condition is applied for all flow regimes, which means that the flow at the transom leaves the hull tangential to it (Figure 4.13). Although this is a reasonable assumption for the intermediate and higher Froude numbers, $Fn > 0.4$, for the lower Froude numbers, the transom is wetted and the dry transom condition is no longer valid. Whenever the transom is wet, a higher hydrostatic pressure is exerted on the stern compared to the dry transom, and accordingly, in a lower Froude number, e.g. $Fn = 0.3$, XPAN predicts larger resistance due to the dry transom condition applied. Moreover, at higher Froude numbers, $Fn > 0.6$, some highly non-linear effects in the inviscid flow, including flow spray, breaking or over turning waves, become increasingly important. These effects are not captured in the potential flow solver and, therefore, the resistance of the hull is under predicted in such Froude number ranges.

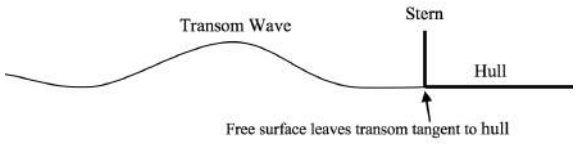

Figure 4.13 Dry transom condition

In order to predict the required powering more accurately, hull resistance must be predicted as precisely as possible. Hence, before employing the calculated hull resistance for balancing the resistance with the thrust of the propulsion system, the predicted resistance by XPAN must be corrected. The correction is accomplished through the formulas introduced by Höglund (2004) similar to those suggested by Harris and Schulze (1997). This method assumes that the computed skin friction is close to the values measured and that this correction is only applied to the wave making resistance of the hull obtained from pressure integration and the transverse wave cut method. The corrected wave-making resistance factor is shown in Equations (4-19):

$$C_{W-corrected} = (1 + K_{CW}) \cdot C_W, \qquad (4\text{-}19)$$

where C_W is the wave making resistance coefficient obtained from pressure integration on the hull. $C_{W\text{-}corrected}$ is the corrected wave-making resistance coefficient, which is corrected through the K_{CW} correction factor.

Höglund (2004) obtained the correction factors based on resistance measurements for the AMECRC systematic series hulls, which are semi-displacement hulls that operate between displacement and planning modes, i.e. $0.3 < Fn < 1.0$. These types of hulls are rather slender and characterized by flared bow sections. The immersed transom becomes dry when speed increases. Moreover, these hulls are known to offer better sea-keeping performance in rough seas than the hard chine planning boats. The AMECRC series consists of 14 models of transom stern, round bilge mono-hulls (Höglund 2004). Some characteristic data of the model geometries employed in the AMECRC series are shown in Appendix B.

Correction factor K_{CW} employed in Equations (4-19) was supposed to be functions of the hull speed *Fn*, the length-to-beam ratio *L/B*, the beam-to-draft ratio *B/T*, the block coefficient C_b and the hull displacement Δ which was used in the non-dimensional form of slenderness coefficient $L/\nabla^{\frac{1}{3}}$. Finally, K_{CW} was defined as Equations (4-20). Non-linear regression was carried out in order to find the constants, $a_1, \ldots, a_{25}$, with the result shown in Appendix B.

$$
\begin{aligned}
K_{CW} = & \left[a_1 + a_2 \cdot \frac{L}{B} + a_3 \cdot \frac{B}{T} + a_4 \cdot \frac{L}{\nabla^{\frac{1}{3}}} + a_5 \cdot C_b\right] \cdot Fn^0 \\
& + \left[a_6 + a_7 \cdot \frac{L}{B} + a_8 \cdot \frac{B}{T} + a_9 \cdot \frac{L}{\nabla^{\frac{1}{3}}} + a_{10} \cdot C_b\right] \cdot Fn^1 \\
& + \left[a_{11} + a_{12} \cdot \frac{L}{B} + a_{13} \cdot \frac{B}{T} + a_{14} \cdot \frac{L}{\nabla^{\frac{1}{3}}} + a_{15} \cdot C_b\right] \cdot Fn^2 \\
& + \left[a_{16} + a_{17} \cdot \frac{L}{B} + a_{18} \cdot \frac{B}{T} + a_{19} \cdot \frac{L}{\nabla^{\frac{1}{3}}} + a_{20} \cdot C_b\right] \cdot Fn^3 \\
& + \left[a_{21} + a_{22} \cdot \frac{L}{B} + a_{23} \cdot \frac{B}{T} + a_{24} \cdot \frac{L}{\nabla^{\frac{1}{3}}} + a_{25} \cdot C_b\right] \cdot Fn^4
\end{aligned}
\qquad \text{(4-20)}
$$

4.4 Validation of Pressure Jump Method

4.4.1 Experimental Measurements

The ITTC Specialist Committee on Waterjets (ITTC 2002)(ITTC 2005d)(ITTC 2008), completed an extensive study and a series of measurements on R/V ATHENA in order to investigate the waterjet/hull interaction phenomenon and defined a standard methodology for the performance of waterjet self-propulsion tests (ITTC 2005a). Multiple Institutes were involved in this study and each of them went through a similar procedure to conduct the resistance and self-propulsion tests. Subsequently, each Institute provided a separate data set containing the final measurements requested by the ITTC Specialist Group on Waterjets. Due to the confidentiality of the Institutes in charge of each data set, the measurements of each Institute were marked by a letter instead of the name of the Institute. The resistance test was accomplished for a Froude number in the range of $0.1 < Fn < 0.7$ but the self-propulsion test was carried out for only $Fn = 0.6$. The size of the towing tanks, in which the measurements were conducted, differed and resulted in 9% discrepancy in the resistance test results. The main source of this discrepancy was the blockage and/or shallow water effect in the smaller towing tanks. Accordingly, the final test results were split into those obtained from small tanks and those from the larger tanks. The data shown in the following bare hull measurements are from the larger towing tanks.

4.4.2 Results

Computational results obtained from the combination of potential flow simulation and the pressure jump method are presented in this section to validate the pressure jump method.

Figure 4.14 shows the predicted wave pattern around the self-propelled hull. The pressure distribution equivalent to the wave pattern shown is plotted in Figure 4.15. During the iterations required to obtain the correct pressure jump, Δp, and corresponding JVR, the pressure at the capture area, $\overline{C_{p\ 1}}$ must be recorded and used in the equation for Δp (Equation (4-10)). Figure 4.16 depicts the pressure distribution across the hull at the capture area section. In fact, $\overline{C_{p_1}}$ is the average of the pressure coefficient curve located inside the dashed rectangle. The pressure at the centre of the capture area is fairly close to the average pressure across the capture area. In practice, $\overline{C_{p\ 1}}$ may be replaced by $C_{p\ 1}$ in Equation (4-13).

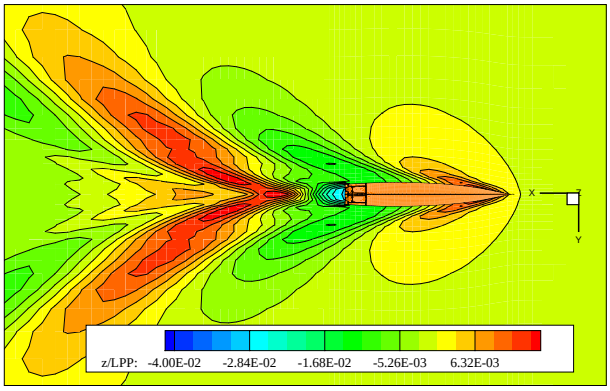

Figure 4.14 Computed Wave Pattern around the self-propelled hull at *Fn*=0.6

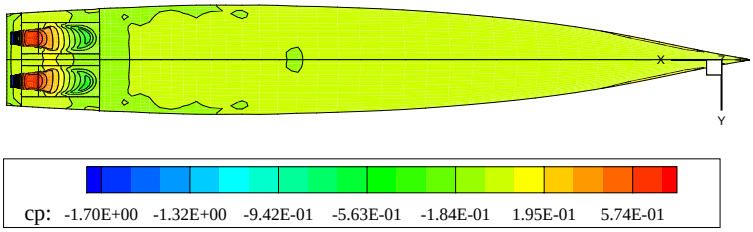

Figure 4.15 Computed Pressure distribution on the hull and ducting system at *Fn*=0.6

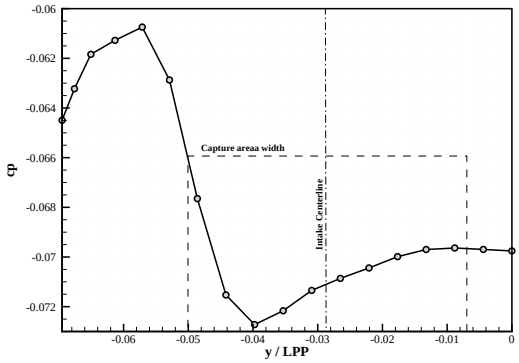

Figure 4.16 Computed Pressure distribution at the capture area section at *Fn*=0.6

A closer look at the pressure distribution inside the ducting channel is shown in Figure 4.17. Since there is no actual pressure jump in the potential flow simulation inside the ducting channel due to the action of the pump, the pressure at the nozzle discharge is negative, which is not the case in reality. In fact, the pressure jump is exactly large enough to yield zero pressure at the exit.

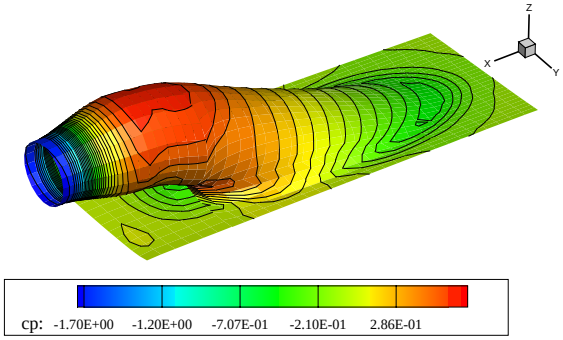

Figure 4.17 Computed Pressure distribution inside the ducting channel at *Fn*=0.6

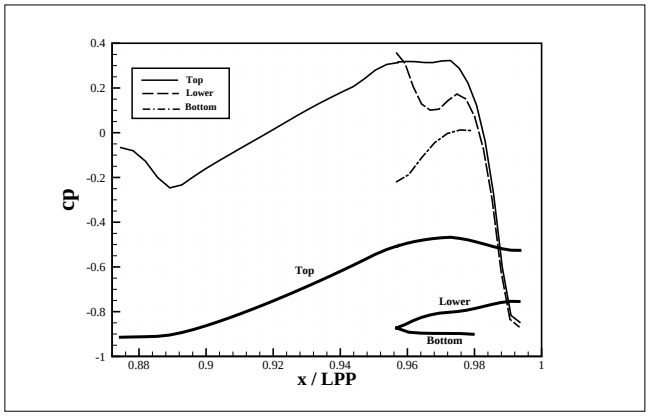

Figure 4.18 Computed Pressure distribution on the ducting channel mid section

Figure 4.18 shows the same information as given in Figure 4.17, but only at the mid-section of the ducting channel. Neglecting the low pressure inside the contracted part of the nozzle, which is not realistic here, the lowest pressure is observed somewhere close to the intake tangency point to the hull, and to some extent, the lower lip part. These are the regions where some cavitating flow may be observed. Moreover, the top part of the ducting channel, where the flow is forced to bend towards horizontal direction, has the highest pressure. These high-pressure and low-pressure zones may create a trimming moment, the direction of which depends not only on the size of these upward or downward forces, but also on the pivot point position. The pivot point for a hull is its centre of floatation (CoF). This effect will be further discussed in Chapter 5.

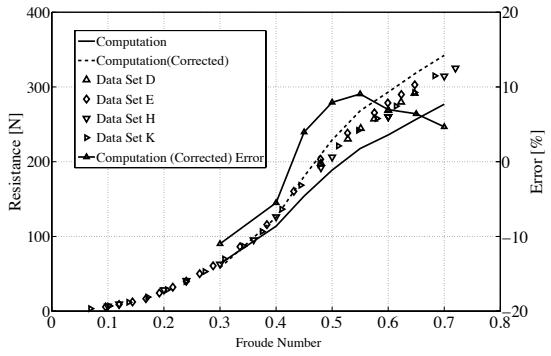

Figure 4.19 Resistance of the bare hull

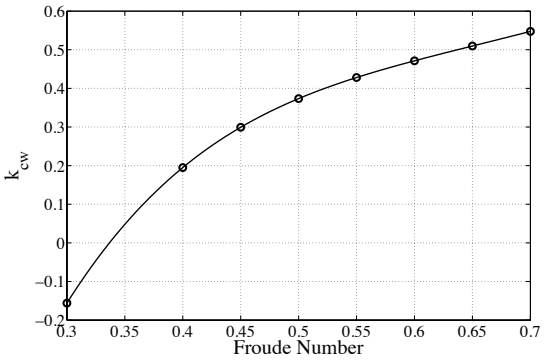

Figure 4.20 Wave making resistance correction factor for R/V ATHENA

Figure 4.19 depicts the predicted bare hull resistance and its comparison with the measurement. The original resistance curve from the potential flow simulation, the solid line, under predicts the actual resistance of the bare hull in the most of the Froude number range. Employing the originally calculated resistance causes some basic error, especially for the self-propelled hull, where the jet system flow rate is a function of the hull resistance. To solve the under prediction resistance problem, the wave making resistance of the hull is corrected based on the proposed method in section 4.3.4. The corrected resistance curve, plotted by the dashed line, shows a better correlation with the measurement. The same correction is applied to the resistance of the hull with intakes, as well. The corrected resistance is used for obtaining the pressure jump in Equation (4-10). In order to obtain the

error a polynomial curve is fitted to all the measured bare hull resistance data sets, and then the difference between this curve and the computed resistance is used for error calculation. For the entire computed Froude number range the computed resistance error varies between $\pm 10\%$ of the mean value of the measured resistance.

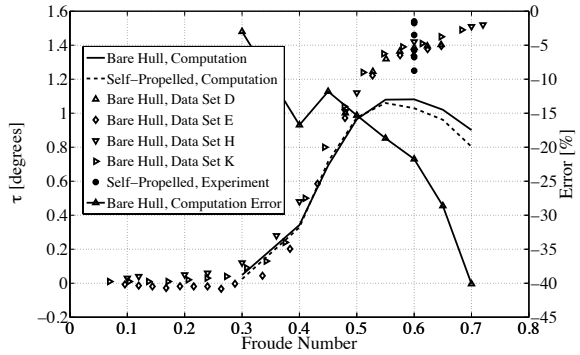

Figure 4.21 Trim angle versus Froude number

Figure 4.21 shows the variation of the trim angle for both the bare hull and the self-propelled hull against Froude number. No correction is available for the sinkage and trim. Comparing the computed bare hull trim angle with that obtained from the measurements, it is seen that there is a good correspondence up to a Froude number of 0.45. Thereafter the angle is under-predicted. The reason for this is most likely strongly non-linear effects like spray and wave breaking, which are not considered in the potential flow model. No error is given for the computed self-propelled hull trim angle because of the large scatter in the measured values.

Comparing the bare hull trim angle with the self-propulsion trim angle, they are the same for Froude numbers below 0.55. For higher Froude numbers, the trim angle of the self-propelled hull becomes slightly smaller than the bare hull trim angle. The reasoning behind the lower trim angle of the self-propelled hull must be related to the action of the waterjet system, which causes a bow down trimming moment. Various potential effects, which may contribute to the observed bow down trimming moment, are discussed in Section 3.9.

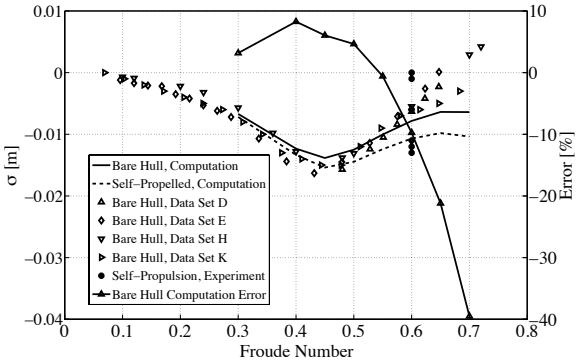

Figure 4.22 Sinkage at $\frac{1}{2}$ LPP versus Froude number

Figure 4.22 depicts the sinkage of the hull measured at half LPP and also the computed bare hull sinkage error. The vertical axis of the coordinate system is pointing upwards so the negative values for the sinkage means that the hull has moved downwards. Comparing the

bare hull sinkage with the measurement good agreement is seen for Froude numbers below 0.6. Since the sinkage changes sign, the relative error will be infinite at the zero-crossing; thus, the computed error is obtained as the difference between the computed and measured data divided by the data range, i.e. the difference between the largest and smallest measured values. This error varies around 10% for Froude numbers below 0.6. At higher Froude numbers, the computed sinkage is under-predicted, which can be related to the limitations of potential flow methods in capturing the highly non-liner free-surface effects. Comparing the computed self-propulsion sinkage with the measurement is a bit tricky since the scatter for the measured values is large, which was also the case for the measured self-propulsion trim angle; thus, no error is given for the computed waterjet driven hull sinkage.

Computed sinkage for the bare and self-propelled hulls demonstrates that the hull with the waterjets sinks more deeply compared to the bare hull. The increased sinkage of the hull in self-propulsion may be analysed in connection with the waterjet induced pressure and possible lift force of the ducting channel. A more detailed discussion on this topic is presented in Section 3.9

An interesting point, which may be noticed from the comparison of Figure 4.21 and Figure 4.22, is the Froude number that causes the bare hull and self-propelled hull sinkage and trim start to deviate from each other. This deviation starts at $Fn = 0.55$ for the trim angle, while the sinkage starts to deviate earlier at $Fn = 0.4$. The indicated fact needs to be investigated further for rendering the effect of sinkage and trim angle on the hull resistance increment.

According to the method proposed in section 4.3.3, an extra tow force is applied to the model in the self-propulsion computation. The purpose of this additional force is to compensate for the increased frictional resistance in the model scale. Figure 4.23 shows the force applied in different Froude numbers. The ITTC-57 friction coefficient formula has been used to calculate the friction coefficients for the model and the ship. Compared to the applied rope forces in the experiment, the employed rope force in the numerical simulation is smaller than most of those used in the experiment. There is a spread of 44.6% for the tow force selected in the experiment. This scatter seems quite large. Different water temperatures and roughness allowances may cause 15% difference in the rope force; however, this cannot explain the spread of the tow forces used.

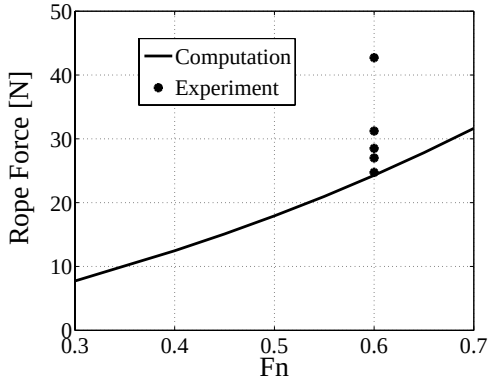

Figure 4.23 Rope force versus Froude number

The computed boundary layer profile at the centreline of the capture area is plotted in Figure 4.24. This figure shows that by increasing the Froude number, the boundary layer profile becomes slightly flatter. This may be in regard to the increasing Reynolds number or possibly according to the variation of the intake velocity.

Figure 4.25 demonstrates the boundary layer thickness and displacement (*Fn*=0.6) at the section of the hull, where the capture area is positioned. Assuming the semi-elliptical shape for the capture area, the outline of the capture area is sketched as well. Since the boundary layer thickness is almost constant in transverse direction across the capture area, a single boundary layer profile can be used for obtaining the ingested momentum and energy flux. The boundary layer profile at the centreline of the capture area is the most reasonable boundary layer profile to select.

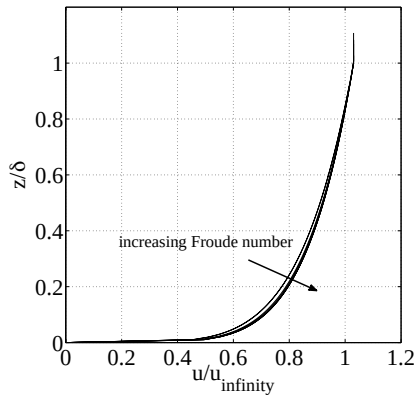

Figure 4.24 Boundary layer profile variation in different Froude numbers obtained at the centerline of the capture area.

According to Figure 4.25, at *Fn*=0.6, the height of the capture area is almost the same as the height of the boundary layer and the entire capture area may be assumed to be located inside the boundary layer. The height of the capture area decreases as the Froude number increases as seen in Figure 4.26.

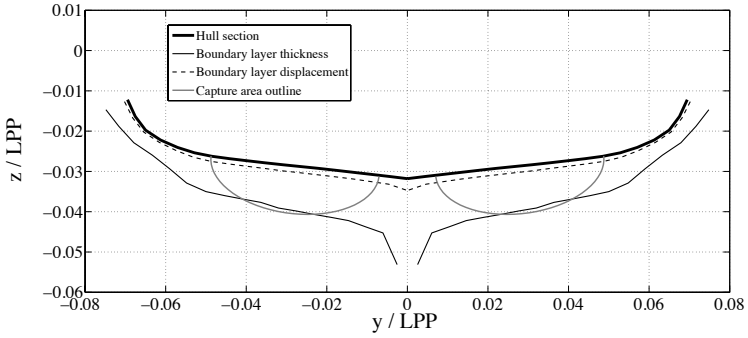

Figure 4.25 Illustration of the computed boundary layer thickness and displacement of a section across the hull at the capture area at *Fn*=0.6

Since the capture area is mainly located inside the boundary layer, it is fair to assume that the velocity in this area is directed along the hull surface. By integrating the non-dimensional boundary layer velocity profile over the capture area and averaging it, the Intake Velocity

Ratio (IVR), which may also be called wake fraction, is obtained. The variation of IVR versus the Froude number is plotted in Figure 4.27. Note the very large scatter in the experimental data.

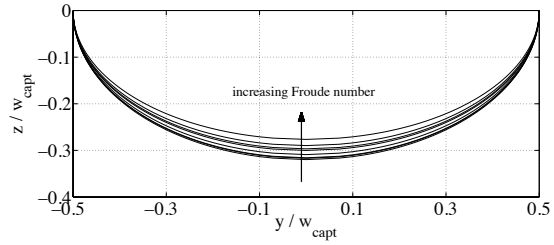

Figure 4.26 Semi-ellipsoid capture area geometry for different Froude numbers

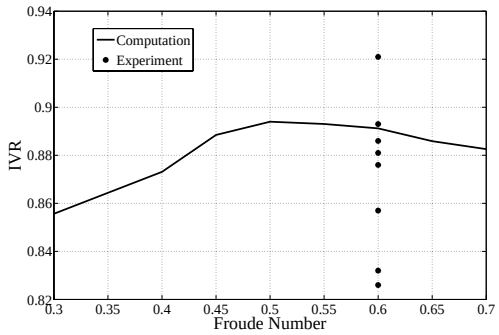

Figure 4.27 Non-dimensional mean velocity at the capture area (IVR)

The Nozzle Velocity Ratio (NVR) is provided in Figure 4.28. NVR shows the non-dimensional nozzle mean velocity. Due to the design of the nozzle discharge geometry for R/V ATHENA, the average pressure at the nozzle discharge is atmospheric and, therefore, there is no vena-contracta. In other words, NVR is equal to JVR (Jet Velocity Ratio). Although there is a hump in the NVR curve versus Froude number (Figure 4.28), the volume flow rate of the jet increases with Froude number (Figure 4.29). In both figures the predicted values fall within the bounds of the experimental scatter.

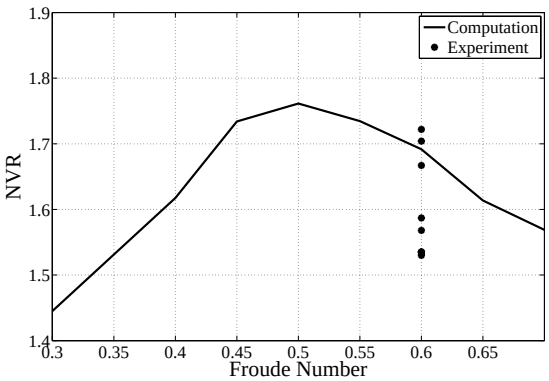

Figure 4.28 Non-dimensional nozzle mean velocity (NVR)

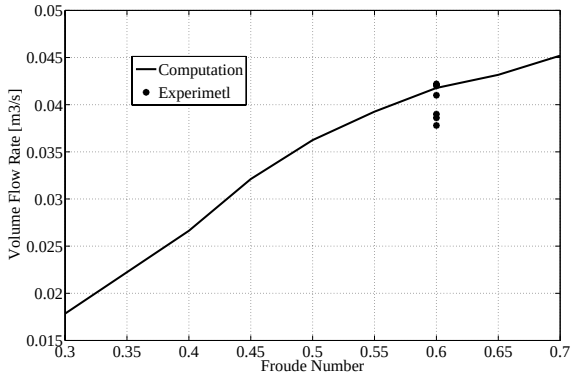

Figure 4.29 Volume flow rate through the ducting channel

The test results of the velocity profile in the nozzle discharge area show a considerable scatter, with the average bandwidth appearing to be 7%. It was reported that the longitudinal position of the measuring plane had a major effect on the velocity measured (ITTC 2005d).

Obtaining the correct values for IVR and JVR is important for calculating the gross thrust. To check the importance of a correct JVR a sensitivity study may be made:

Considering a uniform distribution for the intake and jet velocity, it is possible to simplify Equation (3-5), for obtaining the gross thrust as follows:

$$T_g = \rho u_\infty^2 \cdot NVR \cdot A_8 (NVR - IVR) \qquad (4\text{-}21)$$

According to Figure 4.27 and Figure 4.29, IVR and NVR at *Fn*=0.6 are:

$$IVR = 0.88, \quad JVR = 1.68$$

These IVR and NVR values will result in a certain gross thrust. If, for the same ship speed, IVR is assumed to be the same but NVR is reduced to 1.66 (about 1% less) the ratio of the gross thrust obtained from the new IVR and NVR and the old ones is as follows:

$$\frac{T_{g,2}}{T_{g,1}} = \frac{NVR_2 \cdot (NVR_2 - IVR_2)}{NVR_1 \cdot (NVR_1 - IVR_1)} = \frac{1.66(1.66 - 0.88)}{1.68(1.68 - 0.88)} \cong 0.96 \qquad (4\text{-}22)$$

This shows that a mere 1% under-prediction of the jet velocity results in 4% under-prediction of the gross thrust.

The computed bare hull resistance, net thrust and gross thrust (all corrected) are plotted in Figure 4.30 and compared with the measured gross thrust. Again, the computed gross thrust is within the experimental scatter. According to van Terwisga (1996), gross thrust and net thrust are very similar for most Froude numbers except for the hump region which is around *Fn*=0.6 for R/V ATHENA. However, this is not seen in the results of Figure 4.30. For $Fn < 0.43$ the gross thrust is smaller than the net thrust and for $0.43 < Fn$ it is vice versa. The maximum deviation is observed at *Fn*=0.6.

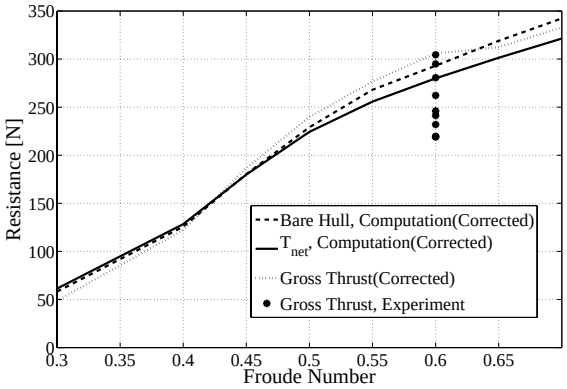

Figure 4.30 Bare hull resistance, net thrust and gross thrust variations

Figure 4.31 shows both total thrust deduction fraction *t* and resistance increment fraction, t_r (Equation (3-13)). Experimental data show the total thrust deduction fraction. Like in previous plots the corrected total thrust deduction fraction is within the experimental scatter. As mentioned earlier, corrected results show the curves obtained after applying the wave making resistance correction to the results of the potential flow solver. The measured thrust deduction fractions plotted in this figure is obtained from the measured model scale bare hull resistance and gross thrust. The corrected computed thrust deduction fraction shows a decent correspondence with the measured data.

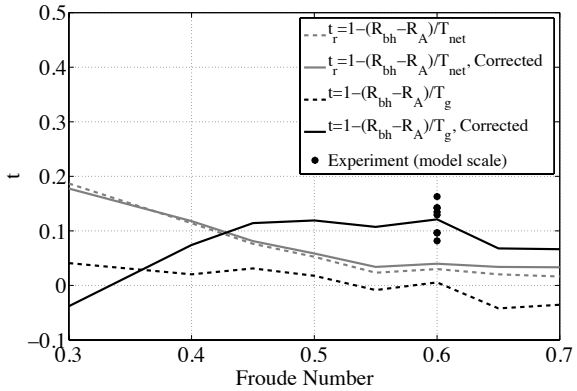

Figure 4.31 Thrust deduction fraction

5 Estimation of Waterjet/Hull Interaction Effects

In this section the various contributions to the sinkage and trim changes due to the waterjet action are estimated and compared to those obtained from numerical simulations or experiments. Thereafter, the resistance increment (Equation (3-23)) of the hull is obtained. It should be stressed that these computations are not intended to be quantitatively accurate; they are made to investigate the relative importance of the various factors in a qualitative way. The results and the discussions presented in this Chapter are also published in (Eslamdoost et al. 2014b).

5.1.1 Sinkage and Trim Estimation

The Finite Plates

In order to estimate the free-stream sinkage and trim, the induced lift force and moment due to the waterjet suction are obtained in a potential flow for a very large flat plate (approximating an infinitely large plate). A constant distribution of normal velocity on the simplified rectangular shape of the intake area is assumed. Two different flat plate hulls with different intake sizes are created as parts of the very large plate. The size of the flat plate hulls should approximate the size of R/V ATHENA and HAMILTON jet boat bottom surfaces. The characteristic data of R/V ATHENA and HAMILTON jet boat geometries are provided in Section 4.3.1 and Appendix D, respectively. These hulls are of different types with very different characteristics. A sketch of the flat plates and the intakes are provided in Figure 5.1 and Figure 5.2 and the related dimensions are specified in Table 5.1. The width of the plate is equal to the max beam of the waterline of the hull and the length is computed to give approximately the same water-plane area as the hull. This should give reasonable estimates of the sinkage, while the trim will be somewhat over-predicted due to the too small moment of inertia of the plate. Note that the ATHENA hull is at model scale, while the HAMILTON case is at full scale.

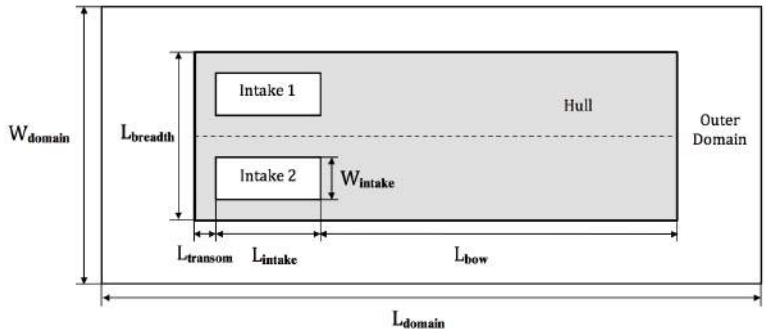

Figure 5.1 General sketch of the computational domain for the flat plate representing R/V ATHENA

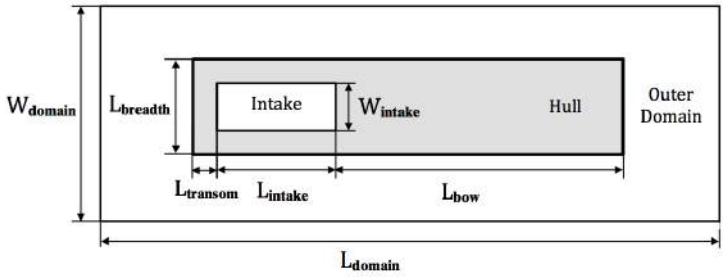

Figure 5.2 General sketch of the computational domain for the flat plate representing HAMILTON jet boat

Table 5.1 Characteristic dimensions of the flat domain employed to simplify the actual hull geometries

	L_{intake}	W_{intake}	L_{bow}	$L_{transom}$	$L_{breadth}$	L_{domain}	W_{domain}
R/V ATHENA	0.31	0.17	4.69	0.23	0.70	60	40
HAMILTON jet boat	0.70	0.35	4.80	0.19	2.20	60	40

* All lengths are in meters.

As a first step, the error of the numerical simulation due to non-infinite domain size should be investigated. According to the momentum balance over CV_4 shown in Figure 3.10, for an infinitely large domain, the momentum flux through the intake is equal to the force exerted on the flat plate including the intake area (Equation (3-29). But since there is no possibility to simulate an infinitely large domain in the numerical calculation, the size of the flat plate must be limited. Different sizes of outer domain were tested to investigate the effect of domain size on the satisfaction of Equation (3-29). Eventually, the computational domain length, L_{domain}, and width, W_{domain}, indicated in Table 5.1, were selected. The percentage of the lift force to momentum flux ratio in percent for each of the hulls is provided in Table 5.2. The deviation from 100% is due to the limited size of the domain and the numerical discretization. Since the deviation is very small the errors can be assumed negligible. It should be noted that the density of the panels close to the intake edges is very important for the calculated lift force, the reason being the large pressure gradients occurring close to the intake.

Table 5.2 The induced lift force ratio to the momentum flux through intake

	$(F_I + F_H + F_O)/\phi_I$ %
R/V ATHENA	98.57
HAMILTON jet boat	98.14

The panelization for the flat plate domains, including the intake, hull and outer domain as well as the obtained pressure distribution due to the suction, is presented in Figure 5.3 to Figure 5.8 for both cases. The total number of panels on the large flat surface are almost 18000 and 13000 and the intake velocity ratio, IVR_I, is set to be 0.23 and 0.21 for the R/V ATHENA and HAMILTON jet boat, respectively. These IVR_I ratios are appropriate for the self-propulsion point at $Fn \cong 0.6$ for both hulls.

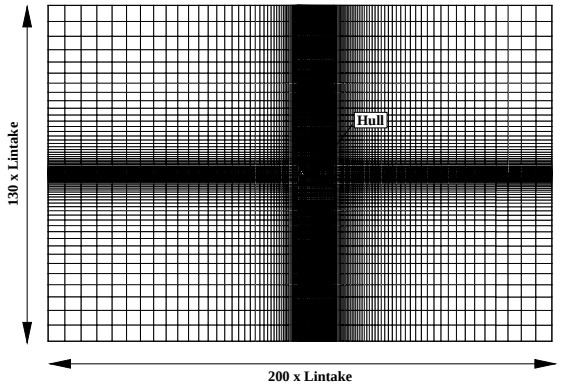

Figure 5.3 Panelization of the planar computational domain for R/V ATHENA

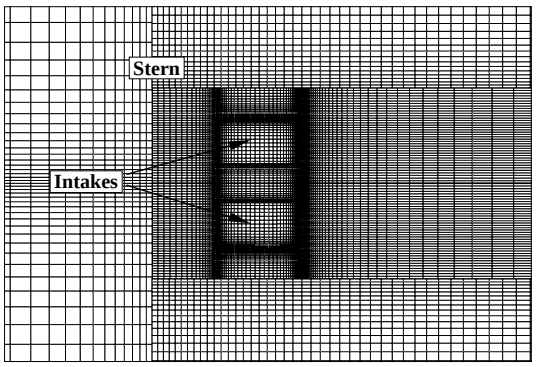

Figure 5.4 Closer look at the panelization of the flat hull of R/V ATHENA

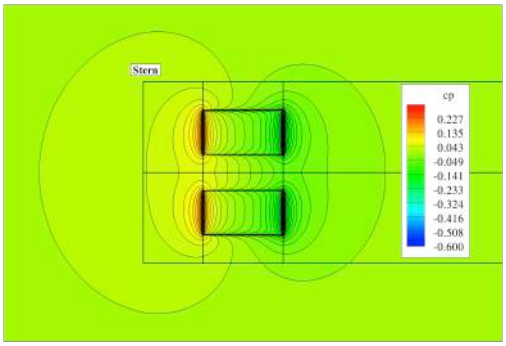

Figure 5.5 Pressure distribution on the flat plate representing R/V ATHENA

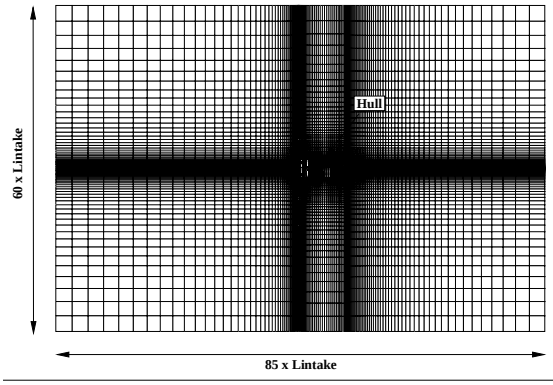

Figure 5.6 Panelization of the planar computational domain for the HAMILTON jet boat

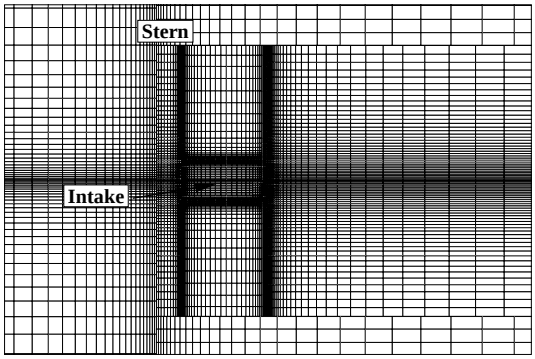

Figure 5.7 Closer look at the panelization of the flat hull of the HAMILTON jet boat

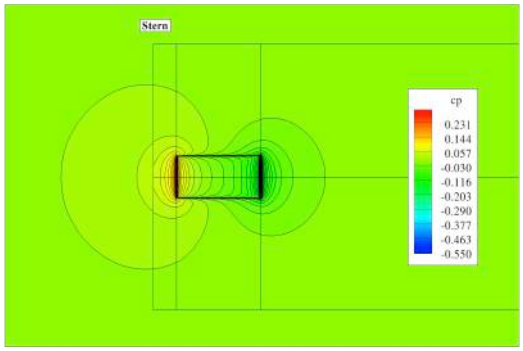

Figure 5.8 Pressure distribution on the flat plate representing the HAMILTON jet boat

In order to quantify the constant normal velocity assumption of the rectangular intake opening the normal velocity on the imaginary surface covering the waterjet intake opening is computed from the Pressure Jump Method simulation (see section 4.1) for R/V ATHENA, which the actual geometries of the hull and the intake channel are employed. The computed normal velocity is plotted on three different cross sections as shown in Figure 5.9. The horizontal axis is the non-dimensional longitudinal position along the intake opening cross sections starting from the section's leading edge, x_{LE}, close to the intake channel tangency point to the hull and extending to the trailing edge, x_{LE}, close to the lip. The cross sections' non-dimensional transverse positions referred to the centreline of the intake are defined as follows,

$$\delta y^* = \frac{y - y_c}{0.5\, W_{intake}}, \qquad (5\text{-}1)$$

where y and y_c are the transverse coordinates of the cross section and the intake opening centreline, respectively. The maximum width of the intake opening is denoted W_{intake}.

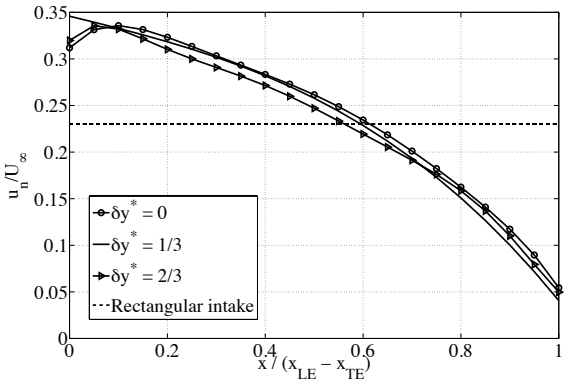

Figure 5.9 Normal velocity distribution on the imaginary surface covering the intake opening.

The mean value of the computed normal velocities over R/V ATHENA intake opening is almost equal to the constant normal velocity used on the rectangular intake opening but obviously the normal velocity on the rectangular intake is lower in the front part of the intake and higher in the back comparing to the computed normal velocity. This can eventually influence the pressure distribution on the flat plate but it should be noted that the entire model of the rectangular flat plate is a first approximation for the estimation of the waterjet induced sinkage and trim, which comes with several approximations and a constant normal velocity distribution over the rectangular intake opening is one of them.

The pressure coefficient is defined as,

$$cp = \frac{P - P_\infty}{\frac{1}{2}\rho U_\infty^2}, \qquad (5\text{-}2)$$

where P is the local pressure; P_∞ and U_∞ are the undisturbed pressure and velocity, respectively. In a potential flow the pressure coefficient simplifies to the following form,

$$cp = 1 - \frac{u^2}{U_\infty^2}, \qquad (5\text{-}3)$$

where u is the local velocity. This coefficient is plotted in Figure 5.5 and Figure 5.8 for both of the studied cases. As shown, the pressure in front of the intakes is lower than the undisturbed pressure while it is higher behind the intake. Depending on the size of the hull, some part of these low- and high-pressure zones may lie outside the hull, which has an effect on the lift force and moment on the hull. In the following section, the effect of different hull sizes on the lift force and moment exerted on the hull will be discussed.

Sinkage and Trim Estimation

Employing the procedure suggested in Section 3.9, there is a possibility to make rapid studies of the sinkage and trim caused by systematically varied hull and intake geometries. This is done here with the two example hulls as starting points. Basically, a single force representing the duct force is added to the force from the pressure distribution obtained from the flat plate simulation; the resultant force and moment is then calculated for varying hull sizes. The forepart, aft part and width of the hull are extended separately. For instance, if the aft part of the hull is extended, both the size of the forepart and width of the hull are kept the same as the standard hull size. There is no need to re-compute the pressure distribution on finite plates of different sizes. In order to calculate the force exerted on the finite plates the pressure distribution obtained from the very large flat plate computation is used but just over the finite plate area. The very large flat plate corresponds to the symmetry plane in the double model approximation. So, the integration of the pressure on the finite plate corresponds to the integration of the pressure on the hull and the part outside the finite plate corresponds to the free-surface in the double model case.

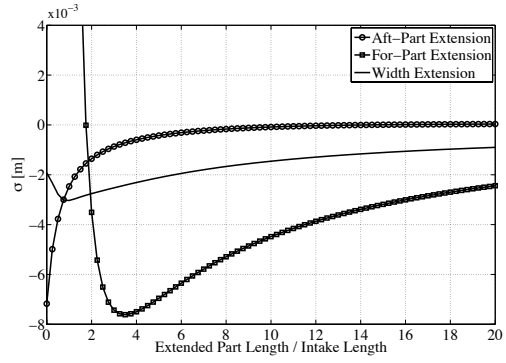

Figure 5.10 Sinkage variations by extending the flat plate in different directions (R/V ATHENA)

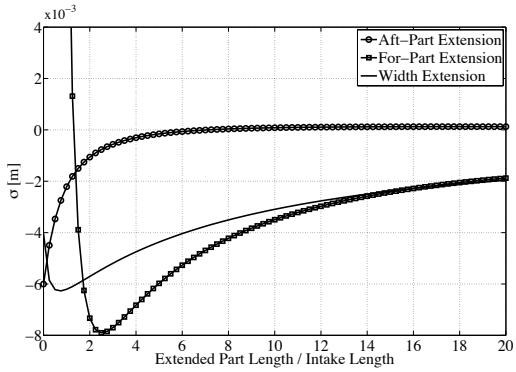

Figure 5.11 Sinkage variations by extending the flat plate in different directions (HAMILTON jet boat)

Figure 5.10 and Figure 5.11 demonstrate the sinkage variation of the hull in the free-stream condition by extending the flat plate in different directions for cases representing both the R/V ATHENA and the HAMILTON jet boat. Extending all directions causes the sinkage to converge to a certain value. The interesting point is that this certain value is almost zero for the extension of the aft part of the hull but not in the case of extending the other part of the hull. The reason is that almost all the waterjet intake induced pressure is located on the hull for the standard hull sizes except for some zones of high pressure located in the aft part of the hull (see Figure 5.5 and Figure 5.8). Extending the hull plate in any direction other than the aft part will not induce much upward lift while the low-pressure region ahead of the intake generates a lift force (pointing downwards), causing the hull to sink. Recovering the high pressure in the aft part of the hull by extending it may control the sinkage of the hull and may be taken into account in designing the vessel.

According to Section 3.9, there is no lift force for infinitely large flat plates in the free-stream condition, but the results obtained in Figure 5.10 and Figure 5.11, the conclusion for a flat plate of limited size may differ depending on the extent to which the hull covers the regions with distorted pressure due to the intake suction. For a flat plate of the size of a normal hull

and standard intake positioning, the lift force (pointing downwards) causes the hull to sink. The resultant sinkage is caused by the pressure distribution on the hull, in addition to the ducting channel force. Furthermore, there is one additional factor to be taken into account to estimate the absolute sinkage of the hull, the inclination of the nozzle that may result in an additional lift force, an effect that was introduced in Section 3.9.

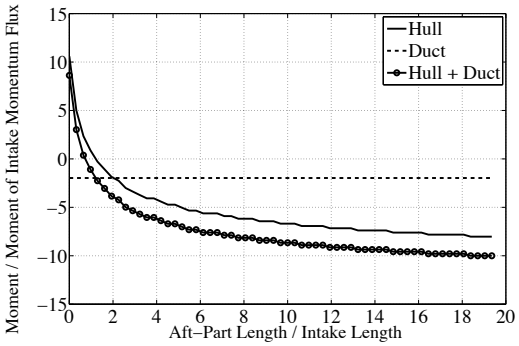

Figure 5.12 Contribution of different forces on the momentum exerted on the flat plate representing R/V ATHENA

Figure 5.12 shows the moment exerted on the hull by extending the aft part of the flat plate representing R/V ATHENA. An aft part length equalling zero means that there is no surface belonging to the hull after the intake trailing edge. Since the duct force for a certain intake velocity ratio (Equation (3-32)) is constant, the moment created by the duct force does not vary. The only varying moment is that created by the pressure distribution on the flat plate. Increasing the length of the aft part of the hull, a larger region with high pressure is located on the hull. This increases the bow down moment rapidly but after extending the hull for a certain length, the bow down moment does no longer increase and converges to a certain value caused by the fact that no distortion on the flat plate pressure can be detected far downstream of the intake.

Figure 5.13 and Figure 5.14 depict the trim angle variation of the flat plates representing R/V ATHENA and HAMILTON jet boat, respectively. Similar to sinkage plots, the horizontal axis shows the extension of the flat plate in a certain direction. Equation (3-41), in combination with computed moments exerted on the flat plate, is used to obtain these figures. For both plates, the extension of the hull in any of three directions results in a zero trim angle. This is in agreement with the proof in Section 3.9 that the trim is zero for free-stream conditions in deep water. The reason is that the extension of the hull beyond a certain region, where no noticeable distorted pressure exists, does not change the exerted moment on the hull (see Figure 5.12) but rather increases the metacentric height, which appears in the denominator of Equation (3-41) and causes the trim angle to converge to zero.

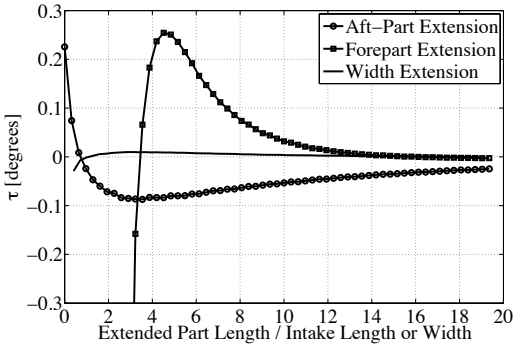

Figure 5.13 Trim angle variations by extending the flat plate in different directions (R/V ATHENA)

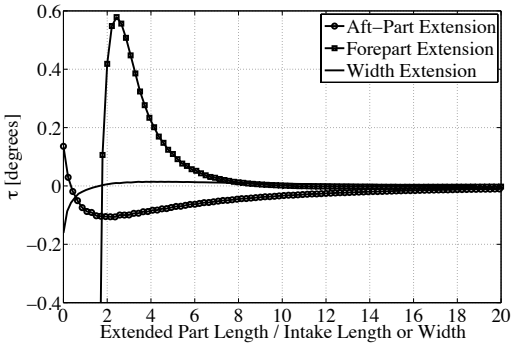

Figure 5.14 Trim angle variations by extending the flat plate in different directions (HAMILTON jet boat)

Comparing the curves demonstrating the extension of the forepart or aft-part of the flat plate, the trim angle does not seem to be sensitive to the extension of the flat plate width. The reason is that the pattern of the pressure distribution on the plate is almost symmetric to the symmetry axes of the intake (see Figure 5.5 and Figure 5.8). Increasing the plate width practically covers the same low-pressure as high-pressure regions, which balance each other so that no moment is exerted on the hull.

The extension of the forepart seems to greatly affect the hull trim angle in the beginning but rapidly dampens out. For the R/V ATHENA and HAMILTON jet boat, the standard ratio of the forepart length to the intake length is around 15 and 9, respectively. This means that a flat plate of standard size for a normal hull will not experience the extreme changes in the trim angle as shown in forepart extension curves in Figure 5.13 and Figure 5.14

After studying the effect of the hull size in free-stream condition on the sinkage and trim of the hull, the sinkage and trim for the flat plate in free-stream condition of the size closest to the R/V ATHENA and HAMILTON jet boat test cases have been obtained. Thereafter the other effects discussed in Section 3.9 have been computed, i.e. the effects of the thrust lift and moment, resistance moment and entrained water weight. Table 5.3 and Table 5.4 show the contribution of each of these parameters on the sinkage and trim change.

Additionally, the actual value from the computational simulation for R/V ATHENA and experimental data available for the HAMILTON jet boat are presented. These computed/measured values are indicated by ‘actual’ in the tables. The reason for not showing both computed and experimental total values for both hulls is that the measured data for ATHENA (from the ITTC measurements) are so scattered that it is even difficult to determine the sign of the effects, while the HAMILTON case could not be computed due to lack of some important data for the case. In principle the total sinkage and trim changes are obtained by considering all the contribution to the sinkage and trim changes shown in Table 5.3 and Table 5.4, if they have not already been taken into account in the bare hull case. The entrained water has already been considered both in the computation of the R/V ATHENA and the measurement of the HAMILTON jet boat, hence the contribution of the weight of the entrained water shall not be considered in the estimation of the total effects. However, all the other contributions in these tables need to be added before comparing with the ‘actual’ value.

Since the tests were carried out according to the ITTC procedure for both hulls, only the second order values of the Thrust Lift and Moment, Resistance Moment and Entrained water will influence the total value, i.e. only the changes in these parameters between the bare hull and self-propulsion will be of importance. As explained above, the first three are obtained by multiplying the first order values in the table by t_r. The magnitude of the fourth is not known due to lack of information on the computation of the entrained water effect in the measurements. If the volume above the still waterline at zero speed was included when computing the entrained water weight, there would be no change at self-propulsion and the effect would be zero in the table, but if this volume was not included there will be some effect.

Table 5.3 Contribution of different effects on sinkage change (first order quantities shown).

	$\Delta\sigma\ (\sigma_{sp} - \sigma_{bh})\ [mm]$		
	R/V ATHENA	**HAMILTON JET BOAT**	
Fn	0.60	0.62	0.98
Finite plate	-3.0	-4.3	-9.2
Thrust lift	+0.15	+6.6	+8.8
Entrained Water	-3.3	-4.7	-4.7
Actual	-2.9	-2.1	-22.8

Table 5.4 Contribution of different effects on trim angle change (first order quantities shown).

	$\Delta\tau\ (\tau_{sp} - \tau_{bh})\ [°]$		
	R/V ATHENA	**HAMILTON JET BOAT**	
Fn	0.60	0.62	0.98
Finite Plate	0.00	+0.01	+0.03
Thrust Moment	-0.01	-0.51	-0.67
Resistance Moment	-0.03	-0.21	-0.24
Entrained Water	-0.23	+0.33	+0.33
Actual	-0.02	-0.05	-0.47

As seen in Table 5.3 the flat plate sinkage for ATHENA corresponds very well with the computed total sinkage change. There is no contribution from the second order Thrust Lift, since the only inclination of the shaft is due to the small trim angle. Assuming that the total entrained water had been considered in the bare hull tests (so that the contribution in the table would be zero) it can be concluded that the sinkage is almost entirely due to the change in pressure distribution around the intake. With the same assumption for the Entrained Water all second order quantities are virtually zero. The Finite Plate indicates no trim change, and the actually computed value for the hull is also practically zero, -0.02 degrees. So, the hull does not trim since the change in the pressure distribution around the intake generates zero moment, as seen in the flat plate results.

For the HAMILTON hull there are two Froude numbers. In both cases there will be some effect of the second order quantities. The thrust deduction fraction t_r is not known at these Froude numbers, but the total thrust deduction t is around -0.05. Assuming that the influence of t_j is very small (as conjectured by van Terwisga (1996)), the real effects of the Thrust lift and Moment and the Resistance Moment are -5% of the first order values in the tables. Assuming again that the total volume of entrained water has been considered in the bare hull tests the sum of the effects for the sinkage at the low Froude number would be -4.0 mm,

while the measured on is -2.1 mm. The trim change would be very small, about -0.01 degrees, as compared with small the measured value –0.05 degrees. A similar conclusion for this case as for the ATHENA may be drawn for the trim: the pressure changes around the intake generate practically no trim at this Froude number. The over-prediction of the sinkage change by the flat plate may be due to the flat plate approximation. One must not overstress the results of this simple approach.

For a given Intake Velocity Ratio (IVR), the flat plate results should be proportional to the Froude number squared. Now, for HAMILTON, the IVR is slightly smaller for the higher Froude number, so the increase in sinkage between the Froude numbers is slightly smaller than quadratic: it increases from -4.3 mm to -9.2 mm. Adding the second order thrust lift, a sinkage change of -9.6 mm is obtained. This should be compared with a measured value of -22.8 mm. Like for ATHENA there is thus a factor 2 between the estimated and actual values, but here the estimated value is the smallest. The HAMILTON results are more cumbersome, since the sinkage increases 10 times between the Froude Numbers in the measurements, which indicates that the waterjet induced pressure is not the cause of the change. This requires further investigation. There is also a question mark for the trim. While the estimated value considering the second order effects is practically zero, -0.01, the actual value is quite large, -0.47°.

The sinkage and trim changes appear to be mainly due to the changes in pressure distribution around the intake, as approximated by the flat plate computations, for the ATHENA hull and the HAMILTON jet boat at the low Froude number. However, at the higher Froude number the measured changes cannot be explained in this way. Further investigations of this problem are needed.

5.1.2 Resistance Increment Estimation

As introduced in Section 3.9.1, the resistance increment of the hull is a function of three independent variables: the hull sinkage, trim and the flow rate through the waterjet system. Derivatives of the hull resistance with respect to each of these variables are given on the right hand side of Equation (3-23). In the following, the magnitude of the sinkage, trim and local flow change effect on the hull resistance increment will be estimated for R/V ATHENA. The estimated resistance increment is compared with the directly computed resistance increment. The direct method used for the computation of the resistance increment is the Pressure Jump Method introduced in section 4.1.

To start with, the self-propelled hull equilibrium position was set to the reference sinkage and trim obtained from the bare hull simulation. Thereafter, one of the parameters sinkage, trim or flow rate was varied while the other two were kept fixed as reference points. This procedure was accomplished for all three parameters. In order to make the sinkage and trim variations totally independent, the sinkage needs to be measured at the centre of floatation (CoF), where the hull does not change its displacement due to trimming. Going through this procedure provides three curves for resistance variations depending on variations of the sinkage, trim and flow rate. The curves obtained for R/V ATHENA are shown in Figure 5.15, Figure 5.17 and Figure 5.20, respectively. The effect of the flow rate variation on the

resistance change is studied by NVR variations. Note that the flow rate variation has to be taken around the self-propulsion flow rate, as the bare hull case (zero flow rate) would cause a very strange flow with an open intake. Since the variation of the parameters are accomplished for some discrete points, to obtain a smooth curve for the derivatives, one needs to obtain the curve which fits the discrete points and then obtain the derivative of the smooth curve. Figure 5.16, Figure 5.18 and Figure 5.20 demonstrate the derivative of resistance with respect to sinkage, trim and flow rate, respectively.

Obviously, increasing the hull sinkage increases the total resistance of the hull (see Figure 5.15) but this is not necessarily the case for the trim angle (see Figure 5.17). The trim angle variation reveals that there is an optimum trim angle for the hull and depending on the bare hull trim angle, as well as the bow down or bow up trimming moment (most probably bow down) created by the waterjet system, the hull resistance may increase or decrease in self-propulsion.

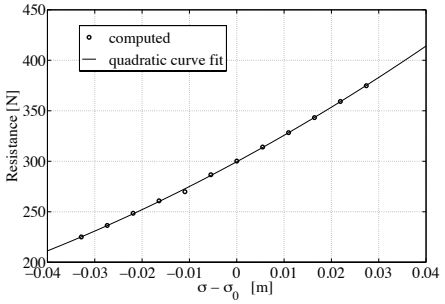

Figure 5.15 Resistance variations against sinkage variations for ATHENA at *Fn*=0.6.

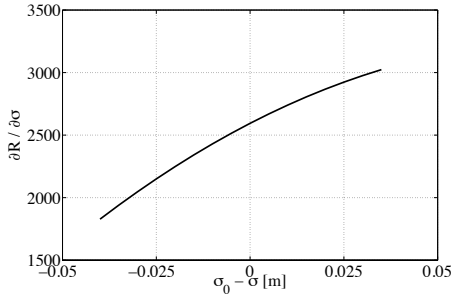

Figure 5.16 Resistance derivative with respect to sinkage for ATHENA at *Fn*=0.6.

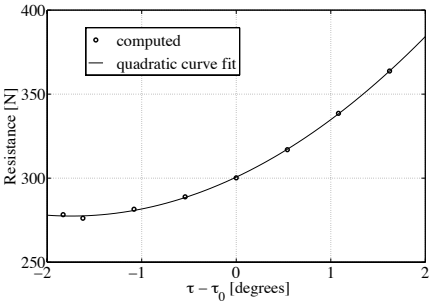

Figure 5.17 Resistance variations against trim angle variations for ATHENA at *Fn*=0.6.

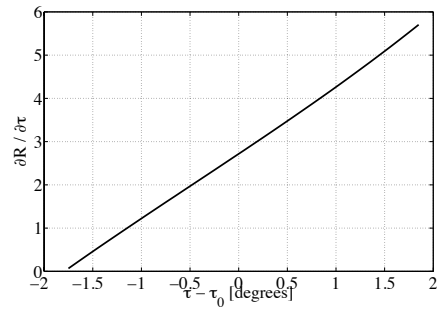

Figure 5.18 Resistance derivative with respect to trim angle for ATHENA at *Fn*=0.6.

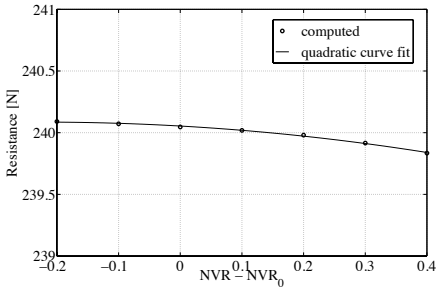

Figure 5.19 Resistance variations against NVR for ATHENA at *Fn*=0.6.

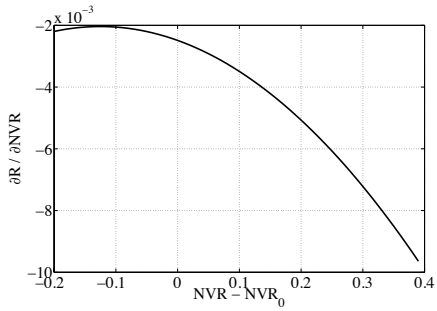

Figure 5.20 Derivative of the resistance with respect to NVR for ATHENA at *Fn*=0.6.

The optimum trim angle for a hull is closely related to the optimum transom area of that hull. As mentioned by Larsson and Raven (Larsson & Raven 2010), there is an optimum transom area for transom-stern hull types which increases with speed (Figure 5.21). The ratio A_{tr}/A_m given in Figure 5.21 is the ratio of the optimum transom area of the hull at rest, A_{tr}, to the maximum sectional area, A_m. According to the optimum values provided for the transom area in this figure, one may investigate whether the waterjet system trimming moment and sinking force helps to approach the optimum value or cause the transom area to move away from the optimum value. The last term of Equation (3-23) shows the impact of local flow change on the resistance increment. In order to obtain this term, it becomes necessary to fix the sinkage and trim angle of the self-propelled hull to those from the bare hull and set the flow rate to that obtained from the self-propulsion at a certain Froude number. Comparing the resistance change between the bare and self propelled hull with the fixed sinkage and trim angle reveals that for the self-propelled hull with a fixed sinkage and trim angle, the hull resistance is almost independent of the flow rate (see Figure 5.19 and Figure 5.20).

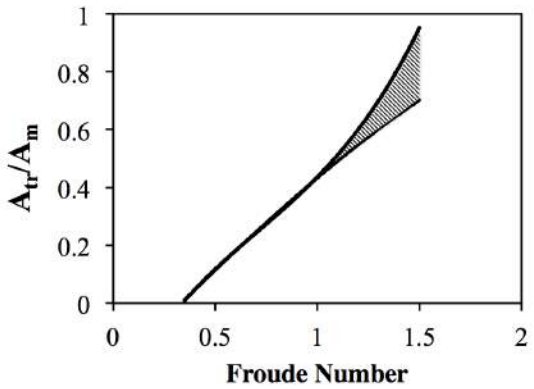

Figure 5.21 Optimum transom area vs. Froude number (extracted from (Larsson & Raven 2010))

Referring to Equation (3-23), the derivatives of the resistance with respect to sinkage and trim can be obtained from the curves provided in Figure 5.16 and Figure 5.18. For this purpose, the derivatives of resistance with respect to sinkage and trim can be taken from the curves provided in Figure 5.16 and Figure 5.18 at the point where the sinkage and trim of the self-propelled hull is the same as the bare hull. Then, multiplying these derivatives by the actual sinkage and trim change between the self-propelled hull and the bare hull (Figure 4.22 and Figure 4.21), the contribution of sinkage and trim to the resistance increment is obtained. The completed values of the resistance increment due to sinkage and trim for the R/V ATHENA hull at Fn=0.6 are given in Table 5.6.

As mentioned earlier, one can split the effect of the local flow change into wave making and viscous resistance. Table 5.6 shows the components of the local flow change, which contribute to the resistance increment. The wave making resistance is split into two components, where the first one is due to the change in wave pattern. This change is displayed in Figure 3.14, where it is seen that the wave trough is becoming deeper due to the suction. The second component is the effect on the transom clearance. Since the Froude number 0.6 for Athena is well above the critical value there is no effect of the difference in critical values between the bare hull and the self-propelled hull. There might be an effect of the interaction between the jet and the wave, but even this is unlikely at this relatively high

Froude number for ATHENA. The value for his component is likely to be negligible, but it is marked as not estimated.

Table 5.5 Resistance increment due to the sinkage and trim for R/V ATHENA at *Fn*=0.6

$\frac{\partial R}{\partial \sigma}(Q,0,0)d\sigma$	$\frac{\partial R}{\partial \tau}(Q,0,0)d\tau$
+7.8	-0.1

Table 5.6 Components of the local flow change which contribute to the resistance increment for R/V ATHENA at *Fn*=0.6

Local Flow ($\Delta R(Q,0,0)$): +1.6			
Wave making resistance: +9.3		Viscous resistance: -7.7	
Wave pattern: +9.3	Transom clearance: not estimated	Missing intake area: -7.2	Boundary layer change: not estimated

* All resistance components given in the table are in Newton.

The viscous resistance change due to the local flow change is obtained by comparing the viscous resistance of the hull with or without intake. The missing surface at the intake opening for the hull with the ducting channel, results in a smaller viscous resistance, and as can be seen in the table this reduction accounts for almost the entire viscous resistance drop. The contribution from the changed boundary layer should thus be very small. It has not been estimated in the present work, but this should be done in further work. In general, one may conclude that there is some minor change in the wave making resistance and viscous resistance of the hull caused by the local flow change. These components are of the same order but have different signs. Consequently, they almost cancel each other and the total effect of the local flow change on the resistance increment becomes very small.

As mentioned above, the last term of Equation (3-23) cannot be evaluated at the bare hull condition, so it is treated differently from the other two terms on the right hand side. Rather than using the resistance derivative times the increment in Q, the change is directly computed between the two conditions. Also, since the bare hull has no flow rate, Q_0 is set to zero. The actual realization of Equation (3-23), with the magnitudes of the different terms thus reads:

$$\Delta R_{estimation}(Q,\sigma,\tau) = \frac{\partial R}{\partial \sigma}(0,\sigma_0,\tau_0)d\sigma + \frac{\partial R}{\partial \tau}(0,\sigma_0,\tau_0)d\tau + (R(Q,\sigma_0,\tau_0) - R(0,\sigma_0,\tau_0))$$
$$= \quad +7.8 \qquad\qquad -0.1 \qquad\qquad +1.6 \qquad\qquad = \quad 9.3 \quad [N].$$

This is an estimation of the hull resistance increment and can be compared with the directly computed resistance increment from Pressure Jump Method (Chapter 4). The computed bare hull and self-propelled hull resistances are 293.0 and 304.2 N, respectively, so the resistance increase is 11.2 N, or about 4%.

Comparing the estimated resistance increment and the computed resistance increment via pressure jump method indicates that there is a decent correspondence of the estimated ΔR with the computed one. Since the estimation of the resistance increment is based on the independency of the hull sinkage, trim and local flow changes, the difference between the obtained resistance increments might be related to non-linear relations between the three mentioned effects, but it is more likely that the numerical accuracy of the value from the

direct simulation is too low. This small value is calculated by subtracting two large numbers, which reduces the numerical accuracy. But in general, the estimated resistance increment suggests that the assumption of linear relation of the hull sinkage, trim and local flow changes on the resistance increment seems reasonable. Therefore, the relative magnitudes should also be reasonable, and it may be concluded that the sinkage has by far the largest influence on the resistance for this case, followed by the influence of the local flow change.

5.1.3 Estimation of the Difference between Net Thrust and Gross Thrust

Since for R/V ATHENA it is assumed that the pressure at the nozzle exit is atmospheric, the exit drag is zero. This assumption might be violated in reality. There may also be a significant intake drag. A direct computation based on the definition (or possibly based on the different contributions) cannot be made using the main tools, which are presented so far in this thesis (i.e. potential flow and boundary layer methods), but it may well be done using a viscous flow method of the RANS type. This study is carried out in Chapter 9.

Since a direct computation cannot be made of the intake drag, an indirect estimation can be made by comparing the computed net and gross thrusts for ATHENA using the pressure jump method. For a Froude number of 0.6 the net thrust is 280 N, while the gross thrust is 306 N. The difference is thus 26 N, or 8.5% of the gross thrust. This is a surprisingly large number, which must be treated with caution. Again, we have a difference between two large numbers obtained in completely different ways.

6 Bare Hull RANS Method

This Chapter starts with a brief introduction of the numerical method employed for obtaining the bare hull resistance, followed by a description of the mesh and the verification and validation of the solution for one case.

6.1 Numerical Method

The numerical simulations were carried out with the code STAR-CCM+ 8.02. A Finite Volume method in combination with control volumes consisting of arbitrary polyhedrals is used in this code to solve the unsteady mass and momentum conservation equations in integral form. An implicit unsteady time stepping method is used. This method has a wide stability range (Courant number larger than 1) and therefore allows large local time step. The Volume of Fluid (VOF) method is used to obtain the volume fraction of the liquid, which adds one more equation to the system of equations. Convective terms in this equation are discretized using the HRIC-scheme (Muzaferija & Perić 1999). The free-surface interface is expected to be sharp since this scheme resolves the free-surface within typically one cell. The standard *k-ε* turbulence model is used to solve the turbulence effect on the mean flow. Hence, two more equations need to be solved, one for the kinetic energy, *k*, and one for the dissipation, *ε*. A wall function model for high y^+ values ($y^+ > 30$) is used and if the mesh is fine ($y^+ < 1$) the viscous sub-layer is properly resolved (Wolfstein 1969). This hybrid wall treatment technique is formulated to produce reasonable answers if the wall-cell centroid falls within the buffer region of the boundary layer ($5 < y^+ < 30$).

This system of equations is solved using a segregated iterative solution method based on the SIMPLE-algorithm. Details on discretization and solution methods can be found in (Ferziger & Perić 2003), (Demirdžić, I., Muzaferija 1995) and (Weiss, J., Maruszewski, J.P., Smith 1999).

Based on the different application purposes the bare hull simulations are carried out both with the fixed and free sinkage and trim. The results of the free hull are used in Chapter 7 where the transom clearance of the hull is studied and the results of the fixed hull are employed elsewhere when the thrust deduction of the hull is discussed. In order to compute the dynamic equilibrium position of the hull, the initial sinkage and trim of the hull are set to

the measured values. Before starting the 2DOF (free sinkage and trim) modeling the simulations are carried out with the fixed sinkage and trim until the pressure and viscous forces exerted on the hull are stabilized. Then the hull is released to heave and pitch and the 6DOF solver starts to update the equilibrium position of the hull iteratively.

When the hull is free to move in the simulations a towing force needs to be applied to the hull at the position where the hull was towed in the towing tank. The position of the tow force is shown in Figure 6.2. It was tried to keep the tow force parallel to the keel line during the resistance tests. In the computations, the magnitude of the tow force at each iteration needs to be set equal to the resistance of the hull computed from the previous iteration.

6.2 Hull Geometry

The hull used in this study is a planing hull designed by SSPA, with the model number 3209-B. In the rest of this thesis, this hull is referred to as the SSPA hull. A body plan is presented in Figure 6.1, and the longitudinal position of the hull sections are shown in Figure 6.2. The aft and fore perpendiculars are the sections which are marked by the numbers 0 and 20, respectively. The measurement of the draft is carried out at these sections. The towing point of the hull is 95 mm below the deck level and is located at section 6. The particulars of the hull are given in Table 6.1.

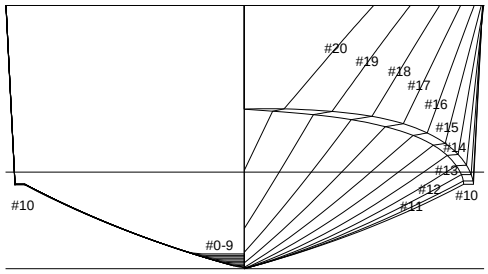

Figure 6.1: Body plan of the hull used in this study.

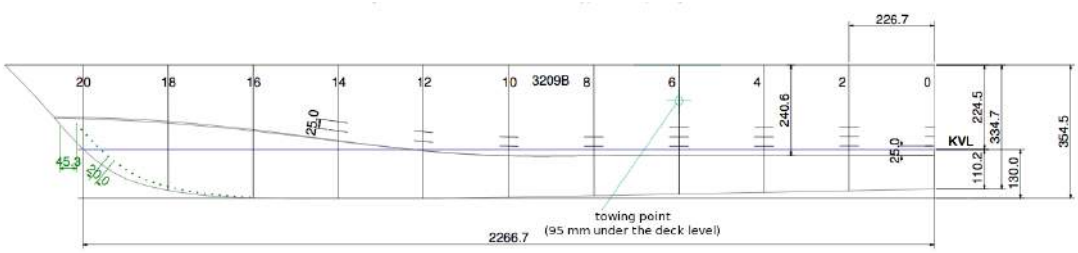

Figure 6.2: Longitudinal position of hull sections.

Table 6.1 Particulars of the hull

Scale factor α [-]	7.500		
Length L_{PP} [m]	17.00	Beam B [m]	4.65
Length L_{WL} [m]	16.98	Displacement [m^3]	35
Draft forward T_F [m]	0.98	Draft aft T_A [m]	0.98

6.3 Mesh Generation and Verification

Considering the symmetry of the flow only half of the geometry is modelled. Trimmed hexahedral grids and prism layers along walls are used to create the grids. Trimmed grids allow anisotropic local refinement around the hull and the free-surface. Four levels of refinement inside arbitrarily defined volumes are used for the free-surface and around the hull to capture the free-surface (Figure 6.3). Since the aim of this study is to investigate the transom flow, the finest refinement level is used in this region as shown in Figure 6.4. The boundary layer grid on the symmetry plane in the aft part of the hull is shown in Figure 6.5.

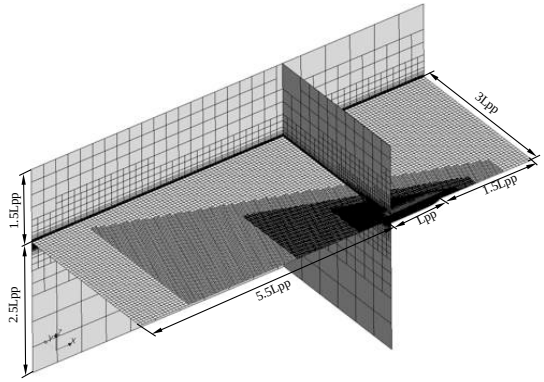

Figure 6.3: The structure of the mesh illustrating the refined zones. Arrows show the dimensions of the computational domain expressed in the hull Lpp.

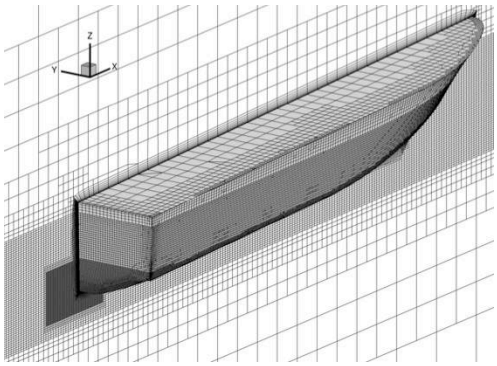

Figure 6.4: Closer look to the mesh on the hull and around it.

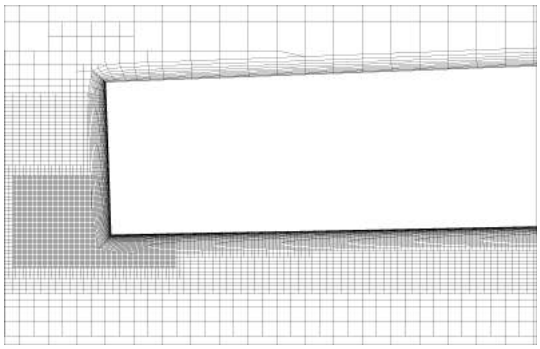

Figure 6.5 Grid on the symmetry plane in the aft part.

To obtain a suitable cell size, and hence total grid number, a systematic grid refinement study was carried out for the Froude number 0.488, which is a speed close to the bare hull transom clearance Froude number. Since the transom clearance phenomenon is on of the focus of the current thesis, this Froude number was selected for the grid independency study of the bare hull flow simulations. Eight grids with systematically varied grid parameters were used. The number of cells for the coarsest grid is $1.0E6$ and for the finest grid it is $14.1E6$. In Figure 6.6 the convergence of the C_T solution is shown. Since the grid is unstructured the step size h_i on the horizontal axis is obtained as the third root of the total number of cells for grid *i*. h_1 represents the finest grid.

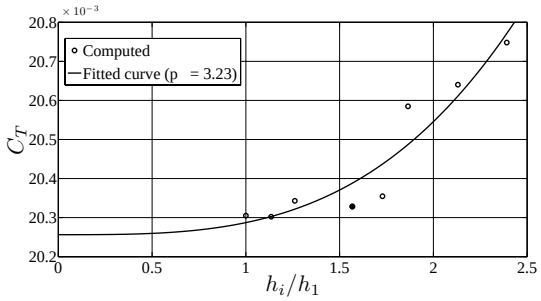

Figure 6.6 Convergence of the total resistance coefficient with grid refinement at $Fn = 0.488$. The full circle shows the grid employed to perform the calculation for the entire range of Froude numbers. The p-value is the power of the best fit expression for the error according to Eça and Hoekstra (2014).

A formal verification based on the Least Squares Root method by Eça and Hoekstra (2014) was also carried out. This showed that a good compromise between numerical accuracy and computational effort was obtained with grid number 4 (full circle in the figure), which was selected for further computations. The number of cells for this grid is $3.7E6$. The numerical uncertainty for this grid was 2.3%. It should be noted that the verification method is for steady flows, while some unsteadiness was detected in the present computations, particularly at Froude numbers below the critical one. A certain dependence on the time step may thus be expected.

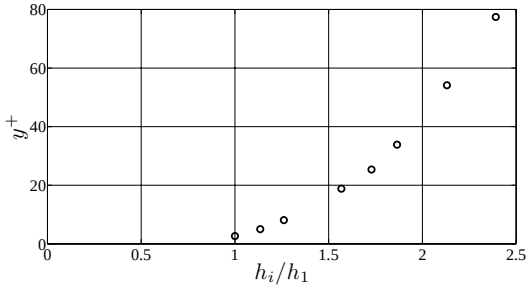

Figure 6.7 Average y^+ values for different bare hull mesh refinement ratios at $Fn = 0.488$.

Figure 6.7 shows the average y^+ values on the wetted part of the hull obtained for different mesh refinement ratios at $Fn = 0.488$. For the finest mesh the average y^+ is almost equal to 3. In Figure 6.6 a large step in the resistance coefficient of the bare hull is noticeable. This step occurs between the grids just below the refinement ratio of 2. In Figure 6.7 it is seen that the average y^+ value for the coarser grid among these two is above 30 and for the finer grid is below 30. This raises the question whether the sudden drop in the C_T curve could be due to the different treatment of the wall model above and below $y^+ = 30$; but, the grid independency study which is carried out for the waterjet driven hull geometry (Section 8.3) does not confirm this speculation because no rapid change can be seen in the resistance coefficient curve between the meshes which have average y^+ above and below 30. The variation of the self-propelled hull resistance coefficient is smoother than that of the bare hull. This might be related to the unsteadiness of the flow which possibly are less at the speed which the self-propelled hull grid independency study is carried out, $Fn = 0.798$, rather than the bare hull grid independency study at $Fn = 0.488$.

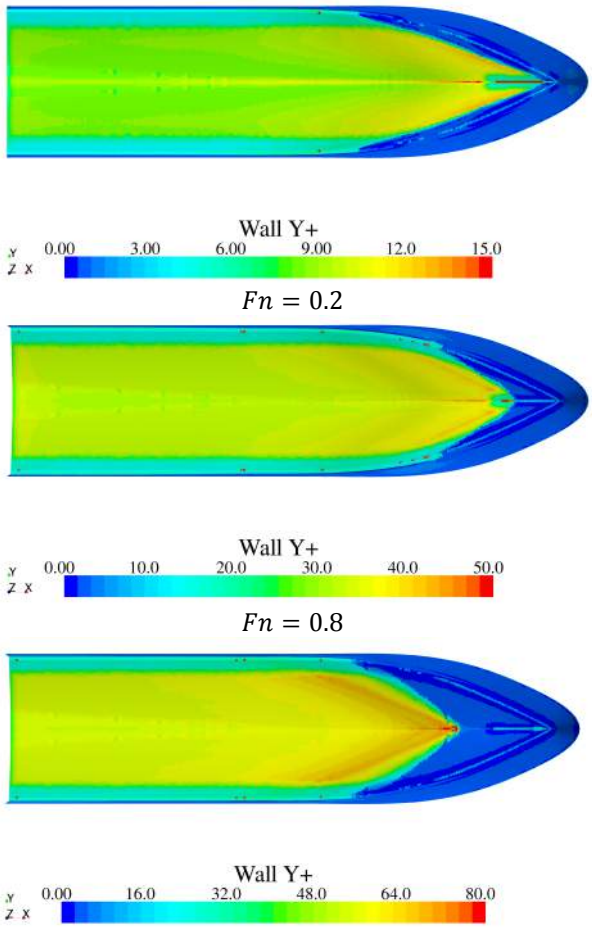

Figure 6.8 y^+ contour on the hull at different speeds.

6.4 Computational Results

A general impression of the solution accuracy may be obtained from Figure 6.9, showing the computed and measured free-surface. According to this figure, the detachment position of the free-surface and the breaking structure of the bow wave are very similar in the computed and measured results. The wave pattern around the fixed hull at three different speeds is shown in Figure 6.10. The wave pattern for the free hulls are very similar to the ones shown in this figure.

The computed and the measured draft change at the fore and aft perpendiculars of the hull at different speed ranges are plotted in Figure 6.11. Both the fore and aft drafts are under-predicted compared to the measured values but overall there is a good agreement with the measured ones. The trim angle of the hull can be calculated based on the given fore and aft draft variations. Figure 6.11 shows the comparison between the computed and the measured bare hull trim angle.

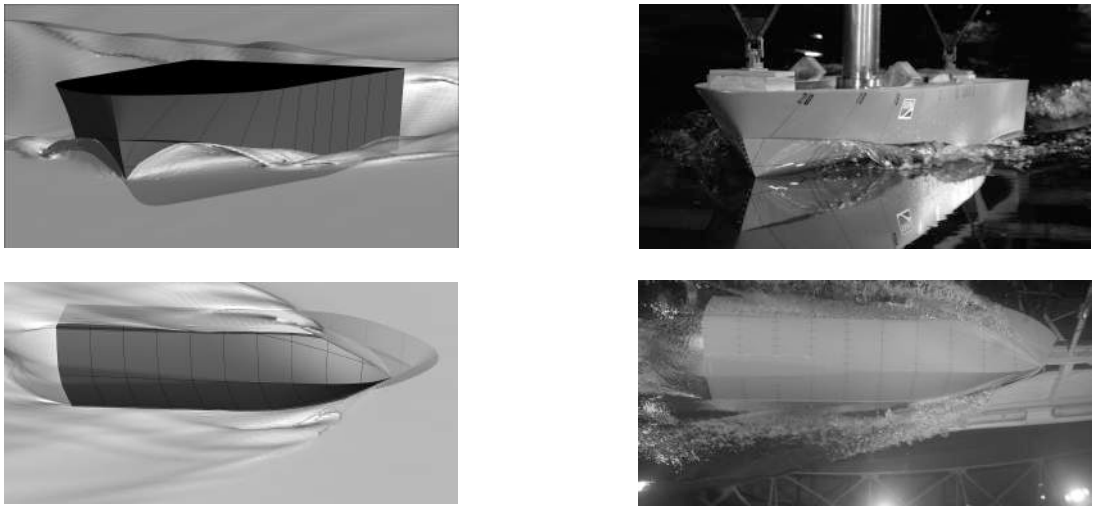

Figure 6.9 Comparison of the computed free-surface with the real free-surface from the towing tank at *Fn*=0.508.

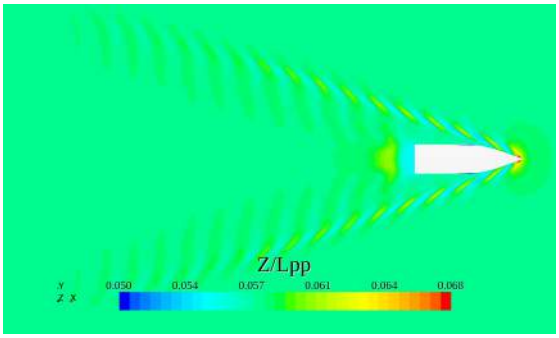

Fn = 0.2

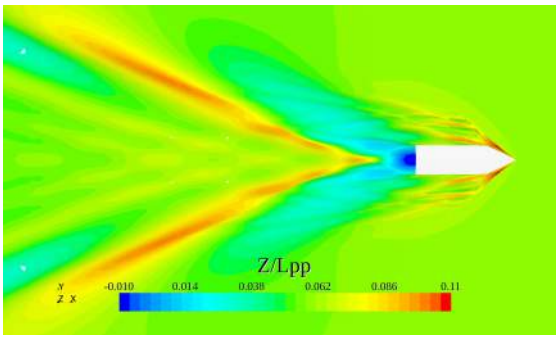

Fn = 0.8

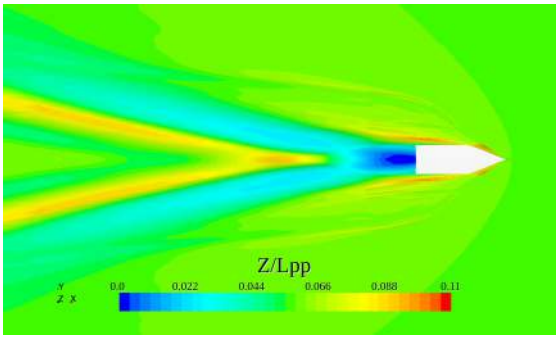

Fn = 1.4

Figure 6.10 Wave pattern around the fixed bare hull at three different Froude numbers. Countours are showing the wave height non-dimensionalized with Lpp.

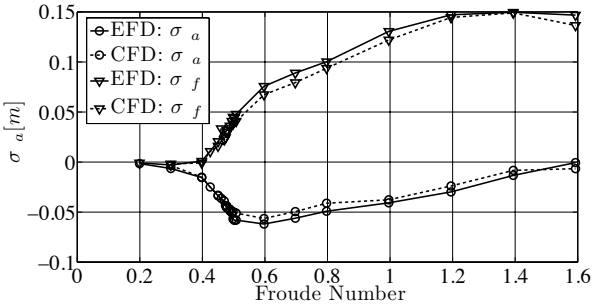

Figure 6.11 Comparison of the bare hull computed fore draft, σ_f, and aft draft, σ_a, with the measured ones.

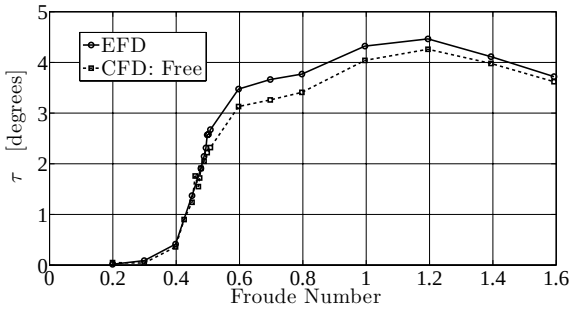

Figure 6.12 Comparison of the computed and measured trim angle.

Figure 6.13 shows the measured and the computed bare hull resistance. The computed resistance is given both for the bare hull, that has the same sinkage and trim as the measured values and the hull which is free to heave and pitch. The resistance computed from the fixed hull has better match with the measured resistance, as expected.

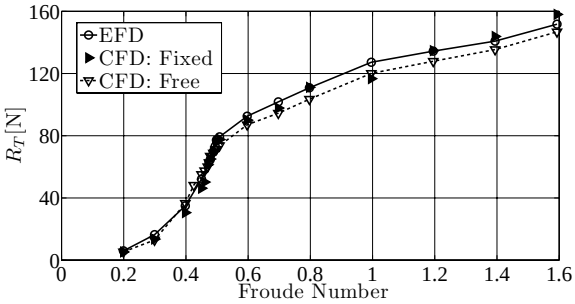

Figure 6.13 Comparison of the computed total bare hull resistance (fixed and free) with the measured resistance.

The comparison of the computed transom clearance Froude numbers (critical Froude number) with the observed transom clearance Froude number of the measurements reveals that the computed critical Froude numbers are slightly under-predicted for both the fixed and free hulls. The measured critical Froude number is within the range $0.494 < Fn \leq 0.498$ whereas the computed ones are within the range $0.470 < \mathrm{Fn} \leq 0.478$.

7 Transom Clearance

In a resistance test of the SSPA hull an unexpected peak in resistance was detected. The peak occurred close to the hump speed, but was much sharper than the expected smooth maximum in the resistance curve caused by the bow and stern wave interaction. Further inspection revealed that the peak occurred exactly at the speed where the water cleared the transom. Intrigued by this finding a systematic investigation, including further testing and CFD computations, went on to explore the physics of the phenomenon. The results of this investigation is presented in the current chapter as well as in (Eslamdoost et al. 2014a).

In the following sections, first a review of the studies carried out on the transom clearance is presented. Then the measured data for the SSPA hull at different initial trim angles are presented and discussed. This section is followed by the discussion of the results of the numerical simulations of the flow around the SSPA hull. Finally, employing the computational data, the resistance components of the hull are obtained and analysed in detail to investigate the connection between the sudden increase of the resistance and the transom clearance.

7.1 Previous Studies

Transom sterns are required for hulls in the semi-planing and planing speed regimes. The larger the speed the larger the optimum transom, see (Larsson & Raven 2010). At speeds below the critical one, where the transom clears the water, a dead-water region is developed and the water is dragged behind the hull. The transom thus has a profound influence on the resistance of the hull, and studies exploring the flow physics of transom stern flows are of great interest in high-speed hull design.

An early paper on transom stern hull forms is that of Mercier and Savitsky (1973), where a drag prediction algorithm for speeds in the pre-planing speed regime is proposed. The transom clearance phenomenon was studied by Oving (1985). In this study he provides an

empirical formula for the transom clearance Froude number as a linear function of the hull breadth to transom draft ratio.

Maki et al. (2006) conducted experiments with a series of geosim models of a destroyer. They measured the elevation of the water behind the vessels and demonstrated a relation between the static transom draft Froude number and the free-surface elevation. A regression formula for estimation of the transom clearance as a function of the beam-to-draft ratio, transom-draft Froude number and Reynolds number was developed. It is shown in the paper that there is a minor effect of free sinkage and trim on the critical Froude number comparing with a fixed model. Finally, they point out the importance of the wave field just external to the transom on the clearance, which for instance occurs earlier if the wave trough is located near the transom.

Aiming at improving the traditional thin-ship formulation for resistance prediction, Doctors et al. (2007) tried to provide a model for the transom hydrostatic drag. The wave elevation behind the transom was measured for a series of simplified hull models with rectangular cross sections. Although the models had different characteristics, the scales were of the same order for all of them. The measured transom flow of the different cases showed that the water level drop at the transom is not monotonous with speed but has a wavy trend. The same regression formula as employed by Maki et al. (2006) was employed to estimate the progression of the transom clearance. In contrast with an earlier study carried out by Doctors (2006), it was concluded that the there is no large influence of the transom-draft Reynolds number on the transom clearance. The contradictory conclusions in these two studies were due to the different measurement techniques used for the detection of the wave elevation at the transom.

Maki (2006) in his doctoral thesis studied the transom stern hydrodynamics experimentally and numerically. A comprehensive literature review on transom flow research can be found in this thesis. Maki discusses different flow regimes representing different characteristics of the free-surface behind the hull as well as the causes of the free-surface unsteadiness. The ventilation of the transom is also investigated in this thesis.

Employing a free-surface fitting RANS method Starke et al. (2007) studied the viscous and potential flow of a 2D transom stern in different regimes by increasing the transom immersion. They show that, due to the less steep wave height in potential flow in comparison with viscous flow, the critical Froude number decreases when viscous effects are neglected. They also demonstrate that the clearance occurs earlier at full scale comparing to the model scale and therefore the transom resistance coefficient is larger at full scale than for the model scale. Assuming a constant base pressure coefficient at the transom they formulate a simple model for the transom resistance.

The same method and solver was used by van der Ploeg and Starke (2013) to investigate the transom flow regimes and the scale effects on this flow for different 3D transom geometries. Comparing model and full scale simulations they show that the scale effects on the free-surface are mainly observed behind the transom. The wavelength is longer and waves are less steep in this region at full scale.

7.2 Towing Tank Results

Figure 7.1 shows the resistance and the resistance coefficient of the towed hull in a Froude number range between 0.35 and 0.65. The resistance coefficient is calculated based on the following definition,

$$C_T = \frac{R_T}{\frac{1}{2}\rho S_{ref} U^2}, \qquad (7\text{-}1)$$

where R_T is the total resistance of the hull, ρ is the water density, S_{ref} represents the wetted surface of the hull at rest and U is the ship velocity.

As seen in the figure, there is a sharp peak in the resistance coefficient at Froude number 0.498. According to observation, this is also the critical Froude number, Fn^*, where the transom becomes fully ventilated. To verify that the peak is really located at the critical Froude number very small steps were taken in the Froude number around the peak.

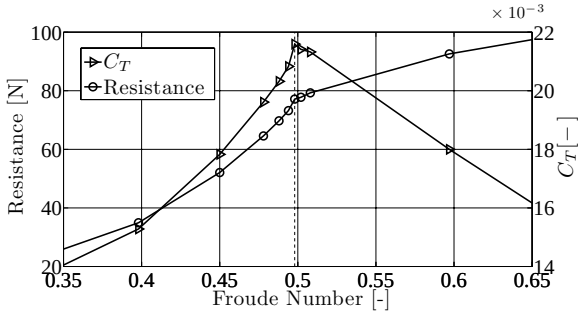

Figure 7.1: Measured resistance and resistance coefficient curves for the even keel hull. The vertical dashed line shows the critical Froude number.

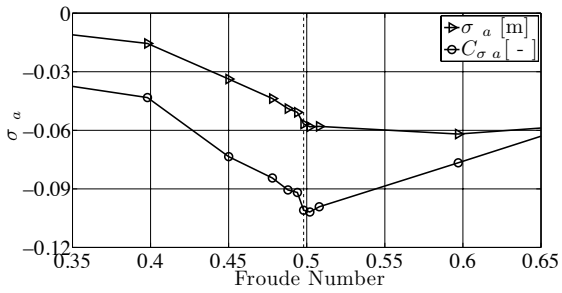

Figure 7.2: Measured aft-draft changes for even keel hull. The vertical dashed line shows the critical Froude number.

Figure 7.2 depicts the measured variation of the hull aft-draft, σ_a. The vertical axis of the coordinate system is pointing upwards and therefore a negative draft change means that the hull has moved downwards. The measured aft-draft increases rapidly just before the critical Froude number, thereafter becoming almost constant, but with a global maximum close to Froude number 0.6. Defining an aft-draft coefficient as,

$$C_{\sigma_a} = \frac{\sigma_a}{Lpp} \cdot \frac{1}{Fn^2}, \qquad (7\text{-}2)$$

where Lpp and Fn are length between perpendiculars and Froude number respectively, a local sharp peak is noted. This occurs at $Fn = 0.502$, very close to the critical Froude number which is at 0.498. It should be noted that the difference in sinkage between these two speeds is very small, much smaller than the correction of the measured sinkage due to the varying distance between rail and water surface, so the difference may well be within the measurement accuracy.

There is thus a sharp peak both in resistance and aft-draft coefficients at the critical Froude number. However, the peak occurs close to the maximum of the resistance hump, caused by the interaction between the bow wave and the rooster tail wave around $Fn = 0.5$, and to separate the peak from the hump maximum two other tests were carried out. The LCG of the hull was first moved aft and then forward, to change the initial trim angle of the hull. Two rather extreme trims around ± 4 degrees were then obtained, and the tests were repeated. Figure 7.3 shows the contours of the hull at the three attitudes.

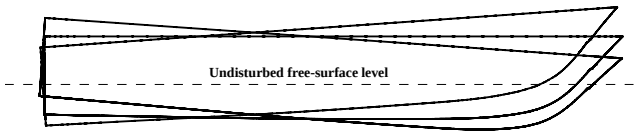

Figure 7.3: Contours of the hull for even keel, bow-up and bow-down trimmed hulls

The resistance and resistance coefficient for the hull at the bow-up trim are depicted in Figure 7.4. The critical Froude number for this case is 0.528, which is marked by a dashed vertical line in the figure. Comparing Figure 7.1 with Figure 7.4 it is seen that the critical Froude number is increased by trimming the hull bow-up. The transom submergence is increased almost by 55%, explaining the delayed transom clearance.

As seen in Figure 7.4 the (dimensional) resistance increases with Froude number, but exactly at the clearance there is a local jump. Investigating the resistance curve in coefficient form reveals the existence of two maxima. One is the rather smooth global maximum in the C_T curve corresponding to the hump at $Fn = 0.5$. The other maximum is at the critical Froude number and is more like a local jump, superimposed on the smooth global curve. Comparing the C_T curve obtained for the hull with zero initial trim angle with the trimmed hull (Figure 7.1 and Figure 7.4) it may be concluded that the peak is related to the transom clearance, not to the hump due to wave interference.

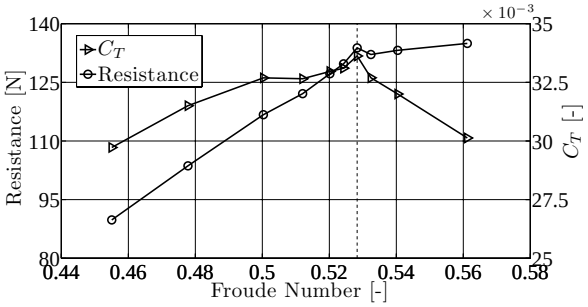

Figure 7.4: Measured resistance and resistance coefficient curves for the bow-up trimmed hull. The vertical dashed line shows the critical Froude number.

The aft-draft variation of the bow-up trimmed hull is presented in Figure 7.5. Local peaks exactly at the clearance Froude number are noted both for the draft and the draft coefficient. The dimensional transom submergence has another, smooth maximum near *Fn*=0.5 corresponding well with the C_T curve depicted in Figure 7.4.

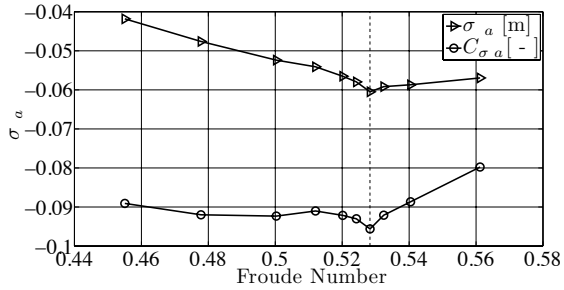

Figure 7.5: Measured aft-draft changes of the bow-up trimmed hull.
The vertical dashed line shows the critical Froude number.

Results for the bow-down trimmed hull are shown in Figure 7.6 and Figure 7.7. Surprisingly enough there is no peak in any of the curves, neither for the resistance nor the aft-draft. It should be kept in mind that this hull has an extreme bow-down trim causing the transom to be very little submerged and the buttocks to have a rather large slope upwards.

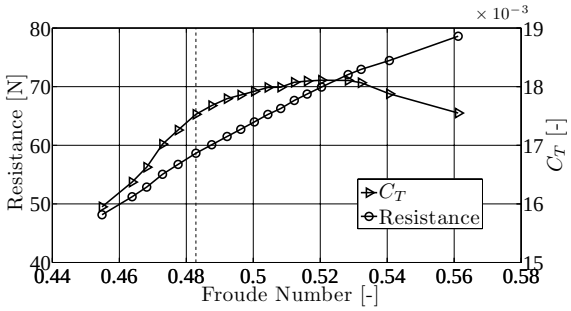

Figure 7.6: Measured resistance and resistance coefficient curves of the bow-down trimmed hull. The vertical dashed line shows the critical Froude number.

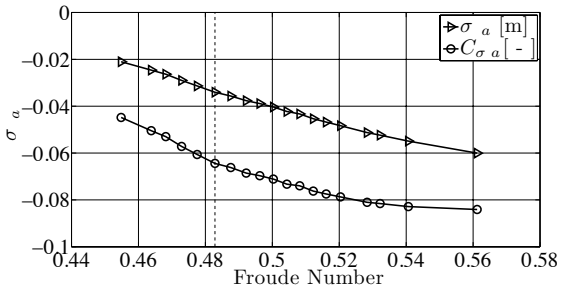

Figure 7.7: Measured fore and aft-draft changes of bow-down trimmed hull. The vertical dashed line shows the critical Froude number.

In order to gain better knowledge of the physics of transom clearance a series of CFD computations were carried out for the hull with no initial trim angle. The results are presented and interpreted in the next section.

7.3 Computational Results

A comparison of the computed bare hull resistance and the measured resistance around the critical Froude number is shown in Figure 7.8. There is a general under-prediction of the resistance and the computed critical Froude number is smaller than the measured one, 0.478 instead of 0.498. However, *the computed resistance peak occurs at the computed critical Froude number*. Therefore, although the critical Froude number is under-predicted, the computed curve confirms the correlation between the clearance Froude number and the peak in the resistance coefficient curve. The plateau of the computed resistance coefficient curve for Froude numbers $0.425 - 0.47$ will be discussed below.

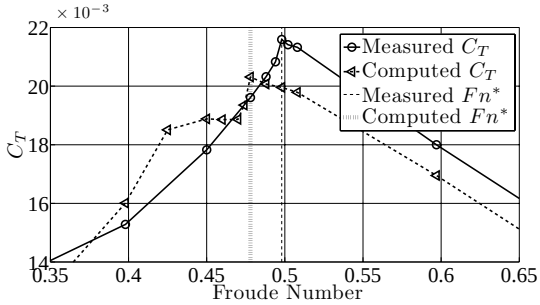

Figure 7.8: Comparison of computed and measured resistance coefficients. The vertical lines show the measured and the computed critical Froude numbers (Fn^*).

Figure 7.9 shows a comparison between the computed and measured aft-draft. The correlation is quite good below the critical Froude number, but an under-prediction is seen for higher speeds. Like the measured values, the computed aft-draft has a global (smooth) maximum at $Fn = 0.598$. This is due to the interaction of the wave systems around the hull. Figure 7.10 depicts a longitudinal wave cut at $Y/Lpp = 0.22$ for Froude numbers 0.478 and 0.597 (see figure legend for a definition of the coordinate system). The forward perpendicular of the hull is located at $X/Lpp = 0$ and the transom is at $X/Lpp = 1$. Comparing the wave cuts close to the transom it is seen that the water level is lowest for the high Froude number, where the stern thus sinks deeper.

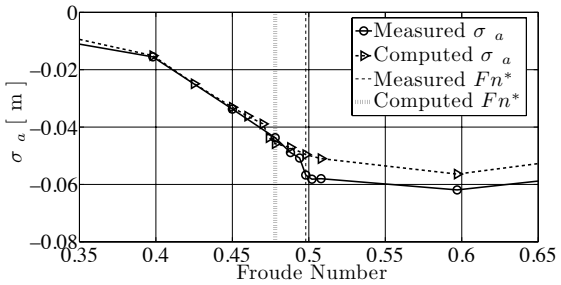

Figure 7.9: Comparison of computed aft-draft and measured values. The vertical lines show the measured and computed critical Froude numbers (Fn^*).

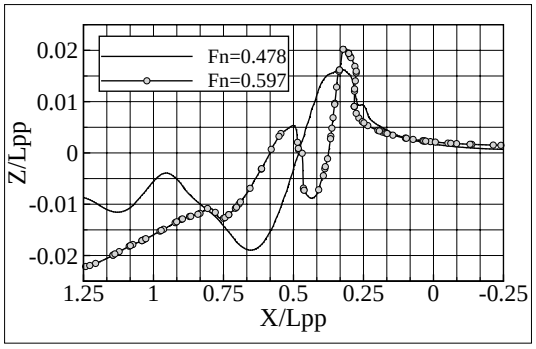

Figure 7.10: Longitudinal wave cuts at $Y/Lpp = 0.22$. The coordinate system has its origin at the zero speed bow waterline, X points backwards, Y to starboard and Z vertically upwards.

The local peak in aft-draft coefficient, defined in Equation (7-2), is seen in Figure 7.11. Like for resistance, *the computed aft-draft coefficient has its maximum exactly at computed critical Froude number*. In the following, the computed flow field is post-processed in more detail, to provide insight into the physics of transom ventilation.

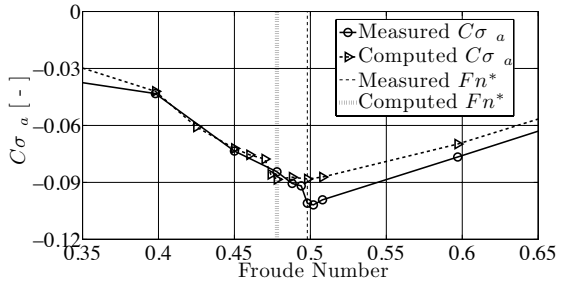

Figure 7.11: Comparison between the computed and measured aft-draft coefficients. The vertical lines show the measured and computed critical Froude numbers (Fn^*).

Since it may be suspected that the aft-draft peak is, at least, part of the explanation for the resistance peak, an investigation of the reasons for the aft-draft peak was first made. As the hull is sucked down, the pressure coefficient on the aft body is of interest. The pressure coefficient is defined as follows,

$$c_p = \frac{p}{\frac{1}{2}\rho U^2}, \qquad (7\text{-}3)$$

where p is the hydrostatic/hydrodynamic pressure, ρ is the water density and U is the ship velocity.

A plot of the pressure coefficient at the transom edge is seen in Figure 7.12. This is obtained for a range of Froude numbers, where the hull was kept at constant sinkage and trim, equal to that at the computed critical Froude number, 0.478. The data plotted in this figure shows the computed hydrodynamic pressure coefficient as well as the theoretical hydrostatic pressure coefficient for speeds from the critical one upwards. When the transom is dry the total pressure at the transom edge is atmospheric; hence the hydrostatic and hydrodynamic pressures must balance each other, i.e. their numerical values must be the same, but the signs different. To facilitate comparison, the hydrostatic pressure has been plotted with a negative sign in the figure. Unfortunately, the computed hydrodynamic pressure coefficient is scattered due to the unstructured grid at the transom edge (the grid is very irregular just at the edge), but in general there is a very good agreement with the theoretical hydrostatic pressure coefficient, which looks like a mean line through the scattered points. The most important conclusion from the figure is that the *minimum pressure coefficient on the bottom near the transom occurs at the clearance Froude number*. Note that this is not caused by the aft-draft maximum at this speed, since the computations were carried out at constant draft.

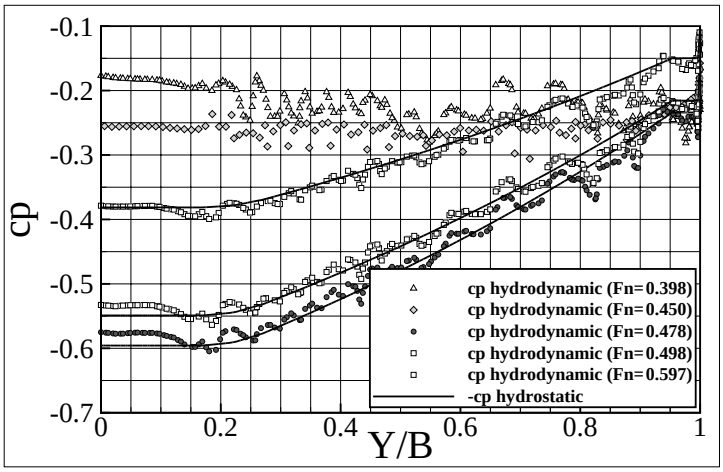

Figure 7.12: Hydrodynamic pressure coefficient at the transom edge beneath the hull.

To further explore the minimum in pressure coefficient at the critical Froude number, the curvature of the streamline in the symmetry plane leaving the transom edge was investigated for the hull with fixed sinkage and trim. Figure 7.13 depicts the position of the free-surface behind the transom and the streamline from the edge at one sub-critical and one super-critical Froude number. For the sub-critical case, the free-surface and the streamline from the transom edge are well separated, while they have merged for the super-critical case. When the transom is still wet the edge streamline separates the recirculating zone behind the transom from the flow moving backwards.

The shape of the streamline leaving the transom edge at different Froude numbers is presented in Figure 7.14. In Figure 7.14 (a) Froude numbers below the critical one are presented, and in Figure 7.14 (b) Froude numbers above that speed are displayed. It is seen that the curvature of the streamline increases with speed up to transom clearance (Figure 7.14 (a)), thereafter decreasing (Figure 7.14 (b)). Thus, *the curvature has its maximum value at the*

critical speed. The maximum curvature creates the minimum pressure coefficient at this speed, which in turn causes the local peak in aft-draft coefficient.

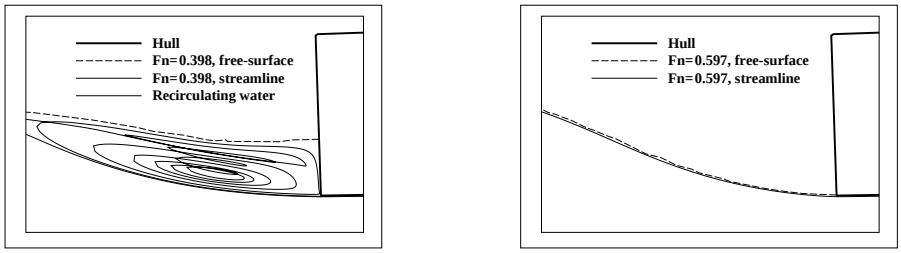

(a) (b)

Figure 7.13: The free-surface behind the hull and the streamline leaving the transom at (a) a subcritical and (b) a supercritical Froude number.

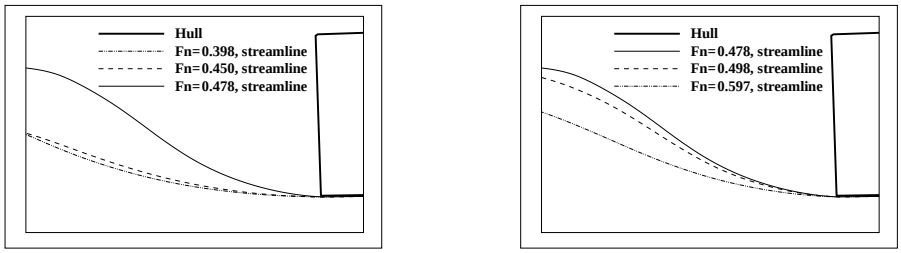

(a) (b)

Figure 7.14: Streamlines leaving the transom edge at different Froude numbers. (a) subcritical and (b) supercritical Froude numbers. The full line corresponds to the critical Froude number (0. 478)

However, it is not the aft-draft *coefficient* that causes a peak in the resistance coefficient; it is the shape of the underwater body, which changes with the dimensional aft-draft. This depends on the dimensional pressure, which is presented along the centreline in Figure 7.15 for the same Froude numbers as in Figure 7.12. It is seen that the pressure in the stern region drops rapidly between $Fn = 0.450$ and 0.478, thereby sucking down the stern, and causing a jump in the aft-draft. There is a further small drop until $Fn = 0.597$, which together with the peak in bow pressure causes the global smooth maximum in aft-draft (This explanation is consistent with that referring to the wave cut of Figure 7.10). The influence of the aft-draft sinkage on the pressure resistance of the hull may thus be expected to have an asymmetric shape. The jump in aft draft is seen both in the measured and computed curves, although the critical Froude numbers are slightly different.

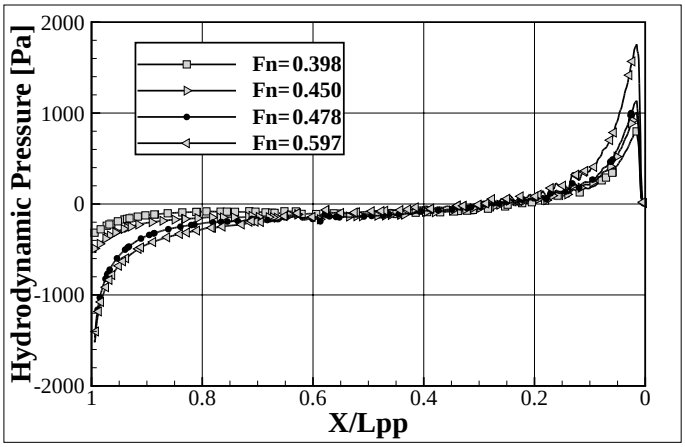

Figure 7.15: Pressure distribution along the centerline at different Froude numbers. The coordinate system has its origin at the zero speed bow waterline and X points backwards

Having investigated the aft-draft variation around the critical Froude number the resistance peak may be further explored. This can be done by studying the evolution of the hydrostatic and hydrodynamic resistance components, both on the transom and the hull, as the Froude number increases. This investigation was carried out for the hull with free sinkage and trim and is presented in the following.

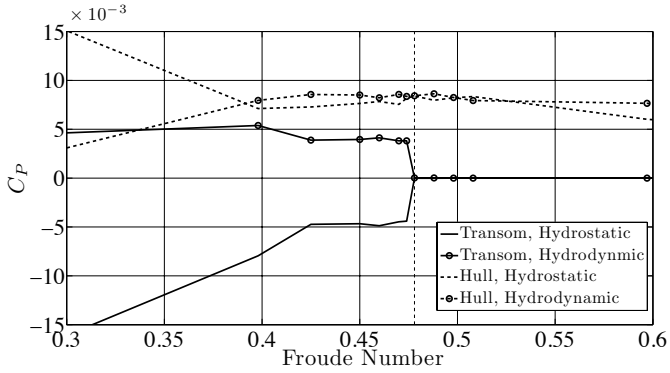

Figure 7.16: Variation of the hydrostatic and hydrodynamic pressure resistance of the transom and the hull sides. The vertical dashed line represents the critical Froude number.

Figure 7.16 depicts the variation of the hydrostatic and hydrodynamic force coefficients of the transom and the hull. The sum of the four force coefficients of Figure 7.16 and the frictional and aerodynamic resistance coefficients should result in the C_T presented in Figure 7.8. The full lines of Figure 7.16 represent the transom force components and the dashed lines the force components of the rest of the hull. It is seen that the hydrostatic force on the transom, directed forwards, decreases rapidly with Froude number, and drops abruptly to zero where the transom is fully ventilated. The transom hydrodynamic force curve has a different trend, however. It is almost constant over a wide range of Froude numbers, but just like the hydrostatic component, it drops abruptly to zero as the transom becomes dry. Close to the critical Froude number the hydrostatic and hydrodynamic force coefficients of the transom have a comparable magnitude but opposite signs, hence they partly cancel each other and the total transom force is relatively small. It is directed forwards, however, and the rapid drop of this thrust is one of the contributions to the resistance peak. This is clearly seen in

Figure 7.17, which shows the development of the total transom pressure resistance in a Froude number range around the critical one.

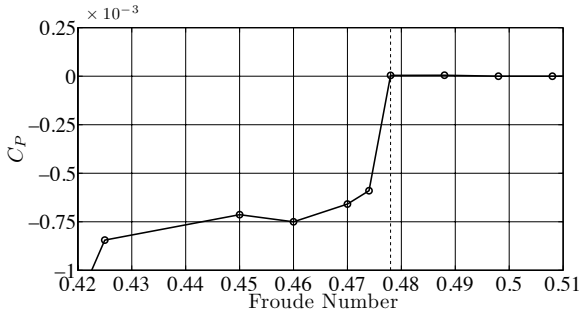

Figure 7.17: Transom total pressure resistance coefficient (negative: points forward). The vertical dashed line represents the critical Froude number.

Referring again to Figure 7.16, the hydrostatic force on the hull is very similar to that of the transom in the low speed range, but with the opposite direction, i.e. backwards. The total hydrostatic force is thus very small, as can be expected at low speed. Above $Fn = 0.40$ the hydrostatic force on the hull becomes more constant than that at the transom. There is however a small jump just before the critical Froude number. The hydrodynamic force coefficient develops more smoothly in the entire speed range. Adding the two components for the hull Figure 7.18 is obtained. The general shape corresponds to the resistance hump, but with a local jump at the critical Froude number (due to the hydrostatic force). It is this jump, together with the rapid drop in transom thrust force (Figure 7.17) that creates the peak in the total resistance coefficient. Since both effects occur just before the critical Froude number the peak must be asymmetric. Inspecting the resistance curve of Figure 7.1 it is seen that this is indeed the case. The reason why the resistance coefficient decreases to the right of the peak is that it is located at the hump maximum. (For the bow-up case, Figure 7.4, the peak is to the right of the hump maximum, which causes a larger drop to the right of the peak and makes it look almost symmetric.)

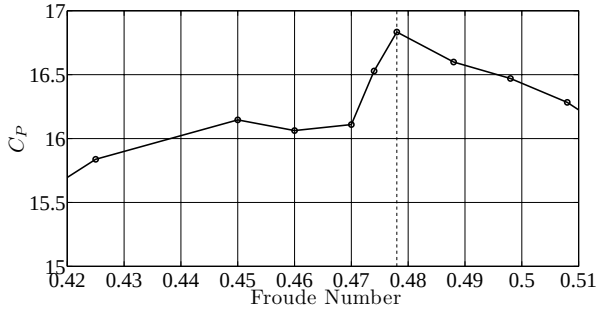

Figure 7.18: Hull total pressure resistance coefficient. The vertical dashed line represents the critical Froude number.

There is one feature of the computed resistance coefficient of Figure 7.8 that needs to be discussed. It is the plateau in the resistance coefficient curve between Fn = 0.45 and 0.47. This does not seem to be present in the measured data, but there are too few points in this region to draw a firm conclusion. Anyway, the reason for this plateau in the computations is that when the hull transom sinks rapidly just before it is about to clear, the clearance is

delayed. This is clearly borne out in Figure 7.19, showing the variation with Froude number of wetted surface area of the transom. A plateau is seen at the Froude numbers in question. This also causes a plateau in the transom resistance components in Figure 7.16.

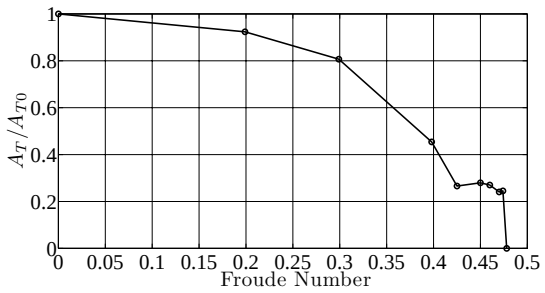

Figure 7.19: Non-dimensional transom wetted surface area.

The CFD investigation was carried out for the even keel case to explore the physics of the transom clearance. All effects found for this case are likely to be present also for the bow-up case, which shows the same effects on resistance and aft-draft, perhaps even more pronounced. However, no effects were detected for the bow-down case. A major reason for this must be that the bottom has a large upwards slope. The flow leaving the transom edge will have a much smaller curvature going up behind the hull. Possibly, the flow will even bend downwards. There will be a very different effect on the aft-draft. Further, the submergence of the transom (at zero speed) is very small, reducing the effect of the drop in transom trust. Finally, since the peak is asymmetric, it will be less visible if it is located to the left of the smooth hump maximum.

8 Self-propulsion RANS Method

In this section, first, the method used for carrying out the numerical simulation of waterjet hull self-propulsion is presented, followed by a verification study of the numerical method. Then the measurement technique used at SSPA for carrying out the self-propulsion tests is discussed briefly. Before getting started with the validation of the computed self-propulsion results, the steps carried out for obtaining the gross thrust in the numerical simulations are presented. Most of the results from this part need to be at hand before starting with the validation, therefore the comparison of the computed results with the measured values is shown late in this Chapter.

8.1 Numerical Method

The numerical method and solvers which are employed for modelling the self-propulsion is the same as the ones used for the simulation of the bare hull flow. The flow field around the self-propelled hull is modelled at the same Froude numbers as the bare hull to facilitate comparison. The hull sinkage and trim are fixed to the measured ones from the towing tank self-propulsion measurements. To model the propulsion system the waterjet geometry including the shaft and hub is used, but instead of modelling the actual geometry of the impeller an axial body force is uniformly distributed inside the volume containing the actual geometry of the impeller. The magnitude of the body force is set to be equal to the computed total resistance of the entire system of the hull and the waterjet unit minus the rope force applied to the hull during the self-propulsion test for unloading the propulsor due to the higher frictional resistance in the model scale.

8.2 Hull and Pump Geometry

The hull geometry used in this study is the SSPA hull introduced in Section 6.2. For the self-propulsion test the hull was equipped with a single waterjet propulsion unit designed by Rolls-Royce (Figure 8.1). The positioning of the waterjet unit on the SSPA hull is shown in Figure 8.2. During the measurements, which were carried out in the SSPA towing tank, the waterjet unit was mounted on the hull throughout both the resistance and self-propulsion test,

but during the resistance test the intake opening was covered and the unit was filled with water to create the same initial conditions for the bare hull and self-propelled one.

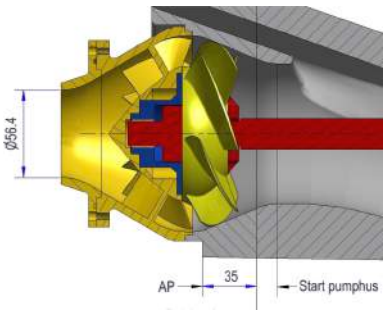

Figure 8.1 Waterjet pump geometry (dimensions are in *mm*).

Figure 8.2 Positioning of the waterjet unit.

8.3 Mesh Generation and Verification

Like in the bare hull simulation, the flow around the self-propelled hull is considered to be symmetric with respect to the xz-plane and therefore only half of the geometry is used is the simulation. An exception is the computations presented at the end of Section 9.2.3, where the differences between the swirling jet flow and the swirl free jet are discussed. There, the flow cannot be considered symmetric anymore and therefore the computational domain used for that specific investigation includes the entire hull geometry. For the sake of the mesh consistency between the bare hull simulations and the ones for the waterjet driven hull it is tried to keep the grid generation technique as well as the mesh size and mesh distribution the same as for the bare hull. However, the geometries are not exactly the same and a larger number of cells is required for the self-propulsion computational domain to generate the grid inside the waterjet unit. Besides, since the flow details into the waterjet intake and the discharged flow out of the nozzle are of interest, the mesh in these regions are refined further (Figure 8.3).

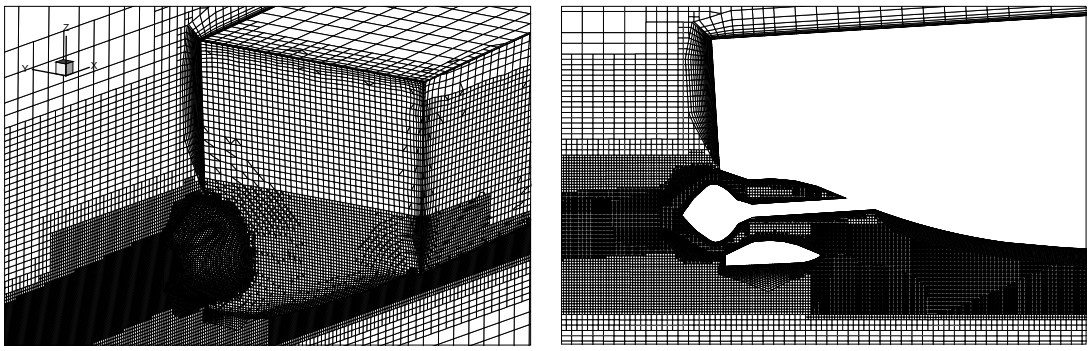

Figure 8.3 Grid distribution on the hull (left) and inside the ducting channel (right) .

Like for the bare hull, to obtain a suitable cell size, and hence total grid number, a systematic grid refinement study was carried out for the self-propulsion. Multiple grids with systematically varied grid parameters were used at Froude number 0.798. The mesh convergence study was carried out by studying the resistance coefficient of the waterjet driven hull which is defined as follows,

$$C_T = \frac{R_T}{\frac{1}{2}\rho S_{ref} U^2}, \qquad (8\text{-}1)$$

where R_T is the total resistance of the self-propelled hull (*including the waterjet unit*), ρ is the water density, S_{ref} represents the wetted surface of the hull at rest and U is the ship velocity.

The total resistance coefficient convergence curve for the self-propelled hull is plotted in Figure 8.4. Since the grid is unstructured the step size h_i on the horizontal axis is obtained as the third root of the total number of cells for grid i. The finest grid is denoted by h_1. The total number of cells for this grid is $16.2E6$ and for the coarsest grid it is $1.2E6$.

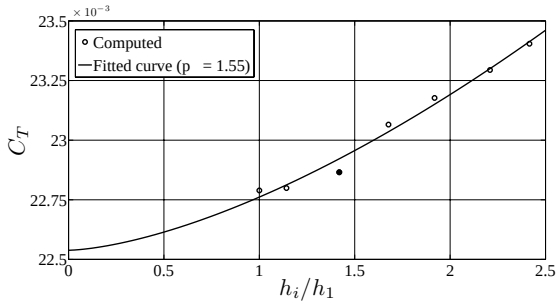

Figure 8.4 Convergence of the total resistance coefficient with grid refinement at $Fn = 0.798$ for the waterjet driven hull. The full symbols show the grid employed to perform the calculation for the entire range of Froude numbers. The p-value is the power of the best fit expression for the error according to Eça and Hoekstra (2014).

The formal verification which is carried out based on the Least Squares Root method by Eça and Hoekstra (2014) indicates that a good compromise between numerical accuracy and computational effort is obtained with the grids shown by the full symbols in Figure 8.4, which is selected for further self-propulsion computations. The total number of cells for this grid is $5.7E6$. The numerical uncertainty for this grid is 2.3% of the computed resistance coefficient. The average y^+ values on the wetted surfaces for each refinement ratio is given in Figure 8.5. The y^+ value for the finest and the coarsest meshes are almost 10 and 130, respectively. The y^+ contour on the waterjet driven hull at different speeds is shown in Figure 8.6. The y^+ distribution on the waterjet-propelled hull is almost the same as on the bare hull at the same speeds (Figure 6.8). This confirms the uniformity of the bare hull and self-propelled hull grids.

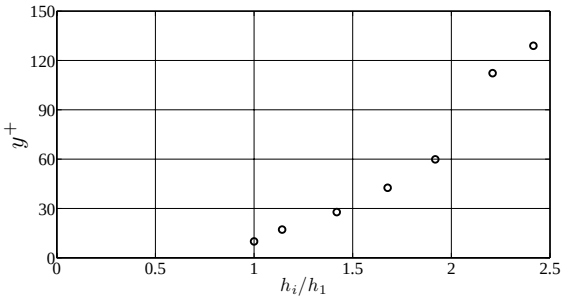

Figure 8.5 Average y^+ values for different bare hull mesh refinement ratios at $Fn = 0.488$.

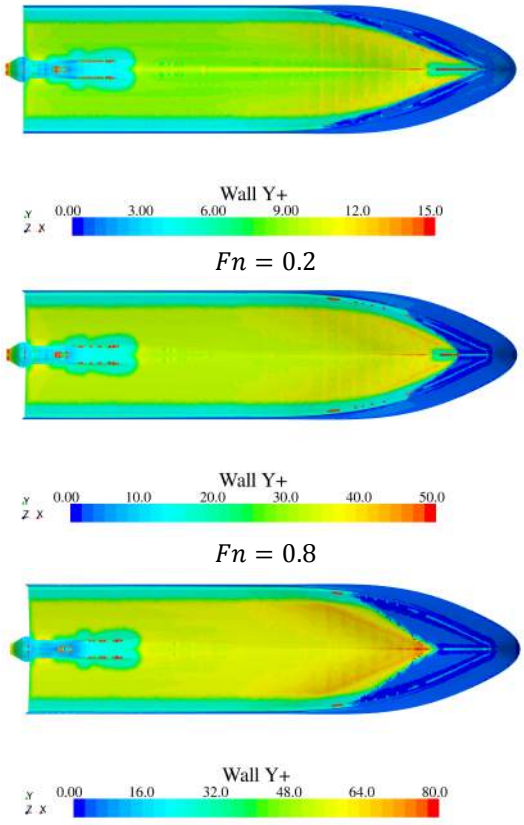

Figure 8.6 y^+ contour on the self-propelled hull at different speeds.

8.4 Self-propulsion Measurements

In this section, first, the self-propulsion measurement technique, which was used at SSPA (Brown 2013), will be discussed. Then, the measured sinkage and trim values from the self-propulsion tests are presented and compared with the values obtained from the bare hull resistance tests.

8.4.1 Measurement Technique

The method employed at SSPA to measure the flow rate through the waterjet unit is based on a method different from that suggested by the ITTC Specialist Committee on Waterjets. In this method using a T-junction, it is attempted to redirect the nozzle discharged flow perpendicular to the nozzle exit. The T-junction alignment respect to the nozzle exit flow is shown schematically in Figure 8.7.

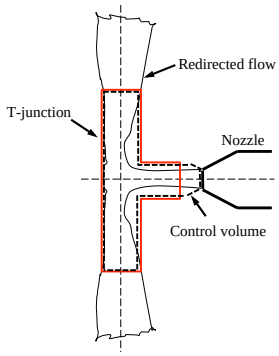

Figure 8.7 Schematic presentation of the T-junction redirecting the flow 90° sideward.

Since the redirected flow out of the T-junction has no force or momentum flux component in the axial direction (i.e. along the pump shaft), the axial momentum flux balance equation for the T-junction control volume (the closed dashed line shown in Figure 8.7) would be as follows,

$$F_T - \iint_{A_8} p dA = \iint_{A_8} \rho u^2 dA, \qquad (8\text{-}2)$$

where F_T is the axial force exerted on the T-junction. The second term on the left hand side represents the pressure force exerted on the nozzle exit area, A_8. The right hand side of this equation shows the axial momentum flux of the jet though A_8. The axial velocity of the jet is denoted u.

Introducing the momentum flux correction coefficient, c_m (Section 3.7), the right hand side of Equation (8-2) can be re-written for the volumetric flow rate of the jet. The pressure integral can be replaced by the average pressure acting over the nozzle exit area. After carrying out these changes the volumetric flow rate of the jet can be obtained as follows,

$$Q = \sqrt{\frac{(F_T - \bar{p}A_8)A_8}{\rho c_{m8}}}, \qquad (8\text{-}3)$$

where $\bar{p}$ is the average pressure over the nozzle exit area.

The momentum flux correction coefficient at the nozzle exit is computed in Section 8.5.3. It is almost equal to 1.005. This coefficient is neglected in the SSPA measurements. According to the computed c_{m8} value, this can introduce 0.25% error to the measured volumetric flow rate (the average jet velocity).

The average jet velocity at the nozzle exit can be obtained from,

$$\bar{u}_8 = \frac{Q}{A_8}. \qquad (8\text{-}4)$$

In order to calculate the gross thrust the momentum flux at the capture area is also required. In the measurements carried out at SSPA the velocity distribution at the capture area was estimated employing the power law equation for the turbulent boundary layer on a flat plate. Then, assuming a rectangular capture area with a constant width at right angles to the x-direction (ITTC 2005b), its height is calculated such that the flow rate through the area, considering the estimated boundary layer profile, becomes as large as the flow rate through the nozzle exit. After this step, the flow rate and the area of the capture area, A_1, are at hand and therefore the mean axial velocity through A_1 can be obtained as follows,

$$\bar{u}_{1x} = \frac{Q_8}{A_1}. \qquad (8\text{-}5)$$

Employing the mean velocity at the nozzle exit and at the capture area the gross thrust of the waterjet unit can be obtained using Equation (8-6),

$$T_g = \rho Q u_0 (NVR \cdot cos\,\theta_n - IVR), \qquad (8\text{-}6)$$

where NVR (Nozzle Velocity Ratio) and IVR (Intake Velocity Ratio) are the ratio of the mean velocity at the nozzle exit section and the mean axial velocity at the capture area to the undisturbed velocity, u_0, respectively. Since the nozzle exit flow may have an angle relative to the horizontal plane, θ_n, NVR is multiplied by cosine of this angle to obtain the horizontal component of the jet momentum flux. In this equation it is assumed that the velocity distribution at the capture area and the nozzle exit are uniform and therefore the momentum correction coefficient is assumed to be equal to 1 at both sections ($c_{m1} = c_{m8} = 1$, compare Equation (3-21) with Equation (3-22)). The computed momentum flux coefficients at the capture area and the nozzle exit (Section 8.5.3) show that assuming these coefficients to be equal to 1 introduces an error of 1 to 2% in the momentum flux of the jet and an error of almost 0.5% in the momentum flux of the capture area.

In practice there are some limitations and complications measuring the flow rate employing the T-junction method. First of all, the T-junction needs to be up in the air to measure the jet momentum flux. In the lower speed range, the device is fully submerged in the water behind the transom or it may partially penetrate the transom wave. In such cases the force measured from the T-junction does not represent the jet momentum flux. Besides, although the T-junction was built to redirect the flow at right angles to the nozzle discharged flow, during the measurements it was noticed that the redirected flow is not exactly perpendicular to the discharged flow; it bounced back slightly towards the nozzle after hitting the T-junction. This means that the force exerted on the T-junction is larger than for the ideal case. In order to

correct for this, the measured force on the T-junction was calibrated through bollard pull tests at various flow rates.

Self-propulsion tests are carried out in two stages. First, the waterjet-driven hull is run with free sinkage and trim and the pump shaft revolution is set such that the waterjet thrust balances the hull resistance (minus the rope force which is used for unloading the waterjet unit due to difference in the frictional resistances of the model and full scale hulls). After this step, the T-junction is assembled on the hull and the sinkage/trim and the pump revolution are set to the values obtained from the previous step. The attitude of the hull is thus fixed by vertical bars, carrying no load in the x-direction. The force exerted on the T-junction is measured and used for obtaining the flow rate through the nozzle exit. A comparison of the pump shaft torque with and without the T-junction shows very small differences and therefore, running the hull at the same equilibrium position and the same operating condition for the pump obtained from the self-propulsion measurements insures that the flow rate with and without the T-junction remains the same. Figure 8.8 shows the two steps of the self-propulsion measurements. The sinkage/trim and pump revolution is obtained from the self-propulsion measurements (left) and the flow rate is obtained at the second step using the T-junction (right).

Figure 8.8 self-propulsion test at SSPA at $Fn = 0.8$ (left: without the T-junction, right: with the T-junction)

8.4.2 Measured Self-propulsion Sinkage and Trim

The measured aft and fore draft of the bare hull (BH) and self-propelled hull (SP) are plotted in Figure 8.9. The aft and fore draft are measured at sections 0 and 20 (Figure 6.2). Comparing the aft draft of the self-propelled hull with that of the bare hull, it is seen that the transom submergence of the waterjet driven hull is larger than the bare hull transom submergence for the entire measured speed range. Figure 8.10 shows the sinkage of the hulls at mid-ship. As it was shown in Section 5.1.1 the hull sinks deeper due to the action of the waterjet unit. The measured trim angle of the bare hull and self-propelled hull is plotted in Figure 8.11. At the intermediate and higher speed ranges ($Fn > 0.6$) there is a bow down trimming moment, which causes the self-propelled hull to trim less than the bare hull. Since the aft part of the waterjet-driven hull submerges deeper at the lower speed ranges, the trim angle of the self-propelled hull becomes larger than that of the bare hull.

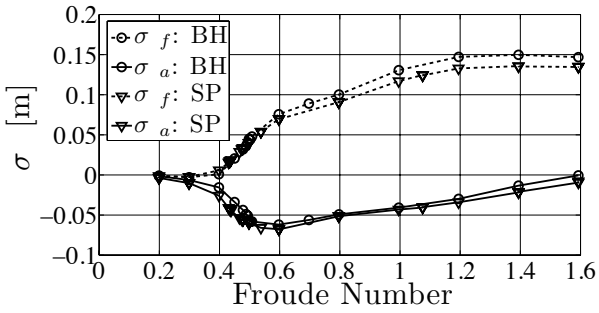

Figure 8.9 Measured fore draft, σ_f and Aft draft, σ_a of the bare hull and self-propelled hull. Negative draft means that the hull has moved downwards.

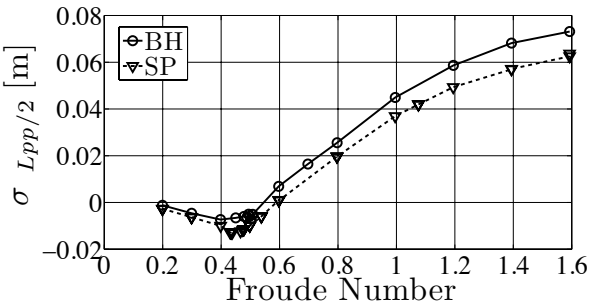

Figure 8.10 Measured sinkage of the bare hull and the self-propelled hull at mid-ship.

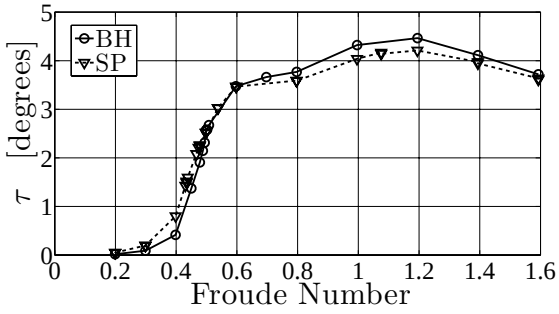

Figure 8.11 Measured trim angle of the bare hull and the self-propelled hull.

8.5 Self-propulsion Computations

The simulated jet flow and the free-surface close to the transom is shown in Figure 8.12. In The Figure 8.13 the pressure distribution inside the ducting channel is presented. The flow head increases as it reaches the region where the body force is applied to. This region starts just before the expansion of the impeller casing and continues until the impeller casing reaches its maximum diameter. Due to the increased flow head the pressure inside impeller casing and the nozzle increases but eventually adapts itself to the atmospheric pressure at the nozzle exit.

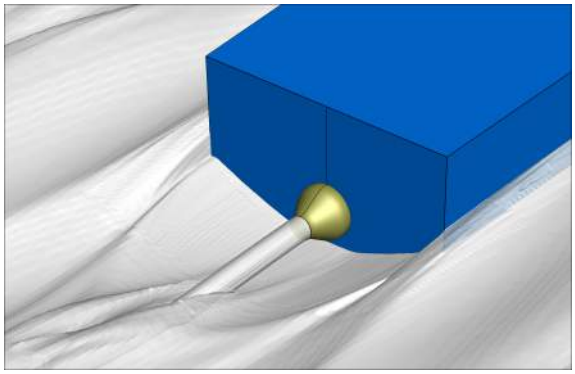

Figure 8.12 Simulated free-surface and jet flow at $Fn = 0.797$.

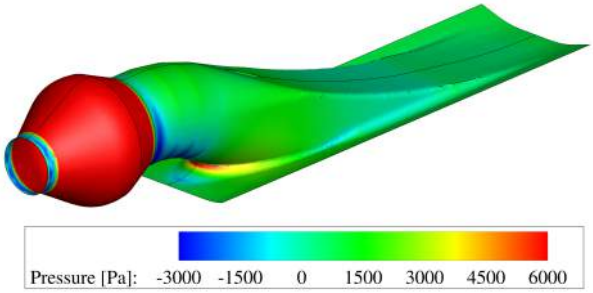

Figure 8.13 Pressure contour inside the ducting channel at $Fn = 0.797$.

In order to calculate the gross thrust of the waterjet unit the ingested momentum flux at the capture area and the momentum flux of the discharged jet at the nozzle exit are required. Since the flow field around the hull is resolved, it is possible obtain the capture area geometry.

8.5.1 Computation of the Capture Area Geometry

Using the same technique as Bulten (2008) and Ding et al. (2010), the streamtube geometry is obtained by solving a convection equation for a passive scalar in the reversed resolved velocity field. The boundary value of the scalar is set to be 1 on the nozzle exit section and 0 on the other boundaries. Then the scalar is obtained iteratively for the entire flow field. The cells inside the streamtube acquire the scalar value of 1 and those outside the streamtube acquire 0. The scalar distribution on the symmetry plane is shown in Figure 8.15. The transition of the scalar value from 1 to 0 is not sharp and its spread depends on the grid size. As shown in Figure 8.3 the grid close to the intake is refined to keep the transition zone as sharp as possible. The streamtube interface is extracted as an iso-surface of the scalar equal to 0.5 (Figure 8.15).

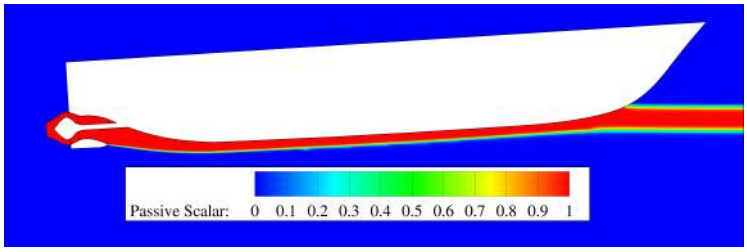

Figure 8.14 Passive scalar contour at $Fn = 0.797$.

The capture area geometry is obtained by extracting a vertical section along the computed streamtube which, as proposed by the ITTC Specialist Committee on Waterjets (ITTC 2005d), is located one intake diameter ahead of the intake tangency point to the hull. The capture area geometry and the axial velocity contour at this section are plotted in Figure 8.16 at different Froude numbers. In order to validate the capture area computation method, the continuity of the flow through the capture area and the nozzle exit needs to be satisfied. The ratio of the volumetric flow rate through the capture area to that of the nozzle exit is plotted in Figure 8.17. As seen in this plot, the deviation of the flow rate through the capture area is less than $\pm 1\%$ of the computed flow rate through the nozzle exit. A better match between the flow rate through the capture area and the nozzle exit can be achieved by refining the grid close to the intake.

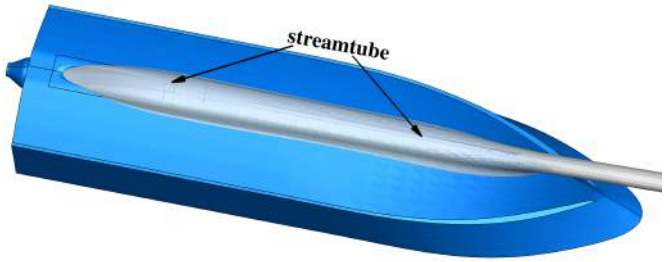

Figure 8.15 Bottom view of the hull showing the streamtube separating the flow into the waterjet intake from the rest of the flow at $Fn = 0.797$.

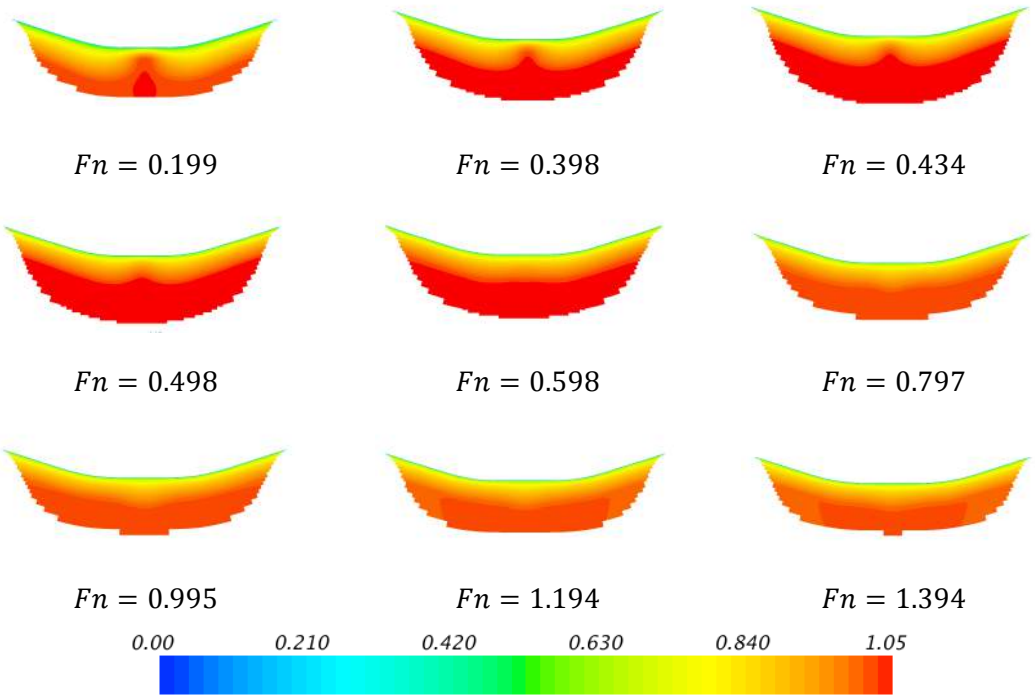

Figure 8.16 Non-dimensional axial velocity (u_1/u_0) distribution on the capture area at different speeds.

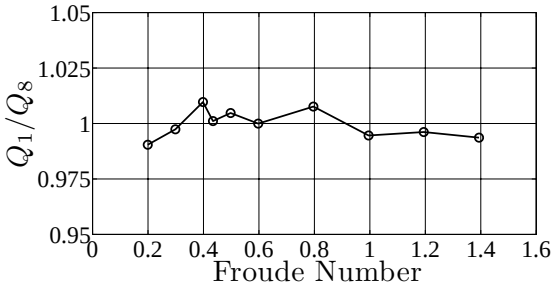

Figure 8.17 Ratio of the volumetric flow rate through the capture area to the volumetric flow rate through the nozzle exit.

The influence of the waterjet-induced flow on the velocity field close to the intake is investigated by comparing the velocity field in front of the intake for the waterjet-driven hull and the bare hull. In order to make this study independent of the sinkage and trim differences between the bare hull and the self-propelled hull, the simulations are carried out at the same sinkage and trim values. The boundary layer profile at the symmetry plane of the computational domain at the capture area as well as two other sections, one before and one after the capture area, is plotted in Figure 8.18. Closer to the intake opening the discrepancy between the self-propelled hull boundary layer profile and that of the bare hull becomes larger. The influence of the intake suction almost disappears 2.5 intake diameters in front of the intake tangency point to the hull.

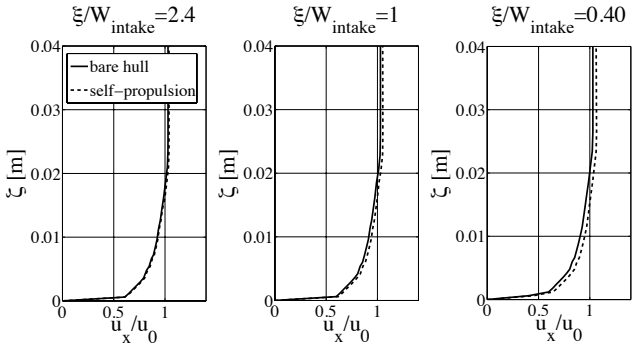

Figure 8.18 Boundary layer profile at $Fn = 0.434$ for three ξ/W_{intake} ratios, where ξ is the axial distance of the section from the intake tangency point and W_{intake} is the intake width. ξ shows the normal distance from the wall.

The variation of the capture area width, w_1, measured from the most outer corners, at different Froude numbers is shown in Figure 8.19. The width is almost constant at the lower and the intermediate Froude numbers but decreases at higher speeds. As stated in Section 3.5, the ITTC Specialist Committee on Waterjets suggests a constant capture area width for all the operating conditions (1.3 for a rectangular capture area and 1.5 for a half-elliptical capture area) but the current results are not supporting the constant capture area hypothesis.

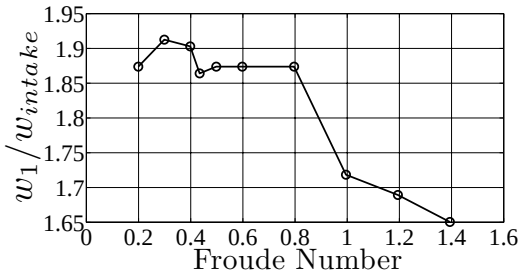

Figure 8.19 Non-dimensional capture area width over a range of Froude numbers.

The ratio of the capture area to the nozzle exit area is plotted in Figure 8.20. The size of the capture area increases with speed up to Froude number of 0.43. Thereafter it starts to decrease. This Froude number is in fact the critical Froude number where the transom of the waterjet driven hull clears water.

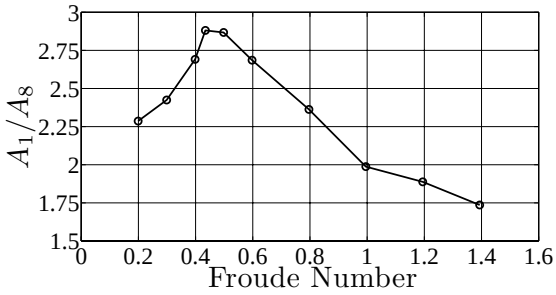

Figure 8.20 Variation of the capture area ratio to the nozzle exit area over a range of Froude number.

8.5.2 Computation of the Vena-contracta

Figure 8.21 shows the static pressure distribution on the nozzle exit section and on the vena-contracta. It is clearly seen that the static pressure on the nozzle exit is not atmospheric. The deviation from the atmospheric pressure becomes larger at the centre of the section. Moving out along the jet the average static pressure of the jet section decreases and eventually at a certain section approaches the atmospheric pressure. This section shows the location of the vena-contracta. The variation of the average static pressure along the jet is shown in Figure 8.22. The horizontal axis in this figure shows the distance between the axial coordinate of the studied cross section, x, and the nozzle exit section axial coordinate, x_8, non-dimensionalized by the diameter of the nozzle exit area, D. According to this plot the location of the vena-contracta is $0.85D$ behind the nozzle discharge section. For the specific nozzle geometry used in this study the diameter of the vena-contracta is rather insensitive to the operating speed and is almost 3% smaller than the diameter of the nozzle discharge area.

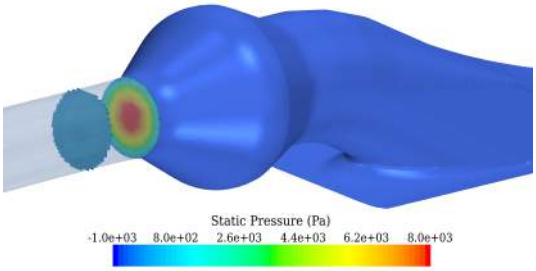

Figure 8.21 Static pressure distribution on the nozzle exit section and on the vena-contracta at $Fn = 0.797$.

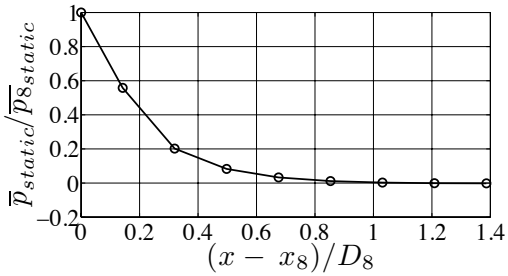

Figure 8.22 Average static pressure in different cross sections along the jet at $Fn = 0.797$.

8.5.3 Momentum Flux Correction Coefficient

The axial velocity distribution on the capture area at different speeds are shown in Figure 8.16. The distribution inside the pump, at the nozzle exit and at the vena-contracta is plotted in Figure 8.23. As can be seen, the velocity distribution is not uniform at any of these sections; thus, assuming the momentum flux correction coefficient at the capture area and at the nozzle exit to be equal to 1 will cause some error in the computation of the gross thrust. Based on the simulations carried out and using Equation (3-20) the momentum velocity coefficients c_{m_1}, c_{m_8} and c_{m_9} are computed. The actual geometry of the pump is not used in this study and it is assumed that the nozzle exit flow is swirl free, so the details of the velocity distribution at the nozzle exit and at the vena-contracta will be different than the real flow. However, obtaining the momentum flux correction coefficient at these sections can still be informative about the imposed error to the gross thrust.

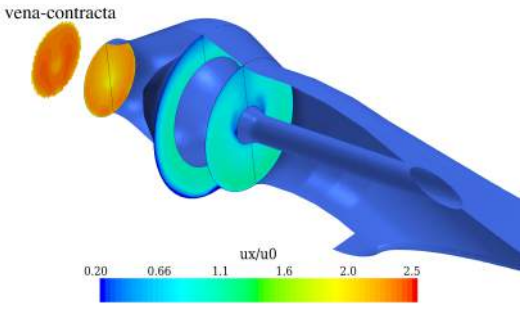

Figure 8.23 Non-dimensional axial velocity inside the pump, nozzle and at the vena-contracta at Fn=0.797.

The axial momentum flux correction coefficient of the capture area, the nozzle exit and the vena-contracta are plotted in Figure 8.24. The negligence of the momentum flux correction coefficient at the capture area cause an error of 1-2.5% over the computed range of Froude numbers. The momentum flux correction coefficient at the nozzle exit is almost constant over the intermediate and the high Froude number range and is close to 1.005. Hu and Zangeneh (2001) studied the flow inside the waterjet pump with the actual geometry of the pump and the stator blades using a RANS code. They computed the momentum flux correction coefficient at the nozzle exit to be almost equal to 1.004. The minor discrepancy between this value which is obtained from the entire pump and the stator geometry modelling with the value obtained from the simplified geometry in the current study might indicate that there is no large influence of the actual pump geometry on the non-uniformity of the discharged flow. The influence of the flow non-uniformity on the momentum flux at the vena-contracta is negligible.

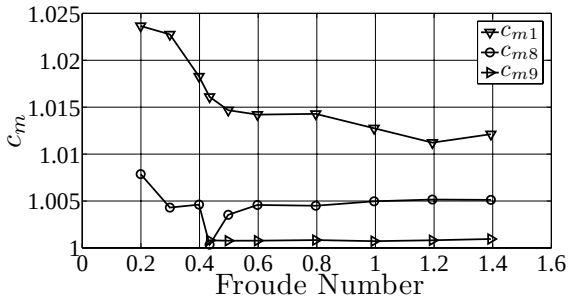

Figure 8.24 Variation of the momentum coefficient at the capture area and nozzle exit over a range of Froude number.

8.5.4 Gross Thrust and Thrust Deduction Computation

The Intake Velocity Ratio (IVR) and the Nozzle Velocity Ratio (NVR) are shown Figure 8.25. The NVR values which are presented with triangular symbols are obtained based on the measured flow rate through the nozzle but IVR values which are shown with circular symbols are obtained base on the empirical formula for the turbulent boundary layer on a flat plate and assuming the capture area to be rectangular as discussed in Section 3.8. On the average there is a discrepancy of 2% and 2.7% between the computed and measured/estimated NVR and IVR, respectively. Intake Velocity Ratio, IVR, is almost constant over the entire studied Froude number range but NVR is very dependent on the operating speed. Variations of NVR with Froude number have the same trend as the capture area size (Figure 8.20) and the humps in both curves occur at the self-propulsion transom clearance speed.

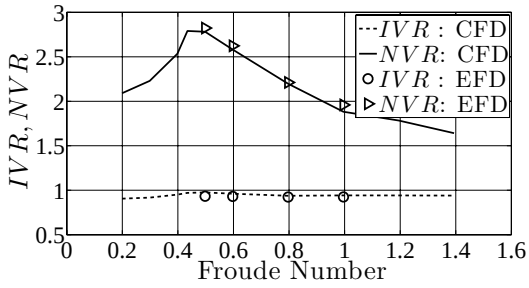

Figure 8.25 Comparison of the measured and the computed IVR and NVR.

The computed and the measured gross thrust are plotted in Figure 8.26. Although the match between the computed IVR and NVR and those employed for obtaining the measured gross thrust is very good, the computed gross thrust is lower than the measured values. This highlights the importance of the accuracy of the flow rate computation. Earlier in Section 4.4.2 it is shown that shows that a mere 1% under-prediction of the jet velocity results in 4% under-prediction of the gross thrust.

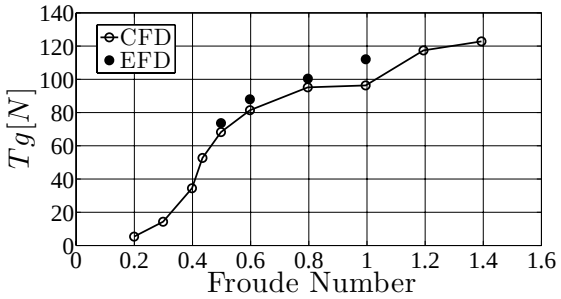

Figure 8.26 Comparison of the computed gross thrust with the measured gross thrust.

Employing the computed gross thrust and the bare hull resistance shown in Figure 8.26 and Figure 6.13, respectively, the thrust deduction fraction of the hull can be calculated from,

$$t = 1 - \frac{R_{bh} - R_a}{T_g}.$$

The rope force, R_a, used to unload the waterjet during the model tests to compensate for the difference between the frictional resistance at the model scale and full scale is obtained from the ITTC-57 formula for the frictional resistance on flat plate (Section 4.3.3). The measured and computed thrust deduction fractions are plotted in Figure 8.27. The computed values are lower than the measured ones in the speed range where the measurements are carried out. The T-junction measurement method is a new and untested technique and the results are strongly dependent on correction for non-orthogonality and nozzle exit pressure. Preliminary computations of the T-junction flow indicated considerably larger corrections for non-orthogonality. This would bring the measured data closer to the computed ones. Further investigations of the T-junction technique are planned. It should be pointed out that accurate measurements of the thrust deduction are very difficult. See Figure 4.31, where the measured thrust deductions for the ATHENA hull in the ITTC campaign varies between $+0.08$ and $+0.16$.

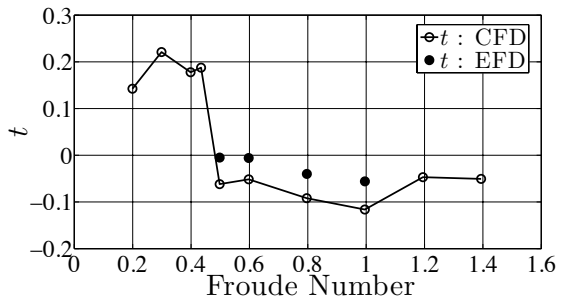

Figure 8.27 Comparison of the measured and the computed thrust deduction fraction.

9 Analysis of the Thrust Deduction

The first objective of this thesis, as specified in Section 2.2, is to explain the physics of the waterjet-hull interaction, in particular the negative thrust deduction observed for many hulls. In the present chapter the details of the interaction will be discussed and the reasons for the large variations of the thrust deduction with Froude number will be explained in the whole Froude number range, from displacement speeds to planing speeds.

The computed thrust deduction fraction, t, is plotted in Figure 9.1 along with the collected thrust deduction fractions obtained through self-propulsion tests at MARIN for a wide variety of hulls with length to beam ratio varying from 3 to 15 (van Terwisga 1996). The trend seen in the computed t is practically the same as in the collected t values. In the lower speed range the thrust deduction fraction has large positive values followed by a rapid drop. After that, it remains almost constant over a range of Froude numbers and then at the higher speed range it starts to increase again.

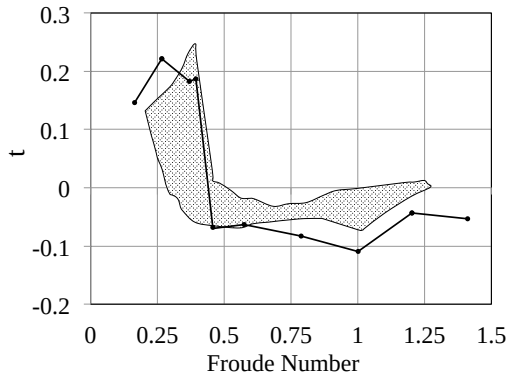

Figure 9.1 Collected thrust deduction fraction (van Terwisga 1996) and the computed thrust deduction fraction (current work, full line).

In order to understand the reason for the diverse trends seen in the thrust deduction fraction curve in different speed ranges it would be less complicated to compare the change in the resistance of the bare hull and the waterjet driven hull directly rather than comparing the bare

hull resistance with the gross thrust of the waterjet system. As introduced in Equation (3-8), the resistance increment fraction, t_r, is defined as follows,

$$t_r = 1 - \frac{R_{bh}}{T_{net}},$$

where T_{net} is equal to the self-propelled hull resistance.

The relation between the total thrust deduction fraction, t, resistance increment fraction, t_r, and jet thrust deduction fraction, t_j, is given in Equation (3-13) and is re-stated in the following,

$$t = t_r + t_j - t_r \cdot t_j.$$

In Figure 9.2 the t and t_r curves are shown. There is a difference between the values of t and t_r but the trends are almost the same, except the Froude number range below the critical Froude number of the waterjet-propelled hull. The present chapter is split into two main parts, first Section 9.1 dealing with t_r and then Section 9.2 concerning t_j. As will be seen, the analysis is very comprehensive, and all contributions to t_r and t_j are discussed in detail.

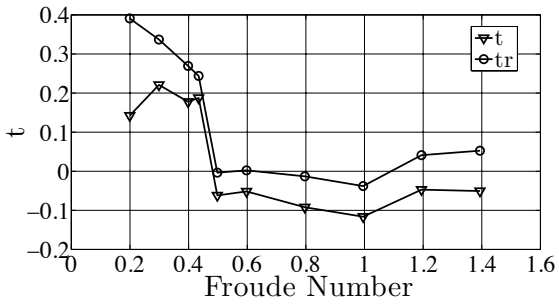

Figure 9.2 Computed thrust deduction fraction, t, and resistance increment fraction, t_r.

9.1 Resistance Increment of the Waterjet-Driven Hull

Like in Chapter 7 the components of the resistance are obtained by splitting the total resistance into the resistance of the transom and the resistance of the rest of the hull, which in the following discussion is mentioned as 'hull'. Then the resistance of the hull and the transom individually are split into the pressure resistance and the frictional resistance, where the pressure resistance in turn is split into the hydrostatic and hydrodynamic resistance. This split was shown as a flowchart in Section 3.9.

For the following discussion three Froude numbers have been selected, each one representing an interesting speed range in Figure 9.2. The Froude numbers are 0.2, 0.8 and 1.4. Complete pressure resistance curves are shown in Appendix D. Results for the three selected Froude numbers are given in Table 9.1, Table 9.3 and Table 9.4. The structure of the tables is presented in connection with Table 6.1.

9.1.1 Lower Speed Range ($0.20 < Fn < 0.50$)

The resistance increment fraction curve can be divided into two distinct regions at the low speed range, which can be recognized based on the slope of the t_r curve shown in Figure 9.2.

In the speed range between Froude number 0.2 and 0.43 the t_r curve slope is negative but is not as steep as the part of the curve between Froude number 0.43 and 0.5. The Froude numbers 0.43 and 0.5 are the transom clearance Froude numbers for the self-propelled hull and the bare hull, respectively. This indicates that the resistance increment is directly associated with the critical Froude numbers of the hulls. The resistance increment in these two regions and the influence of the transom clearance on t_r are discussed in the following.

$0.20 < Fn < 0.43$

The resistance increment fraction has large positive values at this speed range and decreases with Froude number at an almost constant rate until the transom of the waterjet driven hull clears water at Froude number 0.43. The resistance components at Froude number 0.2 are given in Table 9.1.

Table 9.1 Resistance components at $Fn = 0.20$.

		Components			Increments		
		SP	BH	BH_{SP}	SP-BH	BH_{SP} -BH	SP- BH_{SP}
Transom	Hydrostatic	-20.6	-20.7	-21.7	+0.1	-1.0	+1.1
	Hydrodynamic	+3.8	+2.6	+2.7	+1.2	+0.1	+1.1
	Friction	0.0	0.0	0.0	0.0	0.0	0.0
	Total	-16.8	-18.1	-19.0	+1.3	-0.9	+2.2
Hull	Hydrostatic	+22.0	+20.4	+21.5	+1.6	+1.1	+0.5
	Hydrodynamic	+0.8	+0.6	+0.6	+0.2	-0.0	+0.2
	Friction	+2.1	+2.2	+2.2	-0.1	-0.0	-0.1
	Total	+24.9	+23.2	+24.3	+1.7	+1.1	+0.6
Total Resistance	Hydrostatic	+1.4	-0.3	-0.2	+1.7	+0.1	+1.6
	Hydrodynamic	+4.6	+3.2	+3.3	+1.4	+0.1	+1.3
	Friction	+2.1	+2.2	+2.2	-0.1	0.0	-0.1
	Total	+8.1	+5.1	+5.3	+3.0	+0.2	+2.8
			$100\times(\Delta R)/R_{ref}$		+58.8%	+3.8%	+52.8%
			$t_r = \Delta R/R_{final}$		+0.37	+0.04	+0.34

The table rows are divided into three main groups: Transom, Hull and Total, and in each group the three resistance components are presented, together with the total in each group. The columns are split into two main groups: Components and the Increments. It is the increments that are of main interest, and will be discussed below. The notation SP stands for self-propelled hull, BH for bare hull and BH_{SP} for bare hull with the same sinkage and trim as the self-propelled hull. By introducing BH_{SP} the *global effects* (sinkage and trim) can be distinguished from *local effects* caused by the waterjet unit. The increments will now be discussed one by one to explain all contributions to the total sum on the last row, and the t_r computation below the table. Note that all components and increments are positive in the x-direction, i.e. backwards. The resistance increment components due to the global, local and total effects are also presented in a schematic form in Figure 9.3.

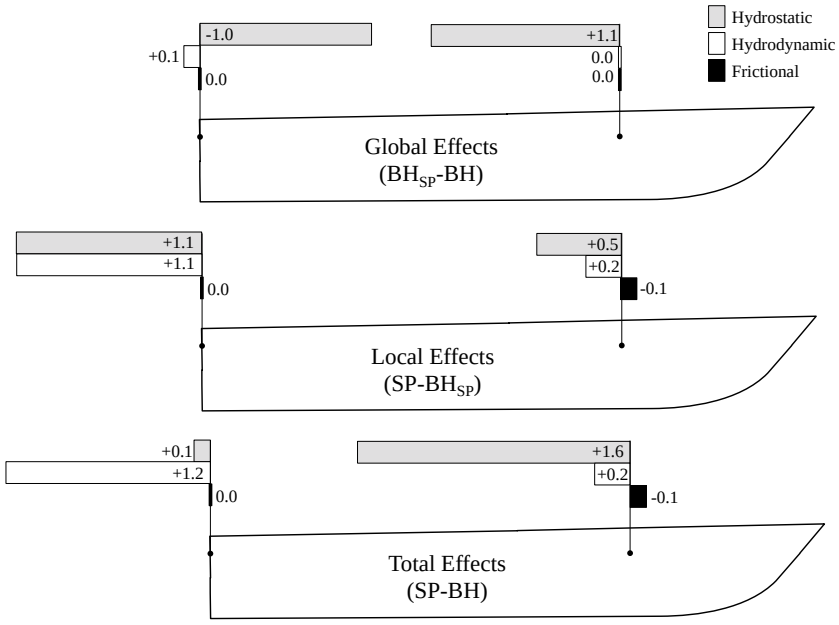

Figure 9.3 Schematic presentation of the hull and the transom resistance increment components at $Fn = 0.20$. The bare hull resistance at this speed is 5.1 N.

Transom Resistance Increment

The total increment of the hydrostatic force on the transom is $+0.1\ N$, a result of a decrease ($-1.0\ N$) due to global effects and an increase ($+1.1\ N$) due to local effects. These effects will now be explained.

The only parameter that influences the hydrostatic force component on the transom, when comparing the bare hulls (BH-BH_{SP}) is the transom submergence. The transom of BH_{SP} is submerged deeper (by almost $2\ mm$[1]) which corresponds to an increase of the transom hydrostatic force component pointing forwards, hence a negative contribution ($-1.0\ N$). Comparing SP and BH_{SP} it is seen that the hydrostatic force component on the SP transom is smaller, i.e. the resistance is changed by $+1.1\ N$. Since SP and BH_{SP} have same sinkage/trim the only cause, which can change the hydrostatic force component on the transom, can be the waterjet system. An obvious reason for the different hydrostatic force component on the transom is the missing area of the nozzle exit, which contributes $+0.8\ N$ out of the total difference, $+1.1\ N$. The remaining $+0.3\ N$ is caused by the lowering of the water height at the transom and results in 4% reduction in the wetted surface area of the transom. The lost area is a strip close to the free-surface and therefore the hydrostatic pressure in this strip is lower than in the rest of the wetted part of the transom.

The increment SP-BH of the hydrodynamic component on the transom ($+1.2\ N$) is almost entirely due to local effects, SP-BH_{sp} ($+1.1\ N$). Global effects, BH_{SP}-BH contribute only $+0.1\ N$. The local effect is due to the jet entrainment. The hydrodynamic pressure coefficient on BH_{SP} and SP as well as the streamlines behind the transoms of these hulls are shown in Figure 9.4 and Figure 9.5, respectively. As seen in Figure 9.5, the discharged jet entrains the

[1] The bare hull aft draft at this speed sinks (moves down wards) by 1.5 mm.

dead water behind the transom. Therefore, the flow at the transom edge bends towards the transom hollow faster to replace the entrained water. The faster turn of the flow means that the curvature of the streamlines tangent to the transom is larger compared to the curvature of the bare hull streamlines, where the jet entrainment effect does not exist. The larger curvature of the streamlines means that the hydrodynamic pressure is lower at the transom edge and thereby also on the entire submerged transom. This is also the reason for the lower water surface.

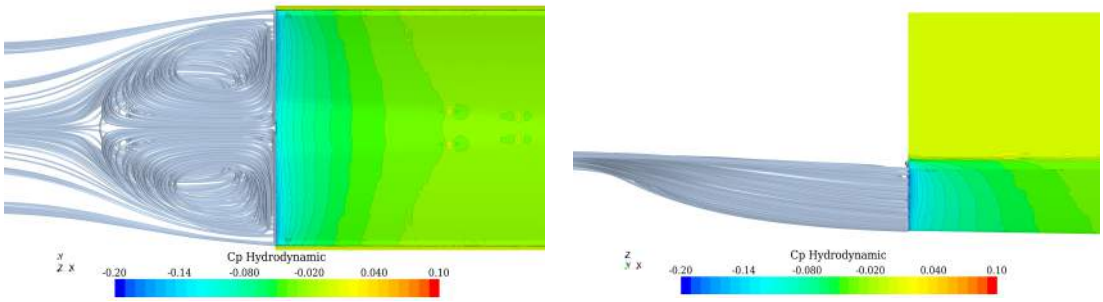

Figure 9.4 Hydrodynamic pressure coefficient contour and streamlines behind the BH_{SP} transom (left: top view and right: side view).

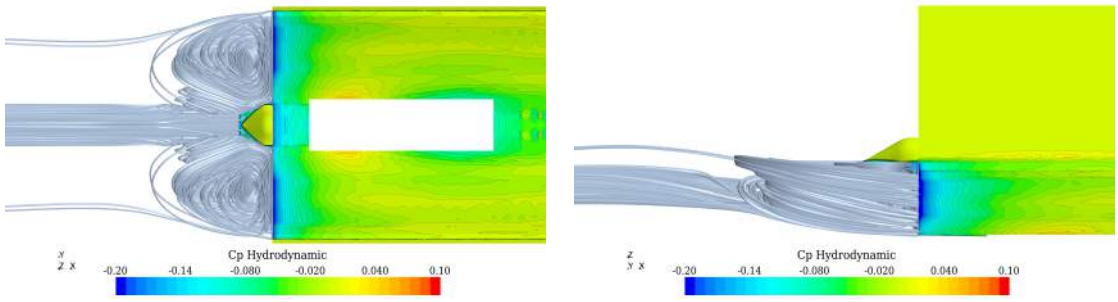

Figure 9.5 Hydrodynamic pressure coefficient contour and streamlines behind the SP transom (left: top view and right: side view).

To further explore the pressure distribution, the hydrodynamic pressure coefficient of BH, BH_{SP} and SP at the transom edge is plotted in Figure 9.6. As seen in this figure, because of the slightly deeper transom submergence of BH_{SP} (almost $2\,mm$), the hydrodynamic Cp at the BH_{SP} transom edge is slightly lower than that of the BH transom, which means that the global effects have small influence on the hydrodynamic resistance change of the transom. But comparing SP and BH_{SP} it is seen that the reduction of the transom edge hydrodynamic pressure due to the local changes caused by the jet entrainment is very large. A prominent bump is seen in the hydrodynamic Cp of the SP transom edge. The reason for this local increase in the hydrodynamic pressure can be related to the recirculating water behind the transom. The streamlines plotted in Figure 9.5 (top view) shows that the recirculating flow hits the transom just on both sides of the nozzle, which results in an increased hydrodynamic pressure around this region. The somewhat irregular distribution of the pressures is due to a very uneven distribution of grid cells close to the transom edge (see also Section 7.3)

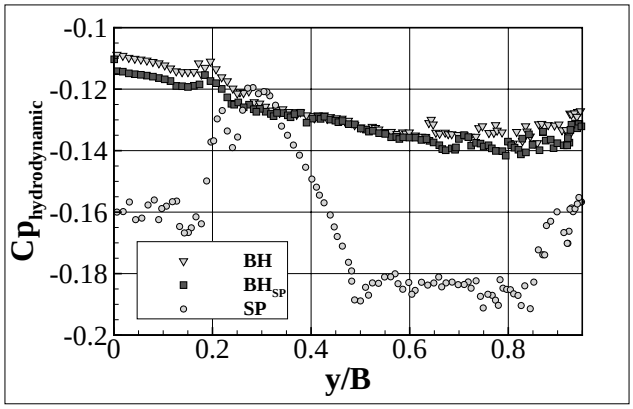

Figure 9.6 Hydrodynamic pressure coefficient across the transom edge for BH, SP and BH_{SP}.

The last transom resistance component shown in Table 9.1 is the frictional resistance. This is zero, since the transom is practically at right angles to the x-axis.

Hull Resistance Increment

The increment in the hydrostatic resistance component of the hull is $+1.6\ N$ between the self-propelled hull and the bare hull. The global effect is largest, $+1.1\ N$, due to increased sinkage ($2\ mm$ at the transom[1]), while $+0.5\ N$ is due to the local changes, mostly caused by the missing surface covering the intake opening. Since the aft part of the bottom at the equilibrium position of Froude number 0.2 has a normal pointing slightly backwards, the hydrostatic pressure acting on this surface will create a net force with a component pointing forward. The hydrostatic pressure coefficient on BH_{SP} is shown in Figure 9.7. Calculation of the hydrostatic force on the intake-opening region (shown in Figure 9.7) confirms that the reason for the different hydrostatic force components on SP compared to BH_{SP} is the missing intake opening area.

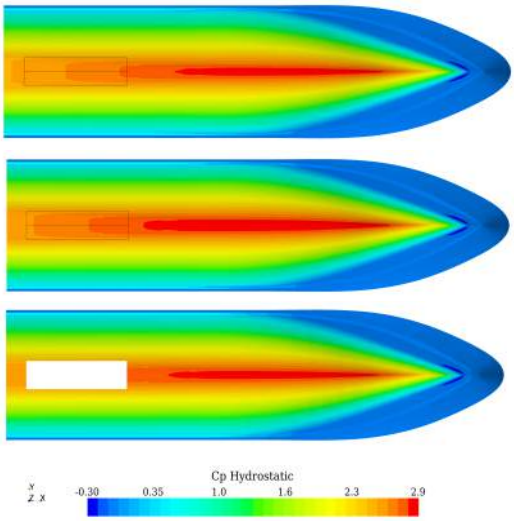

Figure 9.7 Hydrostatic pressure coefficient contour on BH (top), BH_{SP} (middle) and SP (bottom) at $Fn = 0.2$. The bold black line shows the intake-opening region.

[1] The bare hull aft draft at this speed sinks (moves down wards) by 1.5 mm

According to Table 9.1, the hydrodynamic resistance increment of the hull due to global changes is zero. At this speed, the hull sinks by 1.5 mm at mid-ship[1] and the corresponding displacement change is 2%. As a rough estimate, the resistance may be assumed proportional to the displacement. Therefore there would be 2% increase in the hydrodynamic resistance of the hull at this speed, but since the hydrodynamic resistance of the hull is so small from the beginning ($+0.6\ N$), the anticipated 2% increase is negligible.

So at this Froude number, only the local effects contribute to the hydrodynamic resistance increment of the hull ($+0.2\ N$). The computed hydrodynamic force on the intake opening area is negligible and cannot be the reason for the increase in the hydrodynamic resistance of the hull and therefore it is the induced flow by the intake which alters the flow field around the hull and causes a slight change in the hydrodynamic resistance of the hull.

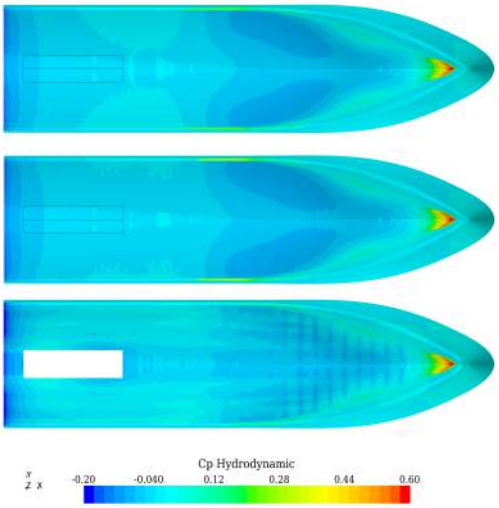

Figure 9.8 Hydrodynamic pressure coefficient contour on BH (top), BH_{SP} (middle) and SP (bottom) at $Fn = 0.2$. The bold black line shows the intake-opening region.

There is a small difference between the SP frictional resistance and that of BH (-0.1 N). As seen in Table 9.1 the reason for the smaller frictional resistance of SP is not global effects but local ones. More specifically, it is the missing area of the intake-opening which results in the smaller frictional resistance of the self-propelled hull.

The last two rows of Table 9.1 indicate the total resistance increment in percent and the total contribution to t_r for all three combinations of hulls, respectively. It is seen that there is 58.8% change in the total resistance of the self-propelled hull compared to the bare hull. There is 52.8% increase due to local effects and only 3.8% due to global effects. The resistance increment fraction t_r is very large: 0.37, of which 0.34 is due to local effects.

$0.43 < Fn < 0.50$

In the speed range to be discussed in this section, t_r drops abruptly from large positive values to values close to zero. In this study it is discovered that the sudden change in the resistance increment curve occurs in the speed range between the critical Froude number of the self-propelled hull and that of the bare hull. In the following, first the possible causes that may

[1] At $Fn = 0.2$ the bare hull sinks (moves down wards) at mid-ship by 1 mm.

result in the earlier transom clearance of the waterjet driven hull are discussed and afterwards the reasons for the sharp drop of the t_r value are explained.

Critical Froude number

Both measurements and computations show that the critical Froude number, where the transom clears water, differs between the towed hull and the waterjet propelled one. Table 9.2 shows the measured and computed critical Froude numbers for both hulls. The critical Froude number is under-predicted in the computations compared to the measured ones, but according to both the measurements and computations the transom of the waterjet driven hull clears earlier than the bare hull. The evolution of the transom wetted surface area for the bare hull and the waterjet-propelled hull is plotted in Figure 9.9.

Table 9.2 Computed and measured critical Froude numbers

	Measured	Computed
Bare Hull	$0.494 < Fn \leq 0.498$	$0.470 < \mathrm{Fn} \leq 0.475$
Self-propelled Hull	$0.430 < Fn \leq 0.434$	$0.415 < \mathrm{Fn} \leq 0.434$

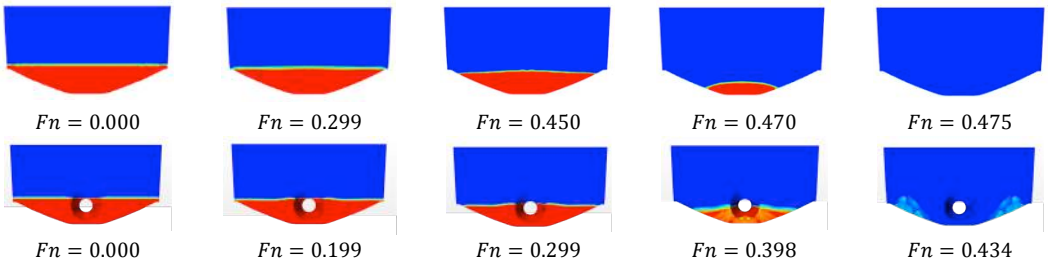

Figure 9.9 Transom wetted surface area of the bare hull (first row) and waterjet driven hull (second row) for various Froude numbers.

The earlier transom clearance of the waterjet-driven hull cannot be due to the draft changes of the self-propelled hull because as shown in Figure 8.9, the aft-draft of the self-propelled hull is larger than that of the bare hull. Deeper transom submergence causes a later transom clearance. So, there must be another reason for the earlier transom clearance for the waterjet-propelled hull.

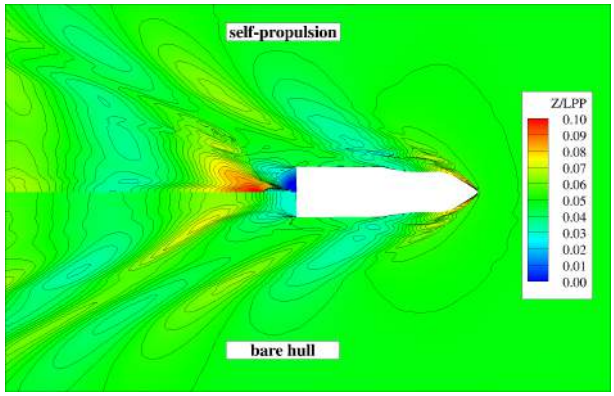

Figure 9.10 Wave pattern around the bare hull (lower half) and waterjet-driven hull (upper half). The bare hull sinkage and trim are fixed to the measured sinkage and trim of the self-propelled hull at $Fn = 0.434$.

In order to eliminate the sinkage and trim effects on the transom clearance of the self-propelled hull, some simulations are carried out with the sinkage and trim of the bare hull set equal to the ones of the self-propelled hull. Figure 9.10 shows the contour plot of the wave height at $Fn = 0.434$ at the same sinkage and trim for the bare hull and waterjet propelled hull. The wave patterns of these two cases are very different behind the transom. The aft-part streamlines on the symmetry plane can be compared in Figure 9.11. Despite the equal sinkage and trim for both cases, the bare hull transom is still wet and transom of the self-propelled is dry. A recirculating zone is noted behind the transom of the bare hull, whereas no such recirculating zone can be observed in the self-propelled case. This is likely to be an effect of the high momentum jet flow which pushes the dead-water flow behind the transom downstream and eliminates the breaking waves filling the hollow behind the transom at Froude numbers just below the critical one.

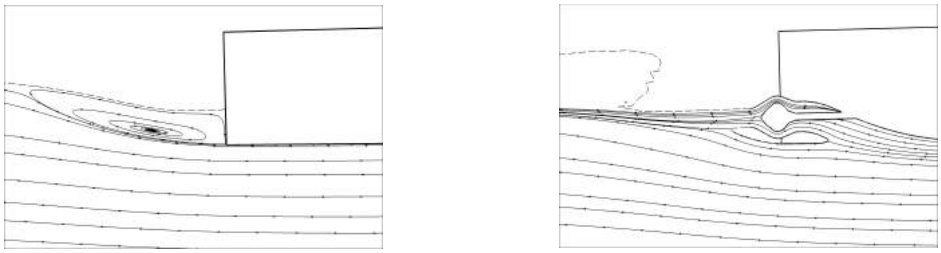

Figure 9.11 Flow pattern in the aft of the bare hull (left) and waterjet driven hull (right) on the symmetry plane. The dashed line shows the free-surface and the full lines show the. The bare hull sinkage and trim are fixed to the measured sinkage and trim of the self-propelled hull at $Fn = 0.434$.

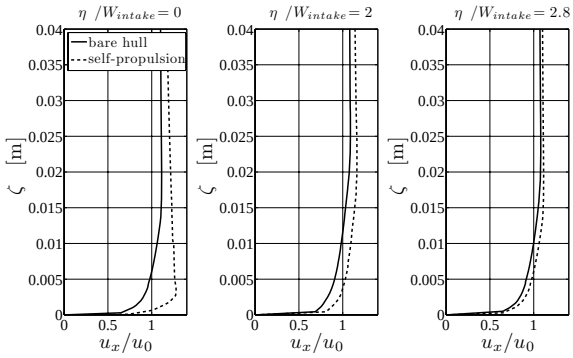

Figure 9.12 Axial velocity variations on three vertical lines with different transverse distance from the symmetry plane of the hull at the transom edge at $Fn = 0.434$. ξ and η are the vertical distance from the transom edge and transverse distance from the symmetry plane of the hull, respectively.

Additionally, low momentum boundary layer flow is sucked into the waterjet unit and then expelled out far beyond the transom. Figure 9.12 shows the axial velocity at the transom edge on three vertical lines positioned in different transverse distances from the hull symmetry plane for both the bare hull and the waterjet driven hull. The axial velocity at the transom edge is larger for the waterjet driven hull compared to the towed hull. The largest difference between the towed hull and the self-propelled hull is seen at the transom centreline and then the deviation becomes smaller at the sections farther from the centreline. This means that the flow leaving the waterjet propelled hull transom edge has a higher momentum and therefore the stern wave is less prone to breaking.

A third effect may be envisaged considering Figure 9.13, which compares the wave cut at $y/Lpp = 0.243$ for the bare hull and self propelled hull with the same sinkage and trim at the same Froude number. Due to the suction of the waterjet unit the wave height is lowered on the sides of the hull in the aft-part (almost starting from the capture area section, $x/Lpp = 0.71$) and therefore the flow, which could fill in the hollow behind the transom from the sides, is removed.

All these three effects result in an earlier transom clearance of the waterjet-driven hull in comparison to the bare hull. The effect of the different critical Froude numbers on the resistance increment is discussed in the following section.

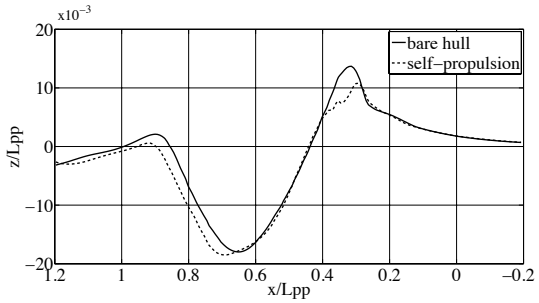

Figure 9.13 Wave cuts at $y/Lpp = 0.243$ for the bare hull and self-propelled hull at $Fn = 0.434$. The bare hull sinkage and trim are fixed to the measured sinkage and trim of the self-propelled hull. The coordinate system has its origin at the zero speed bow waterline, x points backwards, y to starboard and z vertically upwards. The transom is located at $x/Lpp = 1$ and the capture area is located at $x/Lpp = 0.71$.

Abrupt Drop in t_r

As discussed in Chapter 7 there is an abrupt peak in the resistance coefficient of the bare hull at the critical Froude number. This is the case also for the self-propelled hull, as appears from Figure 9.14. Since the self-propelled hull has a lower critical Froude number the peak is shifted to the left. It is this shift that causes the rapid drop in t_r.

Replacing resistance by C_T in Equation (3-8) yields,

$$t_r = 1 - \frac{C_{T_{bh}}}{C_{T_{sp}}}.$$

Employing this equation in combination with the data given in Figure 9.14, it is it is seen that t_r is large and positive at the critical Froude number of the self-propelled hull thereafter dropping to zero at the Froude number where the two curves meet. This explains the abrupt drop in the resistance increment fraction curve of Figure 9.2.

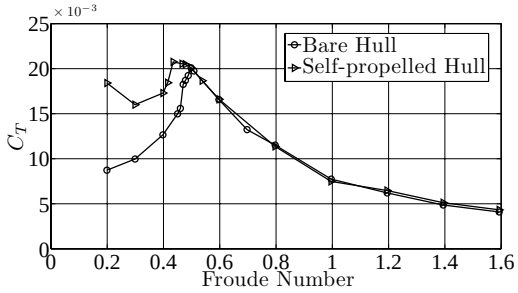

Figure 9.14 Resistance coefficients of the bare hull and the self-propelled hull.

9.1.2 Intermediate Speed Range ($0.50 < Fn < 1.00$)

As seen in Figure 9.2, the resistance increment fraction is close to zero in the intermediate speed range, $0.5 < Fn < 1.0$. The speed in this range is beyond the critical Froude numbers of the bare hull and self-propelled hull and therefore there is no hydrostatic or hydrodynamic force acting on the transom and it is the change of forces acting on the hull that contribute to the resistance increment. The resistance increment components due to the global, local and total effects are also presented schematically in Figure 9.15. In the following, the resistance increment components of the hull are analysed in the same way as for the lower speed range.

Table 9.3 Resistance components of hulls $Fn = 0.80$.

		Components			Increments		
		SP	BH	BH_{SP}	SP-BH	BH_{SP} -BH	SP- BH_{SP}
Transom	Hydrostatic	0	0	0	0	0	0
	Hydrodynamic	0	0	0	0	0	0
	Friction	0	0	0	0	0	0
	Total	0	0	0	0	0	0
Hull	Hydrostatic	+18.0	+25.3	+23.1	-7.3	-2.2	-5.1
	Hydrodynamic	+63.8	+57.1	+64.9	+6.7	+7.8	-1.1
	Friction	+27.4	+28.0	+28.6	-0.6	+0.6	-1.2
	Total	+109.2	+110.4	+116.6	+1.7	+6.2	-7.4
Total Resistance	Hydrostatic	+18.0	+25.3	+23.1	-7.3	-2.2	-5.1
	Hydrodynamic	+63.8	+57.1	+64.9	+6.7	+7.8	-1.1
	Friction	+27.4	+28.0	+28.6	-0.6	+0.6	-1.2
	Total	+109.2	+110.4	+116.6	-1.2	+6.2	-7.4
				$100\times(\Delta R)/R_{ref}$	-1.1%	+5.3%	-6.3%
				$t_r = \Delta R/R_{final}$	-0.01	+0.06	-0.07

Comparing the self-propelled hull resistance with that of the bare hull, it is seen that the total resistance of the hull changes by $-7.3\ N$ due to the change in the hydrostatic resistance of the hull. The global effect contribution to the hydrostatic pressure resistance increment of the hull is $-2.2\ N$. Although BH_{SP} sinks deeper compared to BH ($6\ mm$ at mid-ship[1]) its smaller trim angle (0.2° less) positions the hull such that the hydrostatic pressure on the fore part cancels to a larger extent the hydrostatic pressure on the aft part of the hull. This is the reason for the reduced hydrostatic pressure resistance due to the global effects. The local effects also cause a reduction ($-5.1\ N$) in the hydrostatic pressure resistance of the hull. The major part of this reduction ($-4.9\ N$) is caused by the missing intake opening area. At Froude number 0.8, the trim angle of the hull (~3.8°) positions the intake-opening surface such that the hydrostatic force acting on this surface has an axial component pointing backward.

[1] The bare hull moves upwards by almost $25\ mm$ at mid-ship at $Fn = 0.8$ (Figure 8.10).

Removing this surface will result in a decreased hydrostatic resistance of SP. The rest of the hydrostatic pressure resistance increment due to the local effect ($-0.2\ N$) is caused by the intake-induced flow, which alters the waves close to the aft part of the hull.

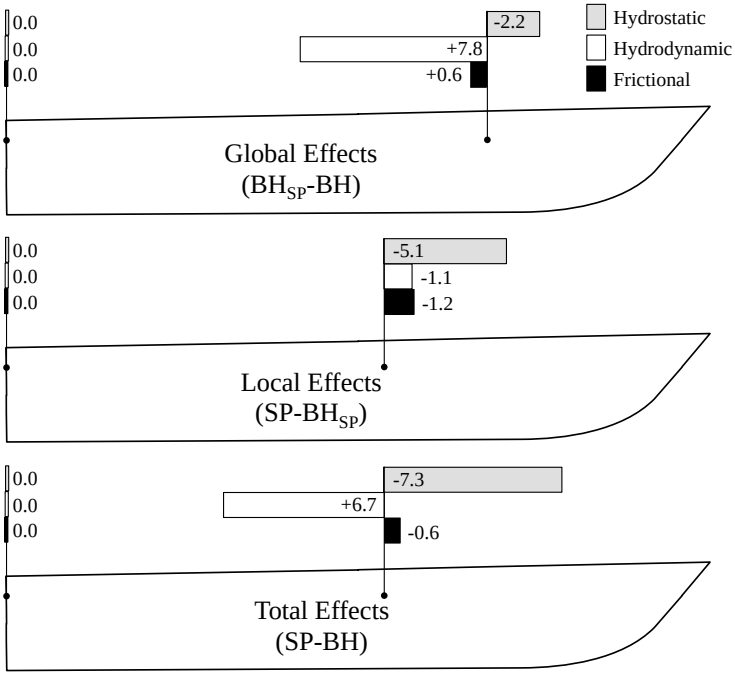

Figure 9.15 Schematic presentation of the hull and the transom resistance increment components at $Fn = 0.80$. The bare hull resistance at this speed is 110.4 N.

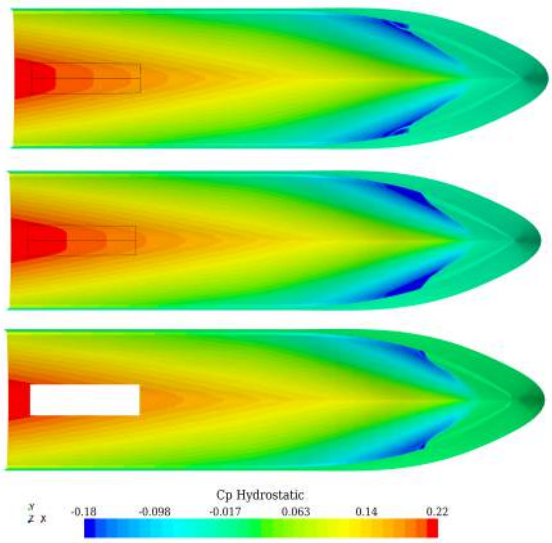

Figure 9.16 Hydrostatic pressure coefficient contour on BH (top), BH_{SP} (middle) and SP (bottom) at $Fn = 0.8$. The bold black line shows the intake-opening region.

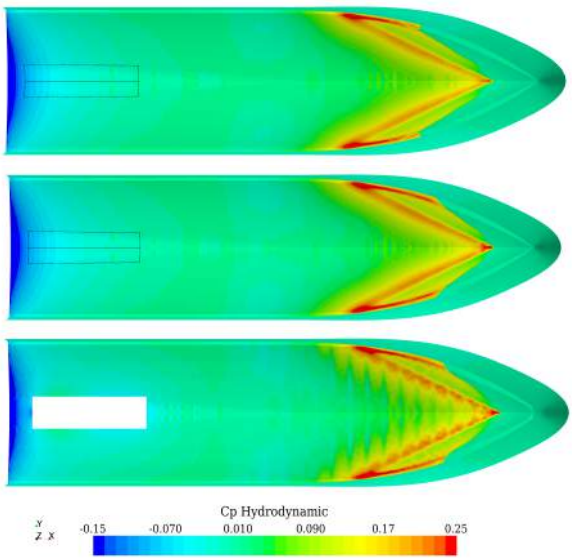

Figure 9.17 Hydrodynamic pressure coefficient contour on BH (top), BH_{SP} (middle) and SP (bottom) at $Fn = 0.8$. The bold black line shows the intake-opening region.

The hydrodynamic pressure resistance of SP is $+6.7\,N$ larger than that of BH. The hydrodynamic pressure resistance increment due to the global effects is $+7.8\,N$. The local effects contribution to the hydrodynamic pressure resistance increment works in the opposite direction and changes the resistance by $-1.1\,N$. The reason for the resistance increase due to the global effects is the deeper sinkage ($6\,mm$ at mid-ship), which gives an increased displacement and thereby a higher hydrodynamic pressure on the bottom (Figure 9.17). The reason for the resistance reduction due to the local effects is the missing intake surface. As stated in the discussion of the hydrostatic pressure resistance of the hull, the intake-opening surface is inclined such that its normal vector has a component which points to the forward direction.

Comparing BH_{SP} and BH, it is seen that the increased sinkage and decreased trim angle result in increased wetted surface area of the hull and therefore the frictional resistance of BH_{SP} increases ($+0.6\,N$) but comparing SP and BH_{SP} the frictional resistance is seen to decrease due to the missing surface of the intake-opening ($-1.2\,N$). The result of these two effects is a frictional resistance change of $-0.6\,N$.

At this operating Froude number, the hull hydrostatic, hydrodynamic and frictional resistances vary such that the sum of all these variations becomes almost zero, and that is the reason for obtaining almost zero resistance increment fraction in the intermediate operating speed range.

9.1.3 High Speed Range ($1.0 < Fn < 1.4$)

The resistance increment fraction gradually increases and has positive values in this speed range (Figure 9.2). The resistance increment components of the hull at $Fn = 0.8$ is shown in Table 9.4. Moreover, the resistance increment components due to the global, local and total effects are also presented schematically in Figure 9.18. Each of these resistance increment components is discussed in the following.

Table 9.4 Resistance components of hulls $Fn = 1.4$.

		Components			Increments		
		SP	BH	BH_{SP}	SP-BH	BH_{SP} -BH	SP- BH_{SP}
Transom	Hydrostatic	0	0	0	0	0	0
	Hydrodynamic	0	0	0	0	0	0
	Friction	0	0	0	0	0	0
	Total	0	0	0	0	0	0
Hull	Hydrostatic	+8.3	+12.5	+13.3	-4.2	+0.8	-5.0
	Hydrodynamic	+74.7	+61.8	+76.7	+12.9	+14.9	-2.0
	Friction	+65.2	+67.2	+69.5	-2.0	+2.3	-4.3
	Total	+148.2	+141.5	+159.5	+6.7	+18.0	-11.3
Total Resistance	Hydrostatic	+8.3	+12.5	+13.3	-4.2	+0.8	-5.0
	Hydrodynamic	+74.7	+61.8	+76.7	+12.9	+14.9	-2.0
	Friction	+65.2	+67.2	+69.5	-2.0	+2.3	-4.3
	Total	+148.2	+141.5	+159.5	+6.7	+18.0	-11.3
				$100\times(\Delta R)/R_{ref}$	+4.7%	+12.7%	-7.0%
				$t_r = \Delta R/R_{final}$	+0.04	+0.11	-0.07

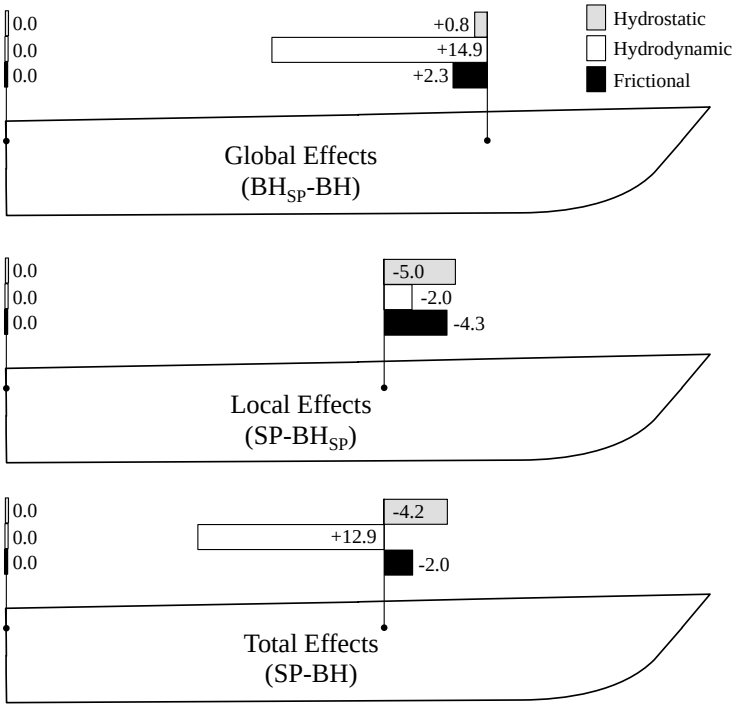

Figure 9.18 Schematic presentation of the hull and the transom resistance increment components at $Fn = 1.4$. The bare hull resistance at this speed is $141.5\ N$.

The total hydrostatic pressure resistance increment of the hull at this speed is $-4.2\ N$. The global effects changes the hydrostatic pressure resistance by $+0.8\ N$ whereas the local effect contribution to the hydrostatic pressure resistance increment is much larger and is in the opposite direction ($-5.0\ N$). The sinkage of BH_{SP} is larger compared to BH ($11\ mm$ deeper at mid-ship[1]) and due to the bow down trimming moment of the waterjet the hull trims less (0.2°). The combination of these two effects result in an increased hydrostatic pressure on the aft part of the hull (see Figure 9.19). Due to the trim angle of BH_{SP} at this speed (~3.9°), the x-component of the surface normal points forwards and therefore the resultant force caused by the increased hydrostatic pressure on the aft part will point backwards. This is the reason for the slight increase of the hull resistance due to the global effects ($+0.8\ N$). Removing the

[1] The bare hull moves upwards by $68\ mm$ at mid-ship at $Fn = 1.4$ (Figure 8.10).

contribution of the hydrostatic pressure force acting on the intake-opening will decrease the resistance. This is the reason for the negative hydrostatic pressure resistance increment at this speed ($-5.0\ N$).

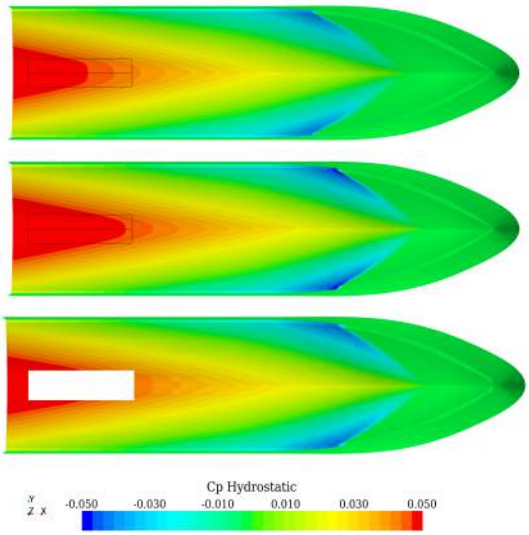

Figure 9.19 Hydrostatic pressure coefficient contour on BH (top), BH_{SP} (middle) and SP (bottom) at $Fn = 1.4$. The bold black line shows the intake-opening region.

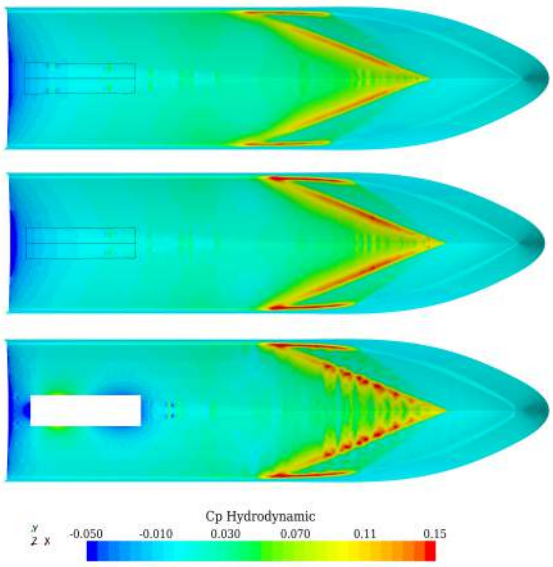

Figure 9.20 Hydrostatic pressure coefficient contour on BH (top), BH_{SP} (middle) and SP (bottom) at $Fn = 1.4$. The bold black line shows the intake-opening region.

The total resistance of the hull changes by $+12.9\ N$ due to the hydrodynamic pressure resistance change, which occurs between SP and BH. In fact the contribution of the global effects to the hydrodynamic resistance increment is larger than this value ($+14.9\ N$) but the local effect changes the resistance by $-2.0\ N$. As stated in the previous paragraph, BH_{SP} sinkage is larger compared to BH which increases the displacement. The increased hydrodynamic pressure resistance due to the global effects is a result of the increased displacement. The hydrodynamic pressure coefficient on BH and BH_{SP} are shown in Figure

9.24. It is seen that, due to the larger displacement of BH_{SP}, the hydrodynamic pressure on the fore part of the hull, especially where the free-surface hits the hull, has increased. A study of the local effects on the resistance increment shows that only a trivial proportion of the total reduction of the hydrodynamic pressure resistance by the local effects is caused due to the missing intake-opening area ($-0.1\ N$ out of $-2.0\ N$). This means that the local effects alter the hydrodynamic pressure resistance of the hull mainly through the intake-induced flow, which changes the waves around the hull. The altered pressure distribution around the intake opening on SP is noticeable comparing to BH_{SP} (Figure 9.24).

The wetted surface area of the BH_{SP} increases by almost 5.9% because of the changed sinkage and trim of the hull. This results in $+2.3\ N$ increase in the frictional resistance of the hull but on the other hand the missing intake-opening surface causes a decrease in the wetted surface area of the hull by 6.3% resulting in $-4.3\ N$ decrease in the frictional resistance of the hull. The resultant of these two effects is a total frictional resistance change of $-2.0\ N$.

9.1.4 Separation at the Lip

Having explained the different contributions to the resistance increment fraction a short note on the flow around the lip will be made. A possible reason for the increased thrust deduction fraction at higher Froude numbers could be a separation occurring at the lip, which could result in an increased resistance of the hull. Figure 9.21 shows the streamlines around the waterjet intake lip at different operating speeds. One of the streamlines which hits the lip is the separating streamline, which shows the location of the stagnation point on the lip. Moreover, this specific streamline shows the streamtube profile in the symmetry plane. As seen in Figure 9.21 the shape of the streamtube, as well as the angle, at which it approaches the stagnation point, varies at different speed. At the lower speed ($Fn = 0.199$) the streamline approaches the stagnation point from the bottom, while at the higher speed ($Fn = 1.394$) it approaches the stagnation point from the above. The coordinate of the stagnation point also varies with speed. As the speed increases the stagnation point moves slightly inside the intake channel. If the stagnation point completely moved inside the ducting channel, there would be a risk of separation on the lower part of the lip. For the studied waterjet unit, the stagnation point stays close to the outer part of the lip, and therefore no separation sign could be detected at any of the operating speeds Thus, for the present hull, separation at the lip cannot be the cause of the increased resistance increment at the higher speed ranges.

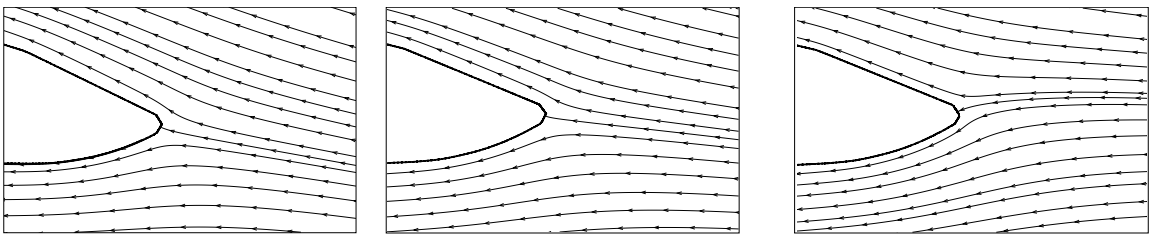

$Fn = 0.199$ $Fn = 0.797$ $Fn = 1.394$

Figure 9.21 Streamlines around the lip at different speeds. The black full line shows the lip geometry on symmetry plan.

9.2 Relation Between the Net Thrust and the Gross Thrust

In Chapter 9 it was shown that the net thrust (resistance of the self-propelled hull) defines the trend of the thrust deduction fraction and that the gross thrust, to a large extent, follows the trend given by the resistance changes of the self-propelled hull. According to Chapter 3, Equation (3-9), the difference between the gross thrust and the net thrust is the sum of the intake and the exit drag,

$$T_g - T_{net} = -\iint\limits_{A_1+A_2+A_8} \sigma_x dA + \iint\limits_{A_4} \sigma_x dA = D_i + D_e. \qquad (9\text{-}1)$$

The intake drag is the resultant of the forces acting on the capture area (A_1), the streamtube which is part of the control volume for determining gross thrust (A_2), and the part of the ducting channel that is outside the stream tube (A_4). The exit drag is the force acting on the nozzle exit area (A_4). In the following, only pressure forces will be considered, since the contributions from friction are very small.

So far it has been assumed that the stator removes the entire swirl caused by the impeller, and therefore the jet is swirl free. However, in off design operating conditions of the waterjet pump the jet might not be entirely swirl free. The swirl at the nozzle exit results in a reduced pressure which changes the exit drag. There might also be an effect on the flow rate and consequently the gross thrust of the waterjet system. The effect of swirl is discussed at the end of this section.

9.2.1 Intake Drag

The intake drag caused by the pressure force acting on surfaces A_1, A_2 and A_4 (Figure 9.22) is split into hydrostatic and the hydrodynamic components to track the source of the drag more in detail. The hydrostatic and hydrodynamic pressure distributions on A_1, A_2 and A_4 at $Fn = 0.8$ are shown in Figure 9.23 and Figure 9.24, respectively. Contributions to D_i from A_1, A_2 and A_4 at different Froude numbers are shown in Figure 9.25. Note that a positive contribution is obtained for a force in the negative x-direction for A_1 and A_2, but in the positive direction for A_4. The hydrostatic pressure force component is larger than the hydrodynamic force exerted on these surfaces. Since the projected area of A_1 and A_2 on the yz-plane is much larger than that of A_4, these two surfaces have the largest hydrostatic pressure force components but since the normal vectors to these surfaces have their longitudinal components in opposite directions, these two large hydrostatic force components have different signs and cancel each other to a large extent. The hydrostatic pressure force on A_1 and A_2 are largest in the lower Froude number range because of the deeper submergence of the hull in this speed range (Figure 8.9). There is also a larger capture area and projection of the stream tube on yz-plane. The variation of the capture area with speed was shown earlier in Figure 8.19.

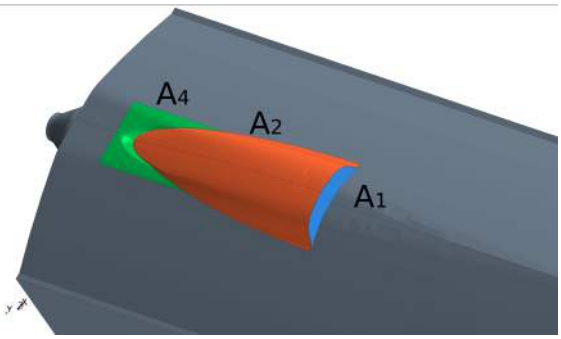

Figure 9.22 Computed A_1, A_2 and A_4.

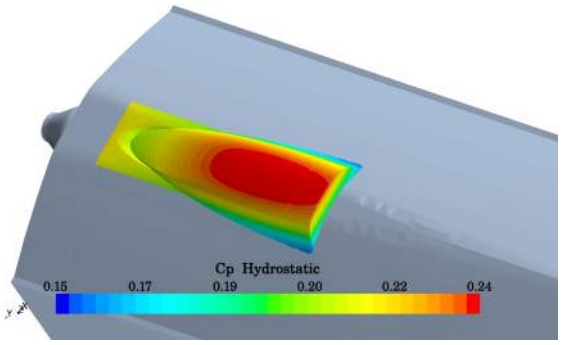

Figure 9.23 Hydrostatic pressure coefficient on the capture area, the streamtube and A_4 at Froude number 0.8 (bottom view)

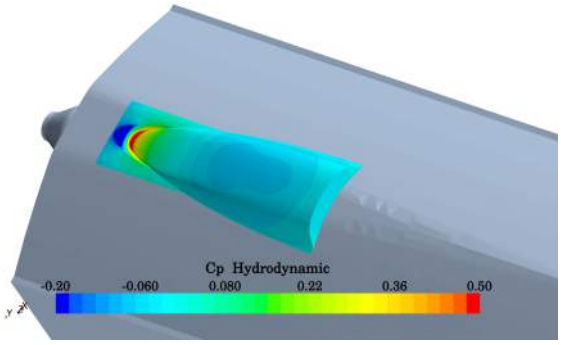

Figure 9.24 Hydrodynamic pressure coefficient on the capture area, the streamtube and A_4 at Froude number 0.8 (bottom view)

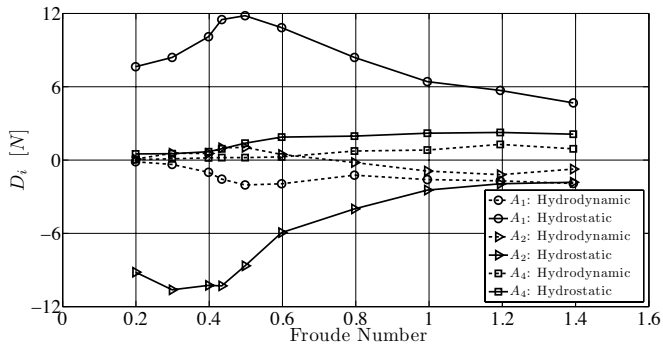

Figure 9.25 Hydrostatic and hydrodynamic pressure contributions to the intake drag

9.2.2 Exit Drag

The exit drag is caused by non-atmospheric pressure on the jet exit. In the literature ((van Terwisga 1996; ITTC 2005d)) this component is assumed significant only if the exit is submerged. However, even if the jet is ejected into the air, the pressure will be non-atmospheric, unless the streamlines leaving the nozzle are exactly parallel. This is unlikely to be the case for most nozzles, and for the SSPA hull (Figure 8.1) a relatively large pressure is found in the jet centre. The pressure distribution is shown in Figure 9.26. Integrating this pressure over the nozzle exit area the exit drag is obtained.

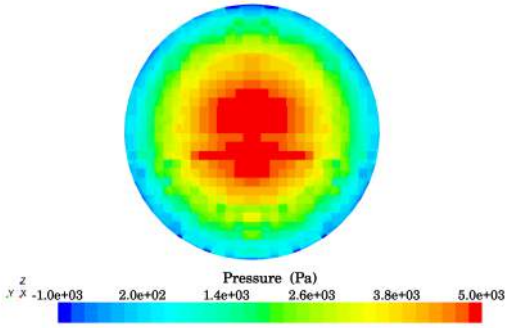

Figure 9.26 Total pressure distribution at the nozzle exit section at $Fn = 0.5$.

Figure 9.27 shows the intake and exit drag versus Froude number. Except at low speed the intake drag is positive, while the exit drag is negative in the entire speed range. In the major part of the speed range the exit drag magnitude is larger than the magnitude of the intake drag, so the largest contribution to the difference between the gross and net thrust is the exit drag. The exit drag magnitude increases more or less linearly with speed but the intake drag magnitude increases first and then starts to decrease slightly in the Froude number range $0.6 < Fn < 1.4$. The magnitude of the sum of the two components has a peak at the clearance Froude number, but increases monotonously above $Fn = 0.5$.

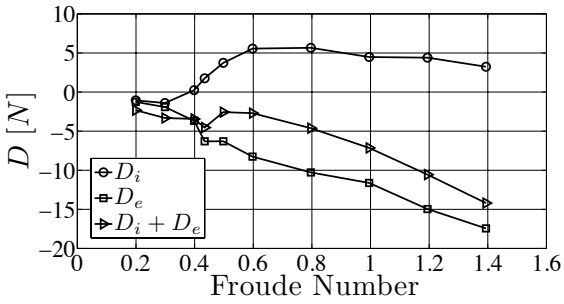

Figure 9.27 Intake and exit drag

9.2.3 Jet Thrust Deduction Faction

According to Equation (9-1), the sum of the intake and exit drag is equal to the difference between the gross and net thrust. In practice there will be a difference due to the limited numerical accuracy. The thrust difference is computed from two large numbers: the gross thrust obtained from the momentum balance, and the resistance of the hull in self-propulsion. These numbers are of the same order of magnitude, while the difference is one order smaller. The intake and exit drags are obtained from forces acting on small areas of the total system.

In Figure 9.28 the difference between the thrusts is compared with the sum of the intake and exit drag. Considering the numerical accuracy the correspondence is very good.

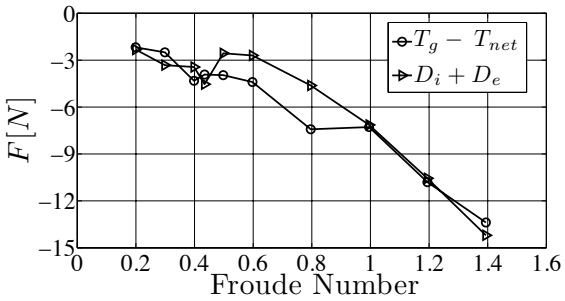

Figure 9.28 Comparison of the difference between the gross thrust and the net thrust with the sum of the intake and the exit drag

The jet thrust deduction fraction, t_j, is obtained from the difference between the gross and net thrust divided by the gross thrust (implicit formula),

$$t_j = \frac{T_g - T_{net}}{T_g}. \qquad (9\text{-}2)$$

It can also be obtained from the sum of the intake and exit drag (explicit formula),

$$t_j = \frac{D_i + D_e}{T_g}. \qquad (9\text{-}3)$$

In Figure 9.29, t_j computed by both methods is presented. According to this figure, the jet thrust deduction fraction magnitude is largest at very low speeds but deceases very fast as the Froude number increases. The smallest magnitude of t_j occurs around Froude number 0.5, which is the transom clearance Froude number of the bare hull. After this speed the t_j magnitude increases slightly.

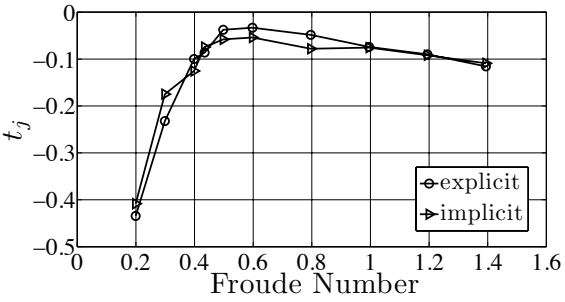

Figure 9.29 Jet thrust deduction fraction

As discussed in Section 3.3 the total thrust deduction fraction can be obtained in two different ways. The first way is using the definition of the thrust deduction fraction (Equation (3-7)) directly and the second way is to add the components of the thrust deduction fraction (Equation (3-13)), which is an indirect method. The equations used in the direct and the indirect methods are re-stated in the following.

direct: $$t = 1 - \frac{R_{bh}}{T_g}$$

indirect: $$t = t_r + t_j - t_r \cdot t_j$$

Figure 9.30 shows the thrust deduction fraction computed from the two different methods. The agreement between these two methods at different Froude numbers is good. These results also show that at the speeds above the critical Froude number of the waterjet-propelled hull the second order term in the thrust deduction fraction equation (indirect) is negligible but it cannot be neglected at the lower speed range where both t_r and t_j are large (Figure 9.2 and Figure 9.29).

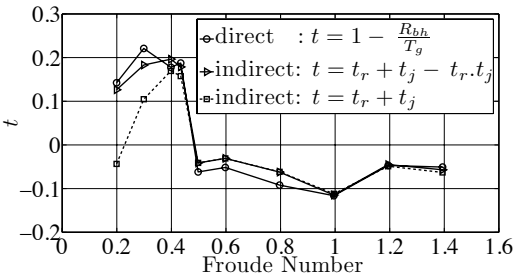

Figure 9.30 Thrust deduction fraction computed from two different methods

Jet Swirl Effects

The effect of swirl is discussed by the 21st ITTC (ITTC 1996b) but there is no information given about swirl levels in existing waterjet systems. There is in fact very little information about swirl available in the literature. Two reports which do include such information are however those of Rispin (2005) and Jonsson (1996). The tangential component of the nozzle exit velocity is very dependent on the operating condition of the pump. Rispin (2005) shows that at the lower flow rates, where the pump and the stator are at off-design conditions, some swirl is left in the nozzle exit flow, while close to the design flow rate the tangential velocity of the jet is nearly removed which indicates that the stator performs its task very well. According to the measurements presented in this report, the average tangential velocity over the nozzle exit section varies between 4 and 17% of the average axial velocity at different operating conditions. Observing the angle of some strings placed at different radii of the nozzle exit at different pump operating conditions, Jonsson (1996) indicates that the ratio of the tangential velocity to the axial velocity at the nozzle exit is at most 17%, where measurements were possible. The swirl is maximum at the jet centre due to a centre vortex created by the hub, but neither in (2005) nor in (1996) the swirl at the centre is reported. The reasons are that in the study carried out by Rispin, the hub was extended to accommodate the water-tunnel rear drive shaft arrangement, so there was no centre vortex started at the nozzle exit, and in the investigating done by Jonsson the rotation was so high at the centre that is was impossible to measure any reliable angle for the visualizing string. But since the area close to the centre is so small, the strong swirl in this region does not significantly affect the area weighted average of the swirl over the entire nozzle exit area.

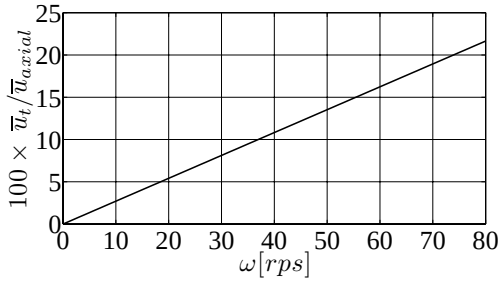

Figure 9.31 The ratio of the area weighted average tangential velocity to the area-weighted average of the axial velocity as a function of the angular velocity (Solid body rotation).

The ratio of the area-weighted average of the tangential velocity to the average axial velocity of the jet as a function of the angular velocity is plotted in Figure 9.31. To obtain this curve, it is assumed that the jet rotates like a solid body meaning that the tangential velocity increases linearly between the centre and the outermost radius, which is assumed to be the same as the radius of the nozzle exit used in this study ($R = 28.2\ mm$). The average axial velocity of the jet is assumed to be the one obtained at $Fn = 0.5$. The reason for choosing this Froude number is the fact that the waterjet pump should be working in an off design condition at this speed and the swirl should be the largest. As seen in Figure 9.31 the ratio of the area weighted average tangential velocity to the average axial velocity increases linearly as the angular velocity of the jet increases. According to (Rispin 2005) and (Jonsson 1996) the maximum inclination angle of the jet outgoing velocity vector with respect to the axial direction is about 10°, which indicates that the maximum tangential velocity is about 17% of the axial velocity. This ratio corresponds to $\omega = 60$ in Figure 9.31.

As shown in Section 3.6.1 the pressure reduction at a radius r in the nozzle exit due to the jet swirl can be obtained from Equation (3-19).

$$\Delta p_{swirl}(r) = -\rho . \int_0^r \frac{u_{\phi 8}^2}{r} dr \qquad (3\text{-}19)$$

where $u_{\phi 8}$ is the tangential velocity of the jet and r is the radial distance from the jet center.

Assuming solid body rotation, the tangential velocity of the jet can be written as follows,

$$u_{\phi 8} = r \cdot \omega, \qquad (9\text{-}4)$$

where ω is the angular velocity.

Inserting Equation (9-4) into Equation (3-19) and carrying out the integration the pressure reduction due to swirl is,

$$\Delta p_{swirl}(r) = -\rho . \frac{u_{\phi 8}^2}{2} \qquad (9\text{-}5)$$

This formula yields the pressure correction at each radius. However, the pressure will be atmospheric at the outer surface of the jet regardless of the swirl and therefore no pressure correction shall be imposed at this radial distance from the jet centre. In order to satisfy this

boundary condition, the pressure correction obtained at the jet outer edge is subtracted from all the pressure corrections at the different radii. After doing so, the pressure gradient from the jet centre outwards is correct and the atmospheric boundary condition is satisfied on the jet outer edge.

Integrating the pressure gradient at different radii over discretized circumferential strips will give the change in the pressure force exerted on the nozzle exit due to the swirl. The ratio of this force, ΔF_ω, to the original pressure force exerted on the nozzle exit, F_0, in the absence of swirl as a function of the angular velocity of the jet is plotted in Figure 9.32. In Figure 9.31 it is shown that the rotational velocity of $60\,rps$ corresponds to $10°$ of the jet inclination. According to Figure 9.32, the corresponding pressure force reduction acting on the nozzle exit at the angular velocity of $60\,rps$ is 23% smaller than the pressure force without swirl.

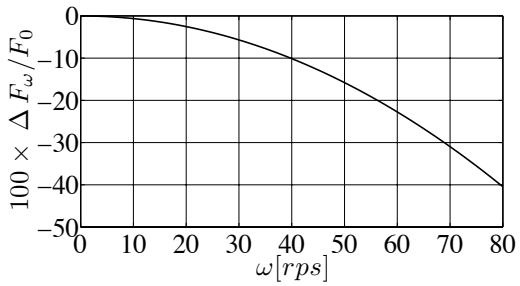

Figure 9.32 The ratio of the change in the pressure force exerted on the nozzle exit due to swirl, ΔF_ω, to the pressure force without swirl, F_0, as a function of the angular velocity.

An alternative evaluation of the swirl effect on the pressure force acting on the nozzle exit is accomplished by adding tangential components to the body force applied to the impeller region in the numerical simulation of the flow around the waterjet propelled hull. Since after the introduction of the tangential component for the body force, the flow is no more symmetric, and it is needed to solve for the entire flow field without any symmetry boundary condition. It is assumed that the tangential component of the body force is equally distributed in the radial direction inside the volume containing the impeller. The relation between the tangential component of the body force and the jet swirl at the nozzle exit is not known from the beginning so it is required to try out some different tangential body force magnitudes in order to obtain the desired swirl at the nozzle exit. Based on the measured swirl angle in (Rispin 2005) and (Jonsson 1996) the tangential component of the body force is specified so as to obtain $10°$ of area weighted average swirl at the nozzle exit. According to the mentioned references, $10°$ swirl is the maximum measured for the studied waterjet pumps and therefore the pressure difference obtained based on such a swirling flow should be conservative. The computed swirl vector indicating the magnitude and the direction of the velocity vector component on the yz-plane is shown in Figure 9.33. The area weighted swirl average is $10°$. The pressure distribution at the nozzle exit is shown in Figure 9.34 which should be compared with Figure 9.26. Since the swirl is strongest at the jet centre, the largest pressure reduction can be noticed in this region. Integrating the pressure distribution on the nozzle exit for the swirl free and swirling jet reveals that the swirl results in 19% smaller pressure force acting on the nozzle exit area. This number is not very different from the 23%

force reduction obtained from the theoretical formulas based on the solid body rotation assumption for the jet. The introduced tangential body force inside the impeller chamber increases the flow head comparing to the case which has just an axial body force component. Beside the pressure distribution on the nozzle exit this influences the flow rate through the nozzle. For the computed case the flow rate of the jet with swirl is 0.5% larger than that of the swirl free jet.

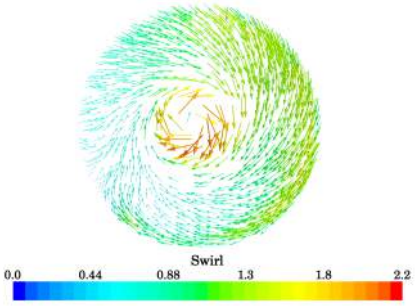

Figure 9.33 The swirl vector showing the magnitude of the radial and the circumferential velocity components at the nozzle exit.

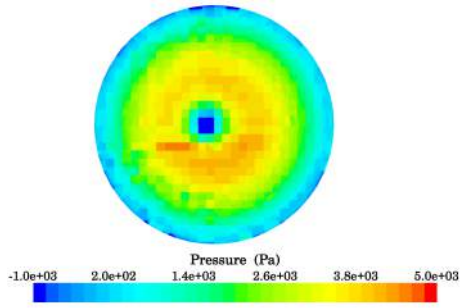

Figure 9.34 The total pressure distribution at the nozzle exit section for the jet with 10° of inclination with respect to the axial direction due to swirl.

Although the presented methods for the evaluation of the effect of swirl are approximate it is concluded that the change of the pressure force acting on the nozzle exit as well as the change of the jet flow rate can be neglected in this thesis. The changed exit pressure will reduce the exit drag by around 20%, but the conclusions about the relative importance of the intake/exit drags will still hold. Note that the 10° assumption for the area weighted swirl is likely to be an overestimation, even for pumps at off-design conditions. For pumps performing at, or close to, the design condition the jet swirl is mostly removed by the stators.

10 Conclusions and Future Work

10.1 Conclusions

As seen in Chapter 2, the motivation for this work has been twofold: to develop better understanding of the physics behind the waterjet/hull interaction, in particular the negative thrust deduction phenomenon, and to develop a fast and sufficiently accurate method for estimating the gross thrust of a waterjet driven hull. Two different methods are used for modelling the waterjet/hull interaction. The first one is a method which is developed and used in combination with the potential flow theory and a panel method code. The method is named the Pressure Jump Method in this thesis. The second technique for modelling the waterjet/hull interaction is based on RANS simulations. Employing this technique, the entire operating speed range of a waterjet driven hull is studied and the reasons for the different thrust deduction values at different speeds, including the intermediate range where the thrust deduction fraction is negative, are presented.

It is extremely difficult to find high quality measured data for validation. In the present work two main data sets are used for the validation of the computed results. The first one is from an experimental campaign within the 24th ITTC Specialist Committee on Waterjets carried out on the research vessel ATHENA. This data set is used for the validation of the results from the Pressure Jump Method. The second data set is from a recent measurement carried out at SSPA on a planing hull. The test results from SSPA are used for the validation of the RANS technique for modelling the waterjet/hull interaction. The measurement of the flow rate in both data sets has a large uncertainty. This makes the validation of the computed self-propulsion results difficult.

The important conclusions drawn at different stages of the current thesis are presented in the following. In order to make the conclusions distinct, they have been listed in separate items. First, the conclusions from the potential flow simulations are presented and then the conclusions from the bare hull and self-propulsion RANS simulations are given.

Potential Flow Method and Application

1. The Pressure Jump Method relates the hull resistance to the gross thrust and may be used in combination with both potential flow/boundary layer methods and more advanced viscous flow methods, for instance of the RANS type. In the present work the potential flow/boundary layer approach has been used for simulation of the waterjet/hull interaction. Computations are also carried out, simplifying the hull geometry to a flat plate. This is to obtain general relations for the sinkage and trim changes due to the waterjet-induced flow for different hull and intake geometries.

2. Due to the limitations of the potential flow assumption, there are some deviations between the computed and measured resistance, sinkage and trim. The former is however relatively accurately predicted using a correction technique, and in spite of the limitations the predictions of inlet velocity ratio, nozzle velocity ratio, gross thrust and thrust deduction are all within the experimental scatter. It should be noted that the predicted thrust deduction fraction is positive, as well as all the measured thrust deduction fractions at the model scale.

3. A mapping of the waterjet/hull interaction effects has been presented in the form of a flow chart. This chart includes all effects envisioned to relate bare hull resistance and gross thrust. Its main components are sinkage, trim, local effects, intake drag and exit drag. The sinkage, trim and local flow effects are subdivided into components, and based on an analysis of these components the following conclusions may be drawn:

    a. There is no sinkage or trim for a waterjet in free-stream conditions, i.e. for a waterjet fitted to an infinitely large flat plate and ejecting the flow horizontally. This is under the condition of infinitely deep water.

    b. The waterjet-induced pressure on a real hull increases the sinkage, which increases resistance.

    c. The influence of the waterjet-induced pressure on the trimming moment depends on the distance between the waterjet intake and the transom, and on the position of the centre of floatation. For most hulls a bow-down moment is generated, but if the intake is far aft, a moment in the other direction may be generated. Also, if the hull is very long, with a centre of floatation at a large distance from the intake, the moment may be bow-up.

    d. An inclination of the waterjet nozzle always induces a bow-down effect, as does the resistance/thrust couple.

    e. There is an optimum trim angle for the hull where the resistance is minimum. This is normally obtained where the transom has an optimum size. An increased trim may increase or decrease the resistance depending on the position on the resistance/trim curve relative to the optimum trim angle. The trim angle is one candidate for reducing the resistance, unless the hull has been optimized for self-propulsion.

    f. Wave resistance, above Froude number 0.6, normally increases due to deepening of wave trough at the stern caused by the intake suction.

g. The viscous resistance decreases due to the missing surface covering the intake opening, but it may increase somewhat due to the changes in the boundary layer around the intake.

Bare Hull RANS Method and Application

4. A prominent peak in the resistance coefficient curve of a semi-planing transom stern hull has been noticed both in measurements and CFD simulations at the critical Froude number, where the transom becomes dry. The peak occurred at a Froude number corresponding to the last hump in the resistance curve. In order to separate the two effects the transom submergence of the hull is changed by trimming the hull bow up and bow down in comparison to the initial even keel hull. The following conclusions are drawn from this study:

    h. The resistance coefficient curve from the bow up trimmed hull shows that the resistance hump and the resistance peak are clearly distinct from each other. The former is due to the interaction between the bow and stern waves and the latter is due to the clearance of the transom.

    i. The resistance curve for the bow-down trimmed hull is however smooth without abrupt changes at the critical Froude number. This is likely to be due to the extreme bow-down trim of the hull causing the transom to be very little submerged and the buttocks to have a rather large slope upwards, which makes this case very different from the even keel and bow-up cases.

    j. Both for the even keel and the bow-up cases there is a jump in the transom submergence just before clearance and the numerical simulations show that this is related to a minimum in pressure coefficient and a maximum in streamline curvature at the transom edge.

    k. The computed hydrodynamic and hydrostatic pressure resistance components of the transom yield a force that pushes the hull forwards, thereby reducing the total resistance below the critical Froude number. This pushing force diminishes abruptly as the transom becomes dry.

    l. The total pressure resistance of the rest of the hull increases rapidly just before the critical Froude number, mostly due to the increased hydrostatic pressure component. This increase is caused by the sudden local increase in transom submergence because of the sudden drop in the aft-part pressure of the hull.

    m. Thus, it is the rapid loss of the transom pushing force, together with the rapid increase in pressure resistance on the rest of the hull that create the peak in the total resistance coefficient.

Self-propulsion RANS Method and Application

5. A technique using a RANS method with a VOF free-surface representation combined with a body force representation of the pump has been developed. Validation showed good agreement for flow rate, but the gross thrust and thrust deduction are smaller than

those from the measurements at SSPA. A possible reason for the discrepancy is the novel experimental technique with a T-junction to measure the flow rate.

6. The thrust deduction has been investigated in detail over a large Froude number range. The main contribution to the thrust deduction fraction is the resistance increment fraction, whose variation can be explained as follows:

    n. In the low speed range large positive thrust deduction fraction values are computed. The significant increase of the resistance in the lower speed range is due to the increase in the hydrodynamic pressure resistance of the transom (larger suction) as well as the increase in the hydrostatic pressure resistance of the hull. The former is caused by the jet entrainment which reduces the hydrodynamic pressure at the transom and the latter is due to the increase transom submergence.

    o. The transoms of the bare hull and the self-propelled hull clear water near the hump speed. The latter clears at a lower Froude number mainly due to the jet entrainment. As mentioned above, there is a peak in the resistance coefficient curve at the critical Froude number. The resistance difference between the hulls is the largest at the peak when the waterjet-driven hull transom becomes dry. Then the difference diminishes rapidly with speed until the bare hull transom clears water. This causes the rapid drop of the thrust deduction fraction observed near the hump speed.

    p. In the intermediate speed range, the resistance increment fraction is almost constant and has values around zero. The hull has rather large trim angles in this speed range (~4° bow up), so the hydrostatic pressure force acting on the intake opening will have a horizontal component backwards. This surface is not present in self-propulsion and therefore the hydrostatic pressure resistance is reduced. There is however an increase in the hydrodynamic pressure resistance of the hull caused by the increased displacement (sinkage). The net result is a resistance increment close to zero.

        a. In the high speed range the resistance increment fraction gradually increases. Like in the intermediate speed range there is a decrease in the hydrostatic pressure resistance due to the missing intake-opening surface and an increase in the hydrodynamic resistance due to increased sinkage. However, the latter effect gradually becomes more important, which causes the increase in the total resistance.

7. The difference between gross and net thrust has been computed over the same Froude number range. For this purpose the geometry of the capture area and the streamtube were computed as well as the exit pressure and the vena-contracta. The following features were found:

    q. The capture area is quite different from the rectangular or semi-elliptical shape suggested by the ITTC Specialist Committee on Waterjets. Despite this, the average velocity of the rectangular capture area obtained from the boundary layer profile on a flat plate is very close to the computed average velocity on the actual capture area. The area and the width of the capture area vary with the speed. The

area is largest at the critical Froude number where also the resistance coefficient has a maximum.

r. The diameter of the vena-contracta is 3% smaller than the nozzle exit diameter and it is located less than one nozzle exit diameter after the exit section. The diameter and the location of the vena-contracta are dependent on the nozzle geometry.

s. According to the computed momentum flux correction coefficients, the assumption of a uniform velocity distribution will have the largest influence on the momentum flux at the capture area. This assumption will results in $1 - 2.5\%$ under-prediction of the ingested momentum flux. The momentum flux at the nozzle exit will be 0.5% under-predicted.

t. The largest contribution to the difference between the gross thrust and the net thrust comes from the exit drag due to the non-atmospheric pressure at the nozzle exit, which depends on the nozzle shape as well as the nozzle exit being ventilated or submerged in the transom wave. The resistance of the self-propelled hull is very close to that of the bare hull in the speed range where the negative thrust deduction values are found. For the SSPA hull, it is shown that the non-atmospheric pressure at the nozzle exit is the major reason for the negative thrust deduction fraction values.

10.2 Future Work

The main focus of this thesis work was to understand the physics behind the waterjet/hull interaction at different speed ranges. The investigations of the interaction effects have been carried out using a series of numerical simulations and experimental measurements at model scale and the scaling of the data has not been investigated. The ITTC Specialist Committee on Waterjets (ITTC 2005d) has employed the Froude scaling method and has assumed that the waterjet flow rate scales proportional to the length scale cubed. The Committee highlights the large uncertainty of this scaling method. The difference between the boundary layer at the capture area in model scale and full scale can influence the ingested momentum flux and the gross thrust. In the measurement carried out by CCDoTT (The Commercial Deployment of Transportation Technologies) (Cusanelli et al. 2007) the difference of the boundary layer thickness due to scale change was taken into account in the data scaling procedure. Consequently, although the thrust deduction fraction was positive in the model scale, taking this correction into account resulted in a negative thrust deduction fraction. This conclusion raises the question whether or not the thrust deduction is dependent on scaling. So far there is no universal scaling method and further investigations on this topic are required.

The assessment of the waterjet self-propulsion measurements carried out at SSPA (Brown 2013) indicates the large influence of the flow rate measurement accuracy on the thrust deduction fraction. The importance of the flow rate measurement accuracy has also been highlighted by the ITTC Specialist Committee on Waterjets (ITTC 2005d). It would be worthwhile to evaluate the accuracy of the experimental techniques using CFD.

It would be of interest to study the waterjet/hull interaction in shallow water. Operating in this condition can influence the ingested momentum flux of the waterjet and add some more factors to those which are playing a role in the interaction.

In real operating conditions the effect of waves on the hull resistance and the waterjet system performance might be important. The transient flow around the hull can change the hull attitude and resistance. Moreover, the risk of air ingestion in the waterjet unit, which affects the performance of the pump, may become larger for the hull operating in waves. The possibility of the nozzle exit suddenly penetrating the transom wave can also change the thrust of the waterjet unit. Therefore, it would be worth investigating the waterjet/hull interaction effects in a seaway.

In this thesis work, it was shown that the exit drag plays an important role in the magnitude of the thrust deduction fraction. The reason is the non-atmospheric pressure distribution on the nozzle exit. It would be of interest to study the exit drag for different nozzle geometries.

In the simulations and measurements presented in this thesis, the possible influence of the steering unit on the hull resistance as well as on the transom clearance are neglected. Investigation of these effects at lower speed ranges where the reversing bucket unit is penetrating the transom wave would be of interest.

In order to model the pump geometry an axial body force model is used in the self-propulsion RANS simulations carried out in this thesis. This means that the flow at the nozzle exit is swirl free, which cannot be exactly true in off design operating conditions. In order to take the effect of the jet swirl into account, it would be worthwhile to introduce a body force model which, beside the axial component, has a tangential component that corresponds to the possible jet swirl. Moreover, the body force model can be evaluated by comparing the pump flow obtained from this model with the flow computed using the actual pump geometry.

Appendices

Appendix A. Marine Waterjet Development History

Date	Name	Remarks
287-212 BC	Archimedes	Axial Water Pump
1452-1519	Leonardo Da Vinci	Axial Water Pump, Screw Propulsion
1631	David Ramsey	Patented Steam Waterjet Ship Propulsion
1642-1727 (1687)	Isaac Newton	Isaac Newton in his *Philosophiae naturalis principia mathematica* formulated the laws of science that are applicable to Ramsey's idea
1661	Toogood and Hayes	Patent for Archimedean Screw WJ
1680	Robert Hooke	Archimedean Screw Propeller
1775	Benjamin Franklin	Proposal for Waterjet Propelled Boat
1736-1819	James Watt	Reciprocating and Rotary Steam Engins
1782	James Rumsey	Waterjet Propelled 80 ft Ferry Boat (Potomac)
1787	Kempelen	Steam Turbines
1791	Barber	Patented Gas Turbine
1802	William Symington	Charlotte Dundas Steam Tug (Clyde)
1807	Robert Fulton	Clemont Steamship (Hudson)
1812	Henry Bell	Steamship Comet (Clyde)
1836-1845	Francis Pettit Smith	Screw Propellers, England
1840's	John Ericsson	Marine Propellers (Including Contra-Rotating), Sweden/USA
1853	John Ruthven	Waterjet Ship Enterprise (Not Successful)
1853	Seydell	Waterjet Ship Albert (Successful) (Oder)
1863	British Admiralty	Waterjet Ship Nautilus, 10 kt (Thames)
1863	British Admiralty	Waterjet Ship Waterwitch Versus Viper
1870	C.M. Ramus	Planning Boat Rocket Propulsion
1878	Swedish Government	Comparative Trials Waterjet and Propeller
1880	Thorneycroft J1	Pump-Jet Propulsion (Exterior)
1894	Royal National Lifeboat Institution	Waterjet Lifboat
1932	First Riva Calzoni Waterjet	
1959-1967	Donald Cambell	Bluebird, Gas Turbine Jet Propulsion
1952	Etablissements Billiez	Waterjet Ferry (France)
1954	First Hamilton Waterjet	New Zealand's Rivers
1968	First KaMeWa Waterjet	Mixed Flow Pump Waterjet
1968-1972	Tucumcari (PGH-2)	Boeing/Cenrifugal Pump
1971-1980	SES 100A	74 kt (1978) Inducer Pump Waterjet
1971-1983	SES 100B	92 kt (1977) Surface Piercing Propellers
1973-1978	2K/3KSES	Most Powerful Waterjet Development
1974-present	PHM	Boing/ALRC Inducer/Mixed Flow, 2 Speed Coaxial Shaft Pumps
1974-present	Jetfoil	Boeing/Kawasaki Inducer/ Axial Pumps
1989	Riva Calzoni	Atlantic Challenger Waterjet
1990	SES 200	Waterjet Conversion
1991	KaMeWa 180 SL1	Largest Current Waterjet Built
1992	SEC SES	Largest Waterjet Ship
1992	Yamato	First MHD Waterjet Ship
1992	Destriero	Atlantic Speed Record with KaMeWa Waterjets
2003	Techno SuperLiner (TSL)	The world´s largest and most powerful waterjets installed on Japanese Techno SuperLiner passenger/cargo ship. Two waterjets, 2.35m in diameter, powered by 27 MW each.
2004	Littoral Combat Ship (LCS)	First deliveries to the largest navy contract with waterjets, the Littoral Combat Ship (LCS) for US Navy Freedom- and Independence-class
2005	AWJ-21™	Submerged waterjet developed by Rolls-Royce for US Navy

The events until 1993 are adopted from (Allison 1993).

Appendix B. Waterjet Control Volume

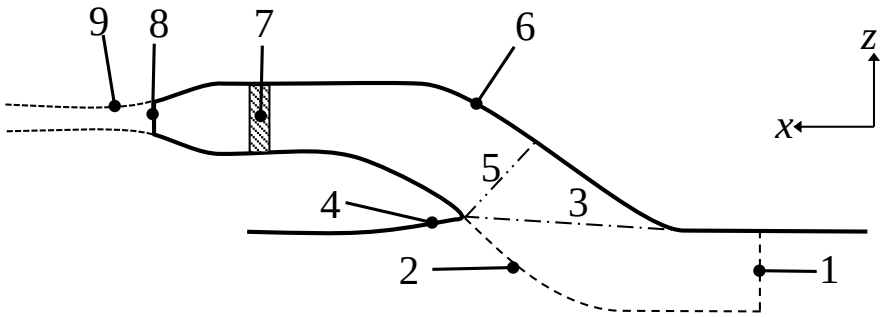

Surface 1	capture area
Surface 2	dividing streamtube
Surface 3	surface covering the intake-opening
Surface 4	part of the waterjet unit which lies outside the streamtube
Surface 5	intake throat where the sectional area of the channel is the minimum
Surface 6	waterjet system internal material boundaries
Surface 7	boundary area of the pump control volume
Surface 8	nozzle discharge area
Surface 9	vena-contracta

Appendix C. Wave Making Resistance Correction

Table b. AMECRC systematic series

Model	L/B	B/T	C_b	WSA[m^2]	Δ [kg]	$L/\nabla^{1/3}$
1	8.00	4.0	0.396	0.3149	6.321	8.649
2	6.51	3.5	0.395	0.3850	11.455	7.100
3	8.00	2.5	0.447	0.3794	11.454	7.074
4	8.00	4.0	0.447	0.3056	7.158	8.274
5	4.00	4.0	0.395	0.6297	25.344	5.444
6	8.00	2.5	0.395	0.3554	10.123	7.393
7	4.00	2.5	0.396	0.7111	40.523	4.649
8	4.00	2.5	0.500	0.7463	51.197	4.300
9	8.00	2.5	0.500	0.3732	12.804	6.817
10	8.00	4.0	0.500	0.3136	8.003	7.990
11	4.00	4.0	0.500	0.6272	32.006	5.031
12	8.00	3.3	0.497	0.3354	9.846	7.442
13	8.00	3.3	0.450			6.362
14	6.00	4.0	0.500	0.4180	14.204	6.593

* All models are 1.6 m in length

Table a. Constants to be used for obtaining resistance correction factor

a_1	-14.741
a_2	8.353
a_3	6.569
a_4	-7.103
a_5	-41.182
a_6	70.842
a_7	-44.422
a_8	-34.315
a_9	38.226
a_{10}	226.876
a_{11}	-106.445
a_{12}	87.905
a_{13}	67.534
a_{14}	-78.547
a_{15}	-473.974
a_{16}	52.252
a_{17}	-76.289
a_{18}	-58.507
a_{19}	71.958
a_{20}	441.525
a_{21}	-1.258
a_{22}	24.716
a_{23}	18.962
a_{24}	-24.703
a_{25}	-156.221

Appendix D. HAMILTON Jet Test Boat

The main particulars of the full-scale test boat at the parent condition Δ_0, LCG_0 are presented in the following (van Terwisga 1996).

Description	Symbol	Magnitude	Unit
Length between perpendiculars (Fr. 1-8)	L_{PP}	7.27	m
Length on waterline	L_{WL}	6.27	m
Hull beam at draught moulded at mid-ship	B	2.226	m
Draught moulded on FP	T_F	0.386	m
Draught moulded on AP	T_A	0.424	m
Displacement volume moulded	∇	2.798	m^3
Displacement mass in sea water	Δ	2.868	t
Wetted surface area bare hull at rest	S	13.264	m^2
LCB position aft of frame 8	LCB	4.58	m
Slenderness ratio	$L_{PP}/\nabla^{1/3}$	5.16	-
Length to beam ratio	L_{PP}/B	3.27	-
Beam to draught ratio	B/T_M	5.50	-

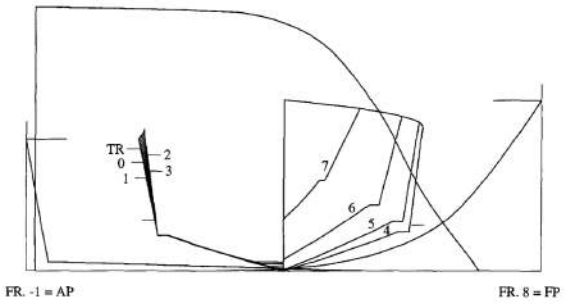

Figure A1 Body plan, stem and stern profiles and sectional area curve of model

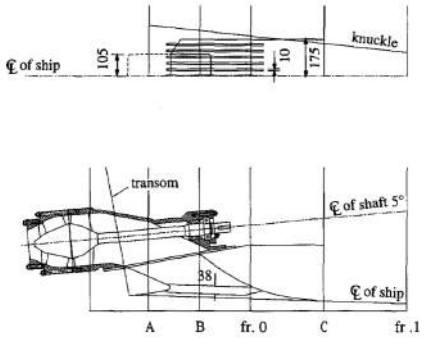

Figure A2 Waterjet intake opening and ducting geometry
(Dimensions are given in millimetres)

Appendix E. Pressure Resistance Components of the SSPA Hull

The computed components of the pressure resistance for the SSPA bare hull and the waterjet-propelled hull for the entire operating speed range are plotted in Figure A3 and A4.

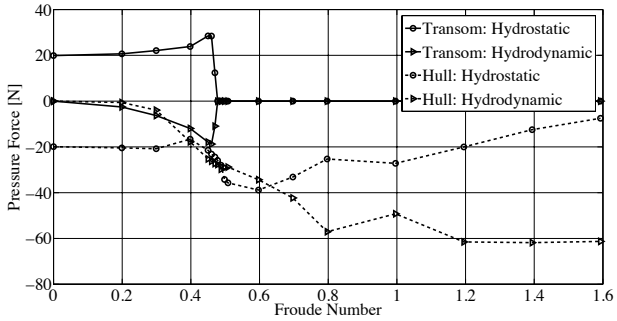

Figure A3 Bare hull pressure resistance components

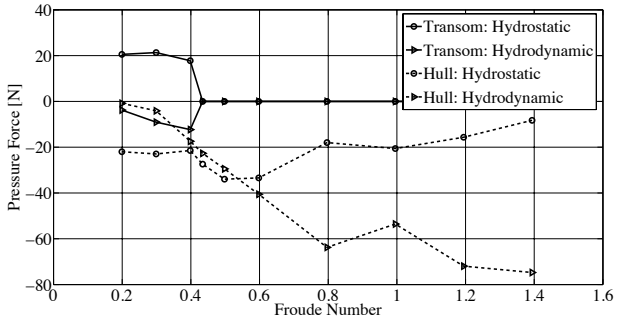

Figure A4 Self-propelled hull pressure resistance components

Nomenclatures

A	control surface
A_H	water plane area
A_I	intake opening area
$A_{impeller}$	impeller area
A_m	hull maximum sectional area
A_{nozzle}	nozzle discharge area
A_T	transom wetted area
A_{tr}	hull transom area
B	hull beam
BH	bare hull
BH_{SP}	bare hull with the same sinkage and trim as self-propelled hull
C_b	block coefficient
C_F	total friction coefficient
C_L	lift coefficient
c_m	momentum flux correction coefficient
CoF	centre of floatation
cp	local pressure coefficient
Cp	pressure coefficient
C_T	resistance coefficient
CV	control volume
C_W	wave-making resistance coefficient obtained from pressure integration
C_{WTWC}	wave-making resistance obtained from the transverse wave cut method
C_σ	non-dimensional sinkage
D_e	exit drag
D_i	intake drag
$D_{impeller}$	impeller diameter
D_{nozzle}	nozzle diameter
F	force vector
F_D	ducting channel lift force
F_H	lift force on the flat plate hull in free-stream condition
F_I	lift force on the imaginary intake covering the hull opening
Fn	Froude number
Fn^*	critical (transom clearance) Froude number
Fo	lift force on the outer domain in free-stream condition
Fs	lift force on the entire flat surface in free-stream condition
Fp	pump force vector
g	gravitational acceleration
GM_L	hull metacentric height
H	flow head
h	height of the capture area
i, j, k	tensor indices denoting the ordinates
IVR	intake velocity ratio at the capture area
IVR_i	intake velocity ratio at the rectangular intake area on hull
JVR	jet velocity ratio
K_{CW}	correction factor of the wave making resistance obtained from pressure integration
LCG	longitudinal centre of gravity
LOW	waterline length
Lpp	length between perpendiculars
m	hull mass displacement
M	momentum flux vector

M_y	moment about the *y*-axis
NVR	nozzle velocity ratio
n_λ	number of panels per characteristic wavelength
p	time averaged pressure
P_{after}	pressure after the impeller disk
p_{atm}	atmospheric pressure
P_{front}	pressure before the impeller disk
Q	volume flow rate
R	jet diameter
r	resistance increment
R	resistance vector
R_A	rope force
R_{bh}	bare hull resistance
R_D	ducting channel resistance
R_H	hull resistance
R_N	nozzle resistance
Rn	Reynolds number
R_{sp}	self-propelled hull resistance
R_{TWOP}	total resistance of the waterjet/hull system without pressure jump
S	control surface
SP	self-propelled hull
S_{ref}	reference surface
T	hull draught
t	total thrust deduction fraction
T_g	gross thrust vector component in *x*-directon
t_j	jet thrust deduction fraction
T_{net}	net thrust vector component in *x*-directon
t_r	hull thrust deduction fraction
u	velocity vector
u_∞	undisturbed velocity
u_ϕ	tangential component of velocity vector
V	control volume
w	width of ducting channel intake
w_{capt}	width of the capture area
x, y, z	Cartesian earth fixed coordinates
β	momentum flux correction factor
∇	displacement volume
Δ	displacement mass
δ_{ij}	Kronecker delta
Δp	pressure jump through impeller
ΔR	resistance increment
θ	shaft line angle with horizon ($\theta = \theta_n + \tau$)
θ_n	nozzle inclination angle with horizon
ρ	density of fluid
σ	sinkage
τ	hull sinkage
τ_{ij}	shear stress tensor
ϕ	momentum flux vector
$\vec{T}_g$	gross thrust vector in ship-fixed coordinates
$\vec{T}_{net}$	net thrust vector in ship-fixed coordinates

Subscripts

a	aft
bh	bare hull
est	estimated
EW	entrained water
f	fore
M	model scale
n	nozzle
RT	resistance/thrust
S	ship
sp	self-propulsion
0	free-stream condition
∞	undisturbed

References

Alexander, K., Coop, H. & van Terwisga, T., 1994. Waterjet-Hull Interaction Recent Experimental Results. In *SNAME Transaction*. Society of Naval Architects and Marine Engineers, pp. 87–105.

Allison, J., 1993. Marine waterjet propulsion. In *Transactions - Society of Naval Architects and Marine Engineers*. pp. 275–335.

Allison, J.L. et al., 2001. Research in Waterjet Inlet, Hull and Jet Interactions. In *Waterjet Propulsion III*. Gothenburg: The Royal Institute of Naval Architects.

Bennet, W., 1858. *Patents for inventions. Abridgments of the specifications; Marine Propulsion(excluding sails)*, Printed by George E. Eyre and William Spottiswoode, Printers to the Queen's most Excellent Majesty.

Brown, M., 2013. Model tests of a complete waterjet-hull system. In SSPA report RE40084817-16-00-B.

Bulten, N., 2008. A Breakthrough in Waterjet Propulsion Systems. In *Doha International Maritime Defence Exhibition and Conference DIMDEX*. Qatar, pp. 2–7.

Bulten, N. & van Esch, B., 2005. Review of Thrust Prediction Method Based on Momentum Balance for Ducted Propellers and Waterjets. *ASME Conference Proceedings*, pp.1621–1629.

Bulten, N.W.H., 2006. *Numerical Analysis of a Waterjet Propulsion System*. PhD Thesis, Eindhoven University of Technology.

Carlton, J., 2007. *Marine Propellers and Propulsion* Second Edi., Elsevier Ltd.

Coop, H.G., 1995. *Investigation of Hull-Waterjet Interaction Effects*. PhD Thesis, Department of Mechanical Engineering, University of Canterbury.

Cusanelli, D.S., Carpenter, S.A. & Powers, A.M., 2007. *Axial Waterjet (AxWJ) Model 5662 and Mixed-Flow Waterjet (MMMWJ) Model 5662-1: Comparisons of Resistance and Model- Scale Powering with Propulsion Nozzle Designs*,

Delaney, K. et al., 2009. Use of RANS for Waterjet Analysis of a High-Speed Sealift Concept Vessel. In *First International Symposium on Marine Propulsors SMP'09*. Trondheim, Norway.

Demirdžić, I., Muzaferija, S., 1995. Numerical method for coupled fluid flow, heat transfer and stress analysis using unstructured moving meshes with cells of arbitrary topology. *Computer Methods in Applied Mechanics and Engineering*, 125, pp.235–255.

Ding, J. & Wang, Y., 2010. Research on flow loss of inlet duct of marine waterjets. *Journal of Shanghai Jiaotong University (Science)*, 15(2), pp.158–162.

Ding J.-M., W.Y.-S., 2010. Research on flow loss of inlet duct of marine waterjets. *Journal of Shanghai Jiaotong University (Science)*, 15(2), pp.158–162.

Doctors, L.J., 2006. Infuence of the Transom-Hollow Length on Wave Resistance. In *International Workshop on Water Waves and Floating Bodies (IWWWFB)*. Loughborough, UK.

Doctors, L.J., Macfarlane, G.J. & Young, R., 2007. A study of transom-stern ventilation. *International Shipbuilding Progress*, 54, pp.145–163.

Dyne, G. & Lindell, P., 1994. Waterjet Testing in the SSPA towing Tank. In *International Symposium if Waterjet Propulsion, RINA*. London: The Royal Institute of Naval Architects.

Eça L. & Hoekstra, M., 2014. A procedure for the estimation of the numerical uncertainty of CFD calculations based on grid refinement studies. *Journal of Computational Physics*, 262, pp.104–130.

Eslamdoost, A., Larsson, L. & Bensow, R., 2013. A Pressure Jump Method for Modeling Waterjet/Hull Interaction. *Ocean Engineering*.

Eslamdoost, A., Larsson, L. & Bensow, R., 2014a. On Transom Clearance. *Submitted to Ocean Engineering*.

Eslamdoost, A., Larsson, L. & Bensow, R., 2014b. Waterjet Propulsion and Thrust Deduction. *Journal of Ship Research*, 58(4), pp.1–15.

Etter, R.J., Krishnamoorthy, V. & Scherer J. O., 1981. Model Testing of Waterjet Propelled Craft. In *Proceedings of the 9th General Meeting of the American Towing Tank Conference*. Ann Arbor, Michigan: Ann Arbor Science Publishers, Inc.

Ferziger, J.H. & Perić, M., 2003. *Computational Methods for Fluid Dynamics* 3rd ed. Springer, ed., Berlin, Heidelberg: Springer.

Flexner, J.T., 1944. *Steamboats come true : American inventors in action*, New York: Viking Press.

Hadler, J.B., 1966. The Prediction of Power Performance on Planing Craft. In *Transactions of the Society of Naval Architects and Marine Engineers*. New York, pp. 563–610.

Harries, S. & Schulze, D., 1997. Numerical investigation of a systematic model series for the design of fast monohulls. In *International Conference on Fast Sea Transportation, FAST '97*. Sidney, Australia.

Hino, T. & Ohashi, K., 2009. Numerical Simulation of Flow around a Waterjet Propelled Ship. In *First International Symposium on Marine Propulsors smp'09*. Trondheim.

Höglund, V., 2004. *Validation and Correction of SHIPFLOW for Fast Hulls*. MSc Thesis, Chalmers University of Technology.

Hu, P. & Zangeneh, M., 2001. CFD Calculation of the Flow Through a Water-Jet Pump. In *Waterjet Propulsion III*. Gothenburg: The Royal Institute of Naval Architects.

Hyo, K.J. et al., 2006. Investigation of turbulent flows in a waterjet intake duct using stereoscopic PIV measurements. *Journal of Marin Science and Technology*, 11(4), pp.270–278.

ITTC, 2005a. Recommended Procedures and Guidelines ITTC – Recommended Procedures and Guidelines Waterjet Propulsive Performance Prediction – Propulsion Test and Extrapolation.

ITTC, 2005b. *Recommended Procedures and Guidelines ITTC – Recommended Procedures and Guidelines Waterjet Propulsive Performance Prediction Waterjet Inlet Duct , Pump Loop and Waterjet System Tests and Extrapolation*,

ITTC, 2004a. Recommended Procedures and Guidelines; Waterjet Propulsive Performance Prediction. In *International Towing Tank Conference*.

ITTC, 1996a. *Report of the Specialist Committee on Waterjets, 21st International Towing Tank Conference*,

ITTC, 2005c. *The presentation for the report of the 24th ITTC Specialist Committee on; Validation of Waterjet Test Procedures*, Edinburgh.

ITTC, 2004b. The Specialist Committee on Validation of Waterjet Test Procedures Final Report and Recommendations to the 24th ITTC. , II, pp.471–508.

ITTC, 2005d. *The Specialist Committee on Validation of Waterjet Test Procedures, Final Report and Recommendations to the 24th ITTC*,

ITTC, 2002. *The Specialist Committee on Validation of Waterjet Test Procedures: Final Report and Recommendations to the 23rd ITTC*,

ITTC, 1996b. *The Specialist Committee on Waterjets: Final Report and Recommendations to the 21st ITTC*,

ITTC, 2008. The Specialist Committee on Waterjets: Final Report and Recommendations to the 25th ITTC. In *Proceedings of 25th ITTC*. Fokuoka, Japan.

Janson, C.-E., 1997. *Potential Flow Panel Methods for the Calculation of Free-surface Flows with Lift*. PhD Thesis, Chalmers University of Technology.

Jessup, S.D. et al., 2008. Performance Analysis of a Four Waterjet Propulsion System for a Large Sealift Ship. In *Proceedings of the 27th Symposium on Naval Hydrodynamics*.

Johansson, A., 1995. *Trim Effect on High-Speed Craft due to Waterjet-Hull Interaction*. MSc Thesis, KTH Royal Institute of Technology.

Jones, Jr. , Paul, Harman, H.L., 1935. Toy Boat (Patenent).

Jonsson, C., 1996. *On Waterjet Performance Prediction Methods*. MSc Thesis, Chalmers University of Technology.

Kandasamy, M. et al., 2010. Integral Force/Moment Waterjet Model for CFD Simulations. *Journal of Fluids Engineering*, 132(10).

Kandasamy, M. et al., 2011. Numerical and Experimental Evaluation of Waterjet Propelled Delft Catamarans. In *11th International Conference on Fast Sea Transportation (FAST 2011)*. Honolulu, Hawaii, USA.

Kruppa, C., Brandt, H., Östergaard, C., 1968. Wasserstrahlantriebe für Hochgeschwindigkeitsfahrzeuge. In *Jahrbuch der STG 62*. pp. 228–258.

Larsson, L. & Eliasson, R.E., 2007. *Principles of Yacht Design* 3rd ed., Camden, Me : International Marine ; McGraw-Hill.

Larsson, L. & Raven, H.C., 2010. *Ship resistance and flow* J. R. Paulling, ed., The Society of Naval Architects and Marine Engineers.

Maki, K.J., 2006. *Transom Stern Hydrodynamics*. PhD Thesis, Naval Architecture and Marine Engineering, The University of Michigan.

Maki, K.J. et al., 2006. Transom-stern flow for high-speed craft. *Austrailian Journal of Mechanical Engineering*, 3(2), pp.191–199.

Mercia, J.A. & Savitsky, D., 1973. *Resistance of Transom Stern Craft in the Pre-Planing Regime*,

Muzaferija, S. & Perić, M., 1999. Computation of free surface flows using interface-tracking and interface- capturing methods. In *Nonlinear Water Wave Interaction*. Southampton: WIT Press, pp. 59–100.

Oving, A.J., 1985. *Resistance Prediction Method for Semi-Planing Catamarans with Symmetrical Demihulls*, Wageningen.

Peri, D. et al., 2012. Simulation Based Design with Variable Physics Modeling and Experimental Verification of a waterjet propelled Catamaran. , (August), pp.26–31.

Van der Ploeg, A. & Starke, B., 2013. Prediction Of The Transom Flow Regime With Viscous Free Surface Computations. *MARINE 2011, IV International Conference on Computational Methods in Marine Engineering*, 29, pp.261–272.

Purnell, J.G., 1976. *The Performance Gains of Using Wide Flush Boundary Layer Inlets on Water-Jet Propelled Craft*, Annapolis.

Raithby, J., 1829. *The statutes relating to the admiralty, Navy, shipping, and navigation of the United Kingdom, from 9 Hen. III to 3 Geo. IV inclusive*, Printed by George E. Eyre and Andrew Strahan, Printers to the King's most Excellent Majesty.

Rhee, B. & Coleman, R., 2009. Computation of Viscous Flow for the Joint High Speed Sealift Ship with Axial-Flow Waterjets. In *First International Symposium on Marine Propulsors SMP'09*. Trondheim, Norway.

Rispin, P., 2005. *Model Test and Evaluation of an Advanced Axial Flow Waterjet Pump Designed for the Coastal Commercial Ship Sealift Application*,

Roberts, J.L., 1998. *The Influence of Hull Boundary Layers on Waterjet Intake Performance*. PhD Thesis, Department of Civil and Mechanical Engineering, University of Tasmania.

Roberts, J.L. & Walker, G.J., 1995. Performance of waterjet propulsion system with boundary layer ingestion. In *Twelfth Australian Fluid Mechanics Conference*. Sidney: The University of Sidney, pp. 271–274.

Roy, S.M., 1994. The Evolution of the Modern Waterjet Marine Propulsion Unit. In *International Symposium if Waterjet Propulsion, RINA*. London: The Royal Institute of Naval Architects.

Saunders, H.E., 1957. Hydrodynamics in Ship Design. In New York: Society of Naval Architects and Marine Engineers(SNAME), pp. 648–649.

Schult, J., 1974. *Curious Boating Inventions*, London: Elek.

Sherer, J.O. & Mutnick, I., 2001. Procedure for conducting a towing tank test of a waterjet propelled craft using Laser Doppler velocimetry to determine the momentum and energy flux. In *Proceedings of 26th ATTC*. Glen Cove NY: Webb Institute.

Starke, B., Raven, H. & van der Ploeg, A., 2007. Computation of transom-stern flows using a steady free-surface fitting RANS method. In *9th International Conference on Numerical Ship Hydrodynamics*. Ann Arbor, Michigan, US.

Takai, T., 2010. *Simulation based design for high-speed sea lift with waterjets by high fidelity URANS approach*. MSc Thesis, IIHR-Hydroscience & Engineering, The University of Iowa.

Takai, T., Kandasamy, M. & Stern, F., 2011. Verification and validation study of URANS simulations for an axial waterjet propelled large high-speed ship. *Journal of Marine Science and Technology*, 16(4), pp.434–447.

Van Terwisga, T., 1996. *Waterjet-Hull Interaction*. PhD Thesis, Delft Technical University.

Van Terwisga, T. & Alexander, K. V., 1995. Controversial issues in waterjet-hull interaction. In *International Conference on Fast Sea Transportation, FAST '95*. Lubeck-Travemunde, Germany, pp. 1235–1253.

Weiss, J., Maruszewski, J.P., Smith, W.A., 1999. Implicit solution of preconditioned Navier-Stokes equations using algebraic multigrid. *AIAA*, 37, pp.29–36.

White, F.M., 2008. *Fluid Mechanics* Sixth., McGraw-Hill.

Wilson, M.B. et al., 2004. Analysis of hull boundary layer velocity distributions with and without active waterjet inlets. In *Waterjet Propulsion 4*. London, pp. 29–37.

Wilson, M.B. et al., 2005. Waterjet-Hull Interaction for Sealift Ships. In *International Conference on Marine Research and Transportation (ICMRT'05)*. Gulf of Naples.

Wolfstein, M., 1969. The velocity and temperature distribution in one-dimensional flow with turbulence augmentation and pressure gradient. *Int. J. Heat Mass Transfer*, 12, pp.301–318.